MAGNETISM AND TOPOLOGICAL FEATURES IN THE NOVEL 2D SYSTEMS OF OSMIUM-BASED HALIDES OsX_3(X:Cl,Br,I)

ANDRÉS FELIPE GÓMEZ BASTIDAS

UNIVERSIDAD INDUSTRIAL DE SANTANDER

FACULTAD DE CIENCIAS

ESCUELA DE FÍSICA

BUCARAMANGA

2023

MAGNETISM AND TOPOLOGICAL FEATURES IN THE NOVEL 2D SYSTEMS OF OSMIUM-BASED HALIDES OsX_3(X:Cl,Br,I)

ANDRÉS FELIPE GÓMEZ BASTIDAS

Undergraduate thesis

Supervisor
Prof. ANDRÉS CAMILO GARCIA CASTRO, Ph.D.
Escuela de Física, Universidad Industrial de Santander

Co-supervisor
Prof. OLEG RUBEL, Ph.D.
Department of Materials Science and Engineering, McMaster University

UNIVERSIDAD INDUSTRIAL DE SANTANDER
FACULTAD DE CIENCIAS
ESCUELA DE FÍSICA
BUCARAMANGA
2023

DEDICATION

To my parents and grandparents
for their love and support.

"Throughout my life, the moments, and people who have defined me. . . they have all been illuminated by sparks."

-Kentaro Miura

AGRADECIMIENTOS

Inicialmente agradezco a mis padres, Hernando Gómez y Claudia Bastidas por su amor incondicional, su apoyo y sus invaluables lecciones. La vida no pudo darme mejor regalo que ser su hijo.

Agradezco a los amigos que me acompañaron cursando la carrera: Camilo Murillo, Juan Gómez, Juan Díaz, German Prada, Katherin Gómez y Dana Lopez. Porque sin su amistad y apoyo, el camino hubiese sido muy dificil.

Así mismo, me encuentro muy agradecido con el profesor Andrés, ya que le dió dirección a mi vida académica y me permitió ser parte de su grupo de investigación. Agradezco su enseñanza de la investigación científica, siendo cada reunión un estimulante intelectual y anímico para seguir adelante. Tambien como su apertura como persona, brindandome una amistad y preocupandose por formar profesionales integros.

De igual forma, agradezco al profesor Oleg la oportunidad de trabajar en su grupo de investigación y conocer los bellos paisajes Canadienses.

Quiero agradecer al grupo de investigación FICOMACO, al centro de computación GUANE (UIS), al laboratorio nacional de supercomputo (LNS, Benemérita Universidad Autónoma de Puebla - México) y la infrastructura de Compute Canada por prestar sus instalaciones para llevar a cabo las simulaciones necesarias para mi trabajo de grado.

Finalmente, expreso mi gratitud a todos los profesores de la Universidad Industrial de Santander que contribuyeron en mi formación profesional.

ACKNOWLEDGEMENTS

Initially, I thank my parents, Hernando Gómez and Claudia Bastidas for their unconditional love, support and invaluable lessons. Life could not have given me a better gift than to be their son.

I thank my friends who accompanied me during my studies: Camilo Murillo, Juan Gómez, Juan Díaz, German Prada, Katherin Gómez and Dana Lopez. Without their friendship and support, the road would have been incredibly difficult.

Likewise, I am very grateful to Professor Andrés, since he gave direction to my academic life and allowed me to be part of his research group. I am thankful for his teaching of scientific research, and each meeting as an intellectual and encouraging stimulant to move forward. I am also grateful for his openness as a person, offering me friendship and caring about forming integral professionals.

Likewise, I thank Professor Oleg for the opportunity to work in his research group and to get to know the beautiful Canadian landscapes.

I would like to thank the FICOMACO research group, the GUANE computing center (UIS), the national supercomputing laboratory (LNS, Benemérita Universidad Autónoma de Puebla - Mexico) and the Compute Canada infrastructure for lending their facilities to carry out the simulations necessary for my degree work.

Finally, I would like to express my gratitude to all the professors of the Universidad Industrial de Santander who contributed to my professional training.

Contents

pág.

List of Figures

pág.

[1] Khomskii 2014.

List of Tables

pág.

Section 1.0

ABSTRACT

TITLE: MAGNETISM AND TOPOLOGICAL FEATURES IN THE NOVEL 2D SYSTEMS OF OSMIUM-BASED HALIDES OsX_3(X:Cl,Br,I) *

AUTHOR: ANDRÉS FELIPE GÓMEZ BASTIDAS **

KEYWORDS: electronic structure, 2D magnetism, topological materials

DESCRIPTION: The recently discovered 2D magnetic van der Waals crystals, possess novel physical characteristics and the potential of being topological materials. Advances in experimental techniques for synthesizing and characterization of monolayer materials have demonstrated the theoretically predicted magnetic properties, disproving the applicability of the Mermin-Wagner theorem. Also, allows the design of innovative devices. There is a great interest in the theoretical prediction of topological materials such as the Chern insulator due to the promising applications of these systems in areas such as spintronics and quantum computing. Theoretical studies of transition metal tri-halide compounds have shown the presence of both properties, inherent magnetic ordering and non-trivial topology. Therefore we focused our efforts on the theoretical exploration of the electronic, magnetic and topological features of the compound family OsX_3 with (X: Cl, Br, I) from the density functional theory (DFT) framework. The selection was taken based on the characteristics of this new condensed matter system: a break of time reversal symmetry due to intrinsic

---

* Bachelor Thesis

** Faculty of Sciences. School of Physics. Supervisor: Andres Camilo Garcia Castro, Ph.D. Co-supervisor: Oleg Rubel, Ph.D.

magnetism, hexagonal symmetry and high spin-orbit coupling. With these conditions the emergence of non-trivial topological properties are expected, such as protected metallic edge states and the quantum anomalous Hall effect. We demonstrate the importance of the electronic structure description for an accurate study of these properties and the high sensitivity of the theoretical prediction of these characteristics to the treatment of electronic correlation. Moreover, the development of a topological characterization tool CHERN from DFT calculations is presented.

Section 2.0

INTRODUCTION

The study of two-dimensional materials has generated great interest in the condensed matter field due to the emergence of unusual phenomena compared to the presented in the three-dimensional case[1]. A fundamental advance in this area was the successful exfoliation of graphene in 2004, an event which allowed the transition from a purely theoretical study to the experimental realm[2]. Consequently, the search for other monolayer exfoliable materials started, with the expectation to encounter novel properties as in the graphene case. For example, the exfoliation of monolayers has been successful in mono-elemental materials such as silicine[3] and germanene[4] and bi-metallic compounds of h-BN type[5]. 2D materials properties comprehend a broad spectrum of functionalities, such as insulators, semiconductors, metals, superconductors and topological phases[6]. Nevertheless, a fundamental material property was absent in this systems: intrinsic magnetism. This was not surprising since the Mermin-Wagner theorem from the isotropic Heisenberg model for magnetic systems states the impossibility of long-range magnetic orderings, as the ferromagnetic (FM) and antiferromagnetic (AFM), at a finite temperature in 2D systems due to thermal

---

1 Xu et al. 2013; Gupta, Sakthivel, and Seal 2015; Mas-Ballesté et al. 2011; Butler et al. 2013.

2 K S Novoselov et al. 2004.

3 Zhao et al. 2016.

4 Bianco et al. 2013.

5 Dean et al. 2010.

6 K. S. Novoselov et al. 2016.

fluctuations[7]. Notwithstanding, 2D magnetism has been recently demonstrated by experimental means in multiple materials[8].

Is appropriate to mention that the study of 2D magnetism has a long story[9], originating from the Ising theoretical model in 1944[10] for which magnetic orderings in 2D systems with a critical temperature $T_c > 0$. However, this formulation was considered a 'toy model' as it assumes a spin dimension of $n = 1$, in other words, all magnetic moments on the crystal are oriented along only one axis. As finding this magneto-crystalline condition on real materials has been uncommon the usual formulation for describing magnetic systems is the Heisenberg model which lacks angular anisotropy ($n = 3$)[11]. Despite this, the experimental proving of 2D materials with intrinsic magnetism indicates an Ising-like behaviour, and therefore, the Mermin-Wagner theorem is not applicable in this type of system. So that is evident that magnetic anisotropy plays a fundamental role in suppressing the thermal fluctuations, which originates from the quantum-relativistic effect of the spin-orbit coupling (SOC)[12].

Subsequently, after the discovery of 2D magnetic systems various methodologies were utilized for inducing magnetism in materials such as graphene and MoS_2[13]. These methodologies were the introduction of defects, proximity effects, straining, electric fields, etc. Nevertheless, the magnetic ordering generated through this methods is

---

7 Mermin and Wagner 1966.

8 B. Huang, Clark, Navarro-Moratalla, et al. 2017; Lee et al. 2016; Gong, Lin Li, et al. 2017; Fei et al. 2018.

9 Cortie et al. 2020.

10 Onsager 1944.

11 Gibertini et al. 2019.

12 Shabbir et al. 2018.

13 Miao and Z. Sun 2021; Cortie et al. 2020.

usually weak, short-ranged and hard to control in practice. The theoretical focus shifted towards materials with intrinsic 2D magnetism, taking as an approach the reduction of dimensionality of 3D magnetic materials. This proved fruitful as this led to the discovery of 2D van der Waals crystals which retained the magnetic ordering. As a result, this type of material has received great attention[14], as the presence of a weak interlayer interaction is beneficial for the exfoliation process. The first experimental demonstration was on the CrI_3 monolayers which hold an intrinsic ferromagnetic ordering[15] and belongs to the transition metal halide (TMH) family, which along the transition metal chalcogenides constitute the principal groups of compounds of this kind of materials[16].

The main aspects in the study of this family of crystals have been: material synthetization, magnetic characterization, modification methods, development of applications, *ab initio* calculation modelling and topological properties.

In the first place, advances in experimental techniques such as micromechanical exfoliation (CrI_3, $CrCl_3$, $Cr_2Ge_2Te_6$), chemical vapour deposition (Fe_3GeTe_2) and molecular beam epitaxial growth (VSe_2) have allowed the synthetization of magnetic 2D crystals[17]. Even so, there still are multiple obstacles to the preparation of this type of material, such as the synthesis speed control, stability under ambient conditions and obtainment of a more superficial area. Therefore, advances in this area are still needed.

---

[14] Cortie et al. 2020; X. Jiang et al. 2021; Shabbir et al. 2018; Gong and X. Zhang 2019; Gibertini et al. 2019; Samarth 2017; Park 2016; Sethulakshmi et al. 2019; Kin Fai Mak, J. Shan, and Ralph 2019; Miao and Z. Sun 2021; Burch, Mandrus, and Park 2018.

[15] B. Huang, Clark, Navarro-Moratalla, et al. 2017.

[16] X. Jiang et al. 2021; Kin Fai Mak, J. Shan, and Ralph 2019.

[17] P. Huang et al. 2020; Lee et al. 2016; B. Huang, Clark, Navarro-Moratalla, et al. 2017; Gong, Lin Li, et al. 2017; Fei et al. 2018.

In the second place, magnetic characterization of crystals has been possible by employing optical and electronic techniques, where it is necessary to use alternative methods to the commonly utilized for the case of 3D materials. The latter are the superconducting quantum interference devices (SQUID) or neutron diffraction methods, nevertheless, the needed samples for this kind of methods are too big in contrast to the ones obtained from exfoliation which are of micro-metrical order in area and width. In this manner, the optical techniques employed are those which allow a local measurement: spin-polarized scanning tunnelling microscopy (SP-STM), which takes advantage of the magneto-optical Kerr effect (MOKE)[18] and the x-ray magnetic circular dichroism. Additionally, techniques such as the measurement of the anomalous Hall effect (AHE) and anisotropic magneto-resistance are employed too, although, the necessity of contacts makes them more invasive[19].

In third place, for the application of this type of materials is essential to study the different methods of controlling and modifying their physical properties. Primarily, one important characteristic is the critical temperature of transition, for which values above ambient temperature are desirable[20]. The main modifications for this type of materials are through strain application[21], electric fields[22], magnetic fields, intercalation[23], the introduction of defects and optical control[24].

---

[18] Gibertini et al. 2019.

[19] Kin Fai Mak, J. Shan, and Ralph 2019.

[20] Hu et al. 2018; Zhong, Seyler, Linpeng, Cheng, et al. 2017; X. Jiang et al. 2021.

[21] Iyikanat et al. 2018; Webster and J. A. Yan 2018; Zheng et al. 2018.

[22] Nguyen et al. 2021; B. Huang, Clark, Klein, et al. 2018; S. Jiang, J. Shan, and Kin Fai Mak 2018.

[23] H. Wang et al. 2016; S. Jiang, Lizhong Li, et al. 2018.

[24] Y. Tian et al. 2019.

In the fourth place, concerning application development, due to the 2D nature of the systems the idea of piling up multiple monolayers of different materials in a single system to couple their properties arose. This type of system is called a van der Waals hetero-structure, which has found a place in multiple devices such as transistors, diodes, sensors and transmitters[25]. For this reason, the discovery of 2D magnetic vdW crystals is opportune, as it introduces magnetic phenomena, as well as, the possibility to develop spintronic devices[26]. Spintronic devices actively manipulate an intrinsic property of electrons, the spin, in order to transport and store information. Multiple devices based on CrI_3 monolayers have been proposed: spin filters, spin valves and multiferroic heterostructures[27].

In the fifth place, the theoretical study of these materials can be approached through *ab initio* [28] calculations. They constitute a powerful tool as they allow the modelling of materials and the prediction of their physical properties without the need of synthesizing them firsthand[29]. For example, the prediction of ferromagnetism in the CrI_3 in 2015[30] was presented 2 years before its synthetization and magnetic probing in 2017[31]. In particular, a theory that has been demonstrated to be extremely useful

[25] K. S. Novoselov et al. 2016; Yuan Liu et al. 2016.

[26] Choudhuri, Bhauriyal, and Pathak 2019; P. Huang et al. 2020; W. Zhang et al. 2019; Gong and X. Zhang 2019.

[27] S. Jiang, Xie, et al. 2020; Zhong, Seyler, Linpeng, Wilson, et al. 2020; Lu et al. 2020.

[28] In this context first principle calculations are those for which there is no need to introduce empirical parameters but from the physical fundamental laws.

[29] Miao and Z. Sun 2021.

[30] W. B. Zhang et al. 2015.

[31] B. Huang, Clark, Navarro-Moratalla, et al. 2017.

and as a consequence is broadly utilized is the density functional theory (DFT)[32]. This allows us to solve directly approximate forms of the many-body Schrödinger equation, and as a result, obtain solutions for which derived physical observables are well suited to the experimental measurements. Additionally, intending to expand the list of suitable 2D magnetic materials, the use of DFT has been the systematization of calculations through database filtering or high throughput, which has allowed the prediction of multiple compounds[33].

Finally, the last topic is a novel field of condensed matter physics, the study of topological materials. These are new phases of matter which present unique electronic transport where spin-orbit coupling and breaking of symmetries are required conditions. Particularly, in topological insulators (TI) the emergence of metallic edge states, and simultaneously, an insulating bulk is observed[34]. The discovery of this class of materials led to the expansion of the band theory of solids, to include concepts such as the Berry phase and curvature, which originate from the non-trivial topology of the electronic state space. This paradigm shift was needed to explain the appearance of physical observable phenomena, such as the quantum anomalous Hall (QAH) conductivity which is quantized in terms of a topological invariant and is not related to a quantum mechanical operator. Materials in which this last effect is presented are known as QAH topological phases or Chern Insulators and are 2D systems with broken time-reversal symmetry (TRS) associated with the presence of a dissipationless single spin conducting channel at the edge; characterized by a global

[32] Hohenberg and Kohn 1964; Kohn and Sham 1965.

[33] Hang Liu et al. 2018; Zhu et al. 2018; Z. Jiang et al. 2018; Mounet et al. 2018; "High throughput computational screening for 2D ferromagnetic materials: The critical role of anisotropy and local correlations (2D Materials 6 (045018)" 2020.

[34] Hasan and Kane 2010; Moore 2010; Ren, Qiao, and Niu 2016; Ando 2013; Qi and S. C. Zhang 2011; Klitzing, Dorda, and Pepper 1980.

property of the electronic structure, the Chern topological invariant (see Fig. 1).

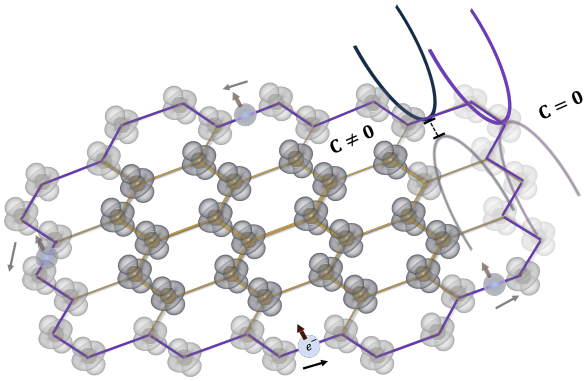

Figure 1. Chern Insulator topological phase illustration. In yellow is presented the hexagonal lattice, the density charge represents the ferromagnetic ordering, and the purple edge represents the edge state where only electrons with the same spin flow.

Consequently, the Chern Insulator phase due to the exhibition of robust filtered spin edge states in the absence of an external magnetic field presents itself as a promising candidate for novel applications in areas such as quantum computing and spintronics[35]. The search for this system has as starting point the theoretical model of Haldane in 1988[36]. This consists of a hexagonal honeycomb crystal lattice with SOC and intrinsic magnetism, such that this condition leads to a TRS breaking and the QAH effect is presented. Engineering of materials by inducing a magnetic field has been proposed, such as in graphene, germanene, stanene and silicene[37] through magnetic adatoms and surface functionalization, nevertheless, these conditions are hard to control in practice. The only experimental realizations of a Chern Insulator up to the present

[35] Qi and S. C. Zhang 2011.

[36] Haldane 1988.

[37] S.-C. Wu, G. Shan, and B. Yan 2014; Zhiyong Wang et al. 2015; X.-L. Zhang, L.-F. Liu, and W.-M. Liu 2013.

have been in V and Cr doped (Bi, Sb)$_2$Te$_3$[38] and MnBi$_2$Te$_4$[39], but the needed temperatures were low: $T < 100$ mK and $T < 6.4$ K respectively. In this manner, research for appropriate candidates is required to advance this field forward.

Therefore, in this research, we focused our efforts on the study from the DTF framework of the electronic, magnetic and topological properties of the osmium-based family of transition metal halides OsX$_3$ with X = Br, Cl, I. This selection was taken as they present the adequate properties for fulfilling a Chern insulator phase, it is, an hexagonal honeycomb lattice for the transition metal atoms, as in the Haldane model, and broken time-reversal symmetry originating from the intrinsic magnetism. Additionally, as the spin-orbit interaction is related to the atomic number with $\propto Z^4$, and for Os: Z=76 the SOC effect is significant; which would contribute to both the crystalline anisotropy and topological features. Other materials belonging to the transition metal halide compounds have been studied for their magnetic properties in recent years[40]. Concerning the topological properties the Chern insulator phase has been theoretically predicted in materials such as FeX$_3$ with X = Br, Cl, I[41], AX$_3$ with A = Pd, Pt and

[38] Chang et al. 2015.

[39] Deng et al. 2020.

[40] Cai et al. 2019; Lee 2016; P. Liu et al. 2017; J. Liu et al. 2018; Q. Sun and Kioussis 2018; J. Yan et al. 2019; Lado and Fernández-Rossier 2017; Xingzhi Wang et al. 2016; O'Hara et al. 2018; W. B. Zhang et al. 2015; W. X. Zhang et al. 2019; Nguyen et al. 2021; Bonilla et al. 2018; Webster and J. A. Yan 2018; McGuire 2017.

[41] L. Tian et al. 2019.

X = I, Br[42], VBr_3[43], $NiBr_3$[44], $NiCl_3$[45], ReX_3 with X = Br, I[46] and $PdCl_3$[47].

For this research, we utilized the crystalline structures obtained through a collaboration with prof Aldo H. Romero from West Virginia University, predicted through the Minima Hopping method. An algorithm that explores the minima of the potential energy surface to determine the stable configuration of a crystalline solid[48]. Initially, the structural relaxations were performed and the magnetic ordering configurations as well as lattice properties were found. We found that the theoretical approach, and therefore, the representation of the exchange-correlation into the calculations, is crucial to correctly reproduce the electronic states close to the Fermi level. Therefore, we focused deeply on the precise electronic structure description. The methodology carried out was through the utilization of Hybrid calculations, that although they involve a greater computational cost, are accurate for calculating strongly correlated materials[49]. Next, through a mapping of the electronic states to the Wannier function representation for the collinear case the exchange constants were calculated as well as a Curie temperature estimation. Finally, the topological properties were explored employing the CHERN software, an open-source contribution implemented by the author through a collaboration with prof Oleg Rubel from McMaster University.

---

[42] You et al. 2019; Jiaxiang Sun et al. 2020.

[43] Jiaxiang Sun et al. 2020.

[44] Jiaxiang Sun et al. 2020.

[45] J. He et al. 2017.

[46] e. a. Sun Q. 2019.

[47] Ya ping Wang et al. 2018.

[48] Goedecker 2004.

[49] Heyd, G. Scuseria, and Ernzerhof 2003.

The program was utilized on known materials that present topological features for validation purposes as well as in the OsX_3 family for computing the Chern number and Berryflux maps, and the results were compared to the obtained with the Z2PACK software.

Section 3.0

OBJECTIVES

3.1. GENERAL OBJECTIVE

Study the structural, electronic, magnetic and topological features of the Osmium based halide monolayers OsX_3 $(X : Cl, Br, I)$ through *ab initio* calculations based on the Density Functional Theory (DFT) framework.

3.2. SPECIFIC OBJECTIVES

1. To perform calculations to determine the minimum energy magnetic configuration for the structures from collinear magnetism.

2. To study the electronic structure of the materials and once included, the effect of Spin-Orbit Coupling (SOC).

3. To verify the GGA electronic structure with respect to the Hybrid functional results by determining the appropriate Hubbard U value.

4. To check the topological features, such as the Chern number and Berry curvature for the compounds.

Section 4.0

THEORETICAL FRAMEWORK

Condensed matter physics studies the theoretical models that predict the behaviour and properties of materials. to make a complete description of these is necessary to start from their fundamental components that require a quantum mechanical description. In the framework of this theory all the information of the physical systems is stored in the quantum states (wave functions $\psi(\mathbf{r})$ in the position representation), obtained from the solution of the Schrödinger equation. This equation governs their time evolution, but if we restrict our study to stationary states it is possible to find an equation only for the spatial coordinates: the time-independent Schrödinger equation. However, the analytical solution to this equation is limited to simple physical systems, in contrast to a material which can be considered as a collection of a large number of nuclei and electrons whose interactions are of a *Coulombian* nature. For this motive to theoretically describe the physics of materials it was necessary to develop theories and mathematical tools to deal with these complex systems.

Having said the above, the theory necessary to have carried out this work is presented in the following manner: Firstly, the Hamiltonian of the solid and the physical approximations required to arrive at a solvable form of the Schrödinger equation. Then, the density functional theory and its usefulness in finding the crystal wave functions, from which it is possible to determine the electronic structure[50]. Next, the exchange and correlation functionals[51] and the DFT+U correction[52]. Finally, the topology of

---

[50] Kaxiras and Joannopoulos 2019; Giustino 2014; Martin 2020; Vanderbilt 2018.

[51] Martin 2020; Jianwei Sun, Ruzsinszky, and J. Perdew 2015.

[52] Himmetoglu et al. 2013; Floris et al. 2020.

the electronic band structure, the concepts of phase, curvature and Berry connection, as well as their relationship with the Wannier functions[53]. Additionally, some topics related to the research but not central to it will be presented in the appendices, which are: the physical approximations taken to study a material 8.1, the spin-orbit coupling effect8.2, the crystal electronic wavefunctions 8.3, the quantum anomalous Hall effect 8.4 and the Wannier functions8.5.

4.1. HAMILTONIAN OF THE SOLID

The energy physical observable is associated with the Hamiltonian operator, whose form depends on the particular system and determines the wave functions $|\psi\rangle$, solutions of the time-independent Schrödinger equation

$$\hat{\mathrm{H}}|\psi\rangle = E_{tot}|\psi\rangle, \tag{1}$$

An eigenvalue equation for the stationary states, with total system energy E_{tot}. Now, to find the wave function $\Psi(\mathbf{r}, \mathbf{R})$ of a solid is necessary to consider all possible contributions to the energy [54]; so, the total Hamiltonian of the system can be written as

$$\hat{\mathrm{H}}(\mathbf{r}, \mathbf{R}) = \hat{\mathrm{T}}_{\mathrm{N}}(\mathbf{R}) + \hat{\mathrm{T}}_{\mathrm{e}}(\mathbf{r}) + \hat{\mathrm{V}}_{\mathrm{NN}}(\mathbf{R}) + \hat{\mathrm{V}}_{ee}(\mathbf{r}) + \hat{\mathrm{V}}_{\mathrm{eN}}(\mathbf{r}, \mathbf{R}), \tag{2}$$

here, a dependence on the position of the nuclei $\mathbf{R}$ and electrons $\mathbf{r}$ is presented. The first two terms of Eq. (2) correspond to the kinetic energy operators of the electrons

[53] Martin 2020; Vanderbilt 2018; Kaxiras and Joannopoulos 2019; Marzari et al. 2012.

[54] Contributions related to relativistic or fine structure corrections are neglected.

($\hat{\mathrm{T}}_{\mathrm{e}}$) and nuclei ($\hat{\mathrm{T}}_{\mathrm{N}}$), and are given by

$$\hat{\mathrm{T}}_e(\mathbf{r}) = -\frac{\hbar^2}{2m_e}\sum_i \nabla_i^2, \tag{3}$$

$$\hat{\mathrm{T}}_{\mathrm{N}}(\mathbf{R}) = -\frac{\hbar^2}{2}\sum_{\mathrm{I}} \frac{1}{\mathrm{M_I}}\nabla_{\mathrm{I}}^2, \tag{4}$$

Taking into account that the coordinates I,J refer to the nuclei with mass $\mathrm{M_I}$ and i, j to the electrons with mass m_e. On the other hand, the remaining three terms are the interaction potential energies *Coulombian* of the electrons with charge $-e$ in a position $\mathbf{r_i}$ and of the ions [55] with charge eZ_I in the position $\mathbf{R_I}$, which are the interactions of: ion-electron attraction ($\hat{\mathrm{V}}_{\mathrm{eN}}$), electron-electron repulsion ($\hat{\mathrm{V}}_{\mathrm{ee}}$) and ion-ion repulsion ($\hat{\mathrm{V}}_{\mathrm{NN}}$), given by.

$$\hat{V}_{eN}(\mathbf{r}, \mathbf{R}) = -e^2 \sum_{i,I} \frac{Z_I}{|\mathbf{r_i} - \mathbf{R_I}|}, \tag{5}$$

$$\hat{V}_{NN}(\mathbf{R}, \mathbf{R}) = \frac{e^2}{2}\sum_{I\neq J} \frac{Z_I Z_J}{|\mathbf{R_I} - \mathbf{R_J}|}, \tag{6}$$

$$\hat{V}_{ee}(\mathbf{r}, \mathbf{r}) = \frac{e^2}{2}\sum_{i\neq j} \frac{1}{|\mathbf{r_i} - \mathbf{r_j}|}. \tag{7}$$

So, replacing in the expression (2) and then $\hat{H}$ in the Schrödinger equation Eq. (1) gives

$$\left[-\sum_i \frac{\hbar^2}{2m_e}\nabla_i^2 - \sum_I \frac{\hbar^2}{2M_I}\nabla_I^2 + \frac{1}{2}\sum_{i\neq j}\frac{e^2}{|\mathbf{r}_i - \mathbf{r}_j|} + \frac{1}{2}\sum_{I\neq J}\frac{e^2 Z_I Z_J}{|\mathbf{R}_I - \mathbf{R}_J|} - \sum_{i,I}\frac{e^2 Z_I}{|\mathbf{r}_i - \mathbf{R}_I|}\right]\Psi = E_{\mathrm{tot}}\Psi, \tag{8}$$

[55] An ion is made up of the nucleus and the electrons closest to it, the separation is taken with the justification that the valence electrons are the ones that participate strongly in the interaction between atoms.

called the time-independent many-body Schrödinger equation, which contains everything necessary to study the behaviour of materials in equilibrium without considering the interaction with external electromagnetic fields. It should be noted that, in this equation the only external parameters are the atomic numbers Z_I and the atomic masses M_I.

4.2. DENSITY FUNCTIONAL THEORY (DFT)

This theory's fundamental premise is that any property of a system of many interacting particles can be described as a functional[56] of the density $n(\mathbf{r})$ of the ground state, i.e., that all the information of the wave functions is determined by the scalar function $n(\mathbf{r})$ which depends only on the position. This hypothesis was demonstrated by Hohenberg and Kohn[57], and a scheme for applying this theory was developed by Kohn and Sham[58].

Starting from the definition of the total electron density $n(\mathbf{r})$ for a system with N electrons

$$n(\mathbf{r}) = N \int \left|\Psi\left(\mathrm{r}, \mathrm{r}_2, \ldots, \mathrm{r}_N; \mathbf{R}_1, \ldots, \mathbf{R}_M\right)\right|^2 d\mathbf{r}_2 \ldots d\mathbf{r}_N d\mathbf{R}_1 \ldots d\mathbf{R}_M, \tag{9}$$

and represents the probability of finding any electron at the $\mathbf{r}$ position. Therefore, if the relationship in Eq. (55) is inverted, the dependence of Ψ on the density $n(\mathbf{r})$ becomes evident, i.e., $\Psi = \mathcal{F}[n]$, which is a significant idea, since it suggests that it is possible to find the wave functions by defining a functional of the electron density, reducing the 3N variable problem to only the $\mathbf{r}$ position. Likewise, looking at

[56] A functional is a function that maps a function to a number.

[57] Hohenberg and Kohn 1964.

[58] Kohn and Sham 1965.

Eq. (53), since $\hat{H}$ does not depend on a particular material, any variation of E must be associated with changes in the wavefunction Ψ, so that

$$\Psi = \mathcal{F}[n] \quad y \quad E = \mathcal{F}[\Psi] \quad \longrightarrow E = \mathcal{F}[n].$$

As stated in the theorem of Hohenberg and Kohn:

Theorem: The ground state energy of the Schrödinger equation is a unique functional of the electron density[59].

This can be proved by *reductio ad absurdum*, by proposing that there is a one-to-one relationship between the electron density and the external potential to which the electrons are subjected[60]. However, the Hohenberg and Kohn theorems do not indicate the exact form the functional must possess, which is unknown up to now. This problem was addressed by Kohn and Sham[61], whose idea was to construct the functional from the mapping to a system of non-interacting fictitious particles, taking the approximation of a single particle, as in Eq. (51). So the functional for the energy $\mathcal{F}[n]$ was redefined from (53), such that

$$F[n] = \int d\mathrm{r} n(\mathrm{r}) V_{\mathrm{n}}(\mathrm{r}) + \langle \Psi[n] | \hat{T} + \hat{W} | \Psi[n] \rangle, \tag{10}$$

obtaining by replacing the terms

$$F[n] = \int d\mathbf{r} n(\mathbf{r}) V_{\mathrm{n}}(\mathrm{r}) - \sum_i \int d\mathbf{r} \phi_i^*(\mathrm{r}) \frac{\hbar^2 \nabla^2}{2m} \phi_i(\mathrm{r}) + \frac{1}{2} \iint d\mathrm{r} d\mathrm{r}' \frac{n(\mathrm{r}) n(\mathrm{r}')}{|\mathrm{r} - \mathrm{r}'|} + E_{xc}[n]. \tag{11}$$

Here, the first term represents the potential energy, the second the kinetic energy,

[59] Hohenberg and Kohn 1964.

[60] Hohenberg and Kohn 1964.

[61] Kohn and Sham 1965.

the third the Hartree energy and the last is called the correlation and exchange term. The latter contains all the information concerning these two electron interactions. In summary, Eq. (11) constructs the functional from the known contributions, taken from the independent electron approximations and an unknown contribution, the correlation and exchange term.

Now, to find the equations to be solved the Hohenberg-Kohn variational principle[62] is employed, which indicates that the electron density of the ground state, n_o, is the function that minimizes the total energy $E = \mathcal{F}$, i.e.

$$\left.\frac{\delta F[n]}{\delta n}\right|_{n_0} = 0. \tag{12}$$

Therefore, starting from the expression (12), it is possible to obtain an equation for the wave functions $\phi_i(\mathbf{r})$, for which the condition of orthonormality can be imposed through a Lagrange multiplier (see appendix B of reference[63]), and as a result, the obtain the expression

$$\left[-\frac{\hbar^2}{2m}\nabla^2 + V_{\mathrm{n}}(\mathbf{r}) + V_{\mathrm{H}}(\mathbf{r}) + V_{xc}(\mathbf{r})\right]\phi_i(\mathbf{r}) = \varepsilon_i\phi_i(\mathbf{r}), \tag{13}$$

where the terms V_n, V_H are identical to those found in Eq. (50) and Eq. (52), respectively; and the term V_{xc} is given by.

$$V_{xc}(\mathbf{r}) = \left.\frac{\delta E_{xc}[n]}{\delta n}\right|_{n(\mathbf{r})}, \tag{14}$$

Called the exchange and correlation potential [64]. The set of equations (14) are known

[62] Hohenberg and Kohn 1964.

[63] Giustino 2014.

[64] This is the only non-exact term in DFT, the cost of simplifying the equations to be solved is to find

as the Kohn-Sham equations, which must be solved through a self-consistent iterative method; and are the basis for performing material property calculations in DFT. It is worth mentioning that, although there is no formal mathematical justification for relating these wave functions to the quantum states of the electrons, experimental evidence has shown that the properties calculated with them fit to a reliable extent so that they can be considered reasonable descriptions of the electronic states.

4.2.1. EXCHANGE AND CORRELATION FUNCTIONALS

The accuracy of the density functional theory depends on a properly constructed correlation and exchange functional. For this reason, since the introduction of the Kohn-Sham theory, abundant efforts have been devoted to developing functionals that properly represent the physical systems under study. The importance of the term $E_{xc}(n)$ is the fact that all interactions associated with the many-body nature are embodied in it, making it depend on multiple positions, i.e., to be non-local. However, this would imply introducing more complexity to the solution of the system, so it has been seeking to develop local functionals that best describe these effects.

Initially, the local density approximation (LDA) was developed and uses the calculated value of the correlation and exchange energy of a homogeneous electron gas [65] to describe this energy in materials; this is by the calculation in regions where the density varies slowly and finding the final value by summing all the contributions.

After this, the generalized gradient approximation (GGA) was developed, whose functional takes into account the magnitude of the density gradient $|\nabla n|$, as well as the value of n at each point in space, leading to better results in the obtained electron density.

---

a sufficiently precise functional for the description

[65] Consists of the free electron gas, but taking into account the interactions. The exchange term can be calculated analytically, while the correlation term parameterized numerically.

Next, one notch higher in the hierarchy of approximations[66] are the meta-GGAs; which are functionals of the kinetic energy density of non-interacting particles, as well as of the particle density[67].

Finally, one of the most accurate exchange and correlation functionals are the Hybrid type. They are a mixture of density-dependent functionals and the Hartree-Fock (HF), which is orbital dependent. The advantages given by these methods is an improvement of the band gap estimation, as LDA and GGA methods tend to underestimate them. The general form of the Hybrid functionals exchange and correlation energy is

$$\mathrm{E_{xc}} = \alpha \mathrm{E_x^{HF}} + (1-\alpha)\mathrm{E_{xc}^{DFT}}, \tag{15}$$

here, $\mathrm{E_{xc}^{DFT}}$ refers to the density-dependent functional, and α is the mixing parameter, which varies from full Hartree-Fock interacting ($\alpha = 1$) and non-interacting electron system ($\alpha = 1$). Multiple forms for the hybrid functionals have been developed, such as the B3LYP[68] which is adjusted to fit atomic and molecular data and the PBE0[69] which employs a non-linear form

$$E_{\mathrm{xc}}^{\mathrm{PBE0}} = E_{\mathrm{xc}}^{\mathrm{PBE}} + \frac{1}{4}\left(E_x^{\mathrm{HF}} - E_{\mathrm{x}}^{\mathrm{PBE}}\right) \tag{16}$$

and uses the PBE density functional and is widely used. Particularly, the hybrid Heyd-Scuseria-Ernzerhof exchange and correlation functional HSE06[70], utilizes a screen

---

66 In this context the hierarchy is called 'Jacob's ladder', a term introduced by J.P Perdew (John P. Perdew 2001)

67 Jianwei Sun, Ruzsinszky, and J. Perdew 2015.

68 A D Becke 1988; Axel D Becke 1993.

69 John P Perdew, Ernzerhof, and Burke 1996.

70 Krukau et al. 2006; Heyd, G. E. Scuseria, and Ernzerhof 2003.

Coulomb potential. This starts from the exchange portion of the PBE0 Eq. 16 and there is a separation of terms into short (SR) and long range (LR) components, obtaining

$$E_x^{PBEO} = a\left[E_x^{HF,SR}(\omega) + E_x^{HF,LR}(\omega)\left[+(1-a)\left[E_x^{PBE,SR}(\omega) + E_x^{PBE,LR}(\omega)\right]\right.\right. . \quad (17)$$

This method is based on the idea that the Coulomb screening is a function of the distance being weak at short and larger as distance increases. In this case ω is an adjustable parameter which dictates the contribution between SR and LR interactions.

4.2.2. DFT + U

In systems with highly localized orbitals (d or f electrons), the description of the electronic structure found by employing DFT is not very accurate, due to the lack of specification of the correlation and exchange energy. Consequently, the idea of DFT+U is to describe these highly correlated electronic states using the Hubbard model, while treating the other valence electrons with the standard DFT functionals. In this case, the total energy of the system is written in the following way

$$E_{\mathrm{DFT+U}}[n(\mathrm{r})] = E_{\mathrm{DFT}}[n(\mathrm{r})] + E_{\mathrm{Hub}}\left[\left\{\rho_{mm'}^{l\sigma}\right\}\right] - E_{\mathrm{dc}}\left[\left\{n^{l\sigma}\right\}\right]. \quad (18)$$

Here, E_{DFT} represents the functional for the total DFT energy to be corrected and E_{Hub} is the term containing the Hubbard Hamiltonian to describe the correlated states. Additionally, it is necessary to remove the energy portion of the 'original' functional E_{DFT}, which will be characterized by the E_{Hub}; is done employing the double counting term E_{dc} that models the contribution of the correlated electrons to the DFT energy. Lastly, $\rho_m^{l\sigma}$ are the occupancy numbers of the localized orbitals.

4.3. TOPOLOGY OF THE ELECTRONIC STRUCTURE

The Born rule in quantum mechanics indicates that the probability of measurement of an eigenvalue associated with an observable is given by the square of the norm of the corresponding quantum amplitude, in a manner that the phase does not affect the measurement. Likewise, in electronic structure theory, a large number of properties of interest can be found as expected values of the Bloch states (total energy, charge densities, strengths, etc.); which when calculated, the total phase multiplying each Bloch state cancels. For this reason, the phase of the electronic states was not considered to be relevant. However, through the investigation of multiple phenomena, such as electric polarization, it has been found that the phase plays a fundamental role. Whereas the general phase of a Bloch function is not that which has utility, but the relative phase between states at close time intervals or for close wave vectors. Thus, it is necessary to introduce the formalism of a geometric or Berry phase and related quantities such as the Berry curvature which embody the underlying topology of the Bloch bands. Additionally, they are directly related to physical phenomena in which there is a quantization of certain observables that cannot be associated with any operator, such as the quantum anomalous Hall effect (see 8.4).

4.3.1. BERRY PHASE, CONNECTION AND CURVATURE

In general, the Berry phase is a phase angle between 0 and 2, which describes the evolution of the phase of a vector in a complex vector space as a function of some parameter or set of parameters as it is transported through a closed trajectory in its vector space. In the particular case of solid-state physics, it arises when the vectors [71] are the occupied Bloch states $|\phi_{\mathbf{k}}^{(n)}\rangle$ and the parameter space corresponds to the

[71] The first postulate of quantum mechanics is that the quantum states of a system are described

components of the wave vector $\mathbf{k}$ in the Brillouin zone (which as mentioned forms a closed space) for a band n. To define this phase we will then perform the analysis of the adiabatic evolution of a general physical system, and from this, we will present the expressions for the case of the electronic states in a crystal.
By defining a parametric Hamiltonian such that

$$\hat{H}(\mathbf{q})\,|\psi_{\mathbf{q}}\rangle = E_{\mathbf{q}}\,|\psi_{\mathbf{q}}\rangle\,, \tag{19}$$

where $\mathbf{q}$ is some parameter that can be associated with multiple characteristics of a system. We know that when solving the Schrödinger equation for the wave function of the system, an arbitrary phase φ of the form $e^{i\varphi}$ appears, assuming we deal with the system in the ground state, it is generally chosen equal to zero, for simplicity. Considering that this phase for two base states of the system, identified by different values of the parameter $\mathbf{q}$, takes the values φ_1 and φ_2 for the values of the parameter $\mathbf{q}_1$ and $\mathbf{q}_2$, respectively; if one wanted to eliminate the phase for each case it would be necessary to multiply each wave function by $e^{-i\varphi_i}$, with the corresponding i, i.e.

$$|\psi_{\mathbf{q}_i}\rangle \to |\tilde{\psi}_{\mathbf{q}_i}\rangle = e^{-i\varphi_i}\,|\psi_{\mathbf{q}_i}\rangle\,, \tag{20}$$

this process is called 'selecting a gauge'. Then, the overlap of the wave functions with the corrected phase would be.

$$\left\langle \tilde{\psi}_{\mathbf{q}_1} \mid \tilde{\psi}_{\mathbf{q}_2} \right\rangle = e^{\mathrm{i}(\varphi_1-\varphi_2)}\,\langle \psi_{\mathbf{q}_1} \mid \psi_{\mathbf{q}_2}\rangle\,, \tag{21}$$

In this expression any dependence on an arbitrary phase has been eliminated, therefore, the term on the left must be the magnitude of the overlap: $|\langle \psi_{\mathbf{q}_1} \mid \psi_{\mathbf{q}_2}\rangle|$; which al-

entirely through vectors belonging to a Hilbert space (Cohen-Tannoudji, Diu, and Laloe 2020)

lows us to find a convenient expression to define the relative phase $\Delta\varphi_{12} = (\varphi_1 - \varphi_2)$ as

$$\mathrm{e}^{-\mathrm{i}\Delta\varphi_{12}} = \frac{\langle\psi_{\mathbf{q}_1} \mid \psi_{\mathbf{q}_2}\rangle}{|\langle\psi_{\mathbf{q}_1} \mid \psi_{\mathbf{q}_2}\rangle|}. \tag{22}$$

then, by separating the real and imaginary parts, it is possible to obtain the phase of the expression

$$\Delta\varphi_{12} = -\operatorname{Im}\left[\ln\left(\langle\psi_{\mathbf{q}_1} \mid \psi_{\mathbf{q}_2}\rangle\right)\right], \tag{23}$$

that in the limit of a differential $\Delta\mathbf{q}$ between $\mathbf{q}_1$ and $\mathbf{q}_2$, corresponding to a change in the phase $\Delta\varphi$, we obtain the expression

$$\mathrm{d}\varphi = \mathrm{i}\,\langle\psi_{\mathbf{q}} \mid \nabla_{\mathbf{q}}\psi_{\mathbf{q}}\rangle\,\mathrm{dq}. \tag{24}$$

Such that, with Eq. (24), it is possible to calculate the total change in phase (Berry's phase γ) along a closed trajectory C in $\mathbf{q}$ parameter space as

$$\gamma = \oint_C \mathrm{d}\varphi = \mathrm{i}\oint_C \langle\psi_{\mathbf{q}} \mid \nabla_{\mathbf{q}}\psi_{\mathbf{q}}\rangle\,\mathrm{dq} \tag{25}$$

This expression is invariant under gauge transformations (such as the one performed in Eq. (20)), in contrast to the integrand that does depend on the chosen *gauge*, which demonstration is beyond the scope of the thesis but can be found in the references. Now, from the expression found is possible to define the integrand

$$\mathcal{A}(\mathbf{q}) = \mathrm{i}\,\langle\psi_{\mathbf{q}} \mid \nabla_{\mathbf{q}}\psi_{\mathbf{q}}\rangle, \tag{26}$$

as Berry's Connection, which is a three-component vector, and from this, define the tensor

$$\Omega_{\alpha\beta}(\mathbf{q}) = \frac{\partial\mathcal{A}_\beta(\mathbf{q})}{\partial q_\alpha} - \frac{\partial\mathcal{A}_\alpha(\mathbf{q})}{\partial q_\beta} = -2\operatorname{Im}\left\langle\frac{\partial\psi_{\mathbf{q}}}{\partial q_\alpha} \mid \frac{\partial\psi_{\mathbf{q}}}{\partial q_\beta}\right\rangle \tag{27}$$

whose elements can be associated with the components of a vector $\mathbf{\Omega}$, known as the

Berry Curvature, by using the Levi-Civita tensor $\epsilon_{\alpha\beta\gamma}$. So that, this can be written as the rotational of $\mathcal{A}$, i.e.

$$\mathbf{\Omega}(\mathbf{q}) = \nabla \times \mathcal{A}(\mathbf{q}). \tag{28}$$

Then, with these definitions, it is possible to rewrite the expression for the Berry phase (25) by making use of Stokes' theorem

$$\gamma = \oint_C \mathcal{A}(\mathbf{q}) \cdot \mathrm{d}\mathbf{q} = \int_{\mathcal{S}} \nabla_{\mathbf{q}} \times \mathcal{A}(\mathbf{q}) \cdot \mathrm{d}\mathcal{S} = \int_{\mathcal{S}} \mathbf{\Omega}(\mathbf{q}) \cdot \mathrm{d}\mathcal{S} \tag{29}$$

where, $\mathcal{S}$ is the surface enclosed by the curve $\mathcal{C}$ and dS is a surface differential element. So, the Berry curvature Ω is the Berry phase γ per unit area in the parameter space $\mathbf{q}$; and is obtained as the rotational of the Berry connection $\mathcal{A}$.

Finally, from the Berry curvature Ω, it is possible to obtain the topological invariant associated with the states $|\psi_{\mathbf{q}}\rangle$ defined on the surface S, known as the first Chern number C; which is consigned in Chern's theorem:

$$\oint_S \Omega \cdot d\mathbf{S} = 2\pi C. \tag{30}$$

The calculation of the Chern topological invariant given by the integration over the occupied bands, determines a global property of the bulk bands, expressed in terms of the Berry curvature which is a local property related to the geometry of the electronic states across the BZ.

4.3.2. TOPOLOGICAL FEATURES OF THE CRYSTAL ELECTRONIC STATES

As already mentioned, the parameter that characterizes the Hamiltonian of the system and the states is the wave vector $\mathbf{k}$, so by using the definitions [(25),(26) y (28)] for the periodic Bloch states $|u_{\mathbf{k}}^{(n)}\rangle$ presented in Appendix. 8.3, we obtain the following expressions

$$\mathcal{A}^{(n)}(\mathbf{k}) = \mathrm{i}\left\langle u_{\mathbf{k}}^{(n)} \mid \nabla_{\mathbf{k}} u_{\mathbf{k}}^{(n)} \right\rangle, \tag{31}$$

$$\Omega^{(n)}(\mathbf{k}) = \nabla_{\mathbf{k}} \times \mathrm{i}\left\langle u_{\mathbf{k}}^{(n)} \mid \nabla_{\mathbf{k}} u_{\mathbf{k}}^{(n)} \right\rangle, \tag{32}$$

$$\gamma^{(n)} = \oint_C \mathrm{i}\left\langle u_{\mathbf{k}}^{(n)} \mid \nabla_{\mathbf{k}} u_{\mathbf{k}}^{(n)} \right\rangle \mathrm{d}\mathbf{k}, \tag{33}$$

where the closed trajectory is taken in reciprocal space. These properties are intrinsic to the band structure since they depend on the electronic states. Moreover, as in the general case, one is free to perform gauge transformations such as

$$\left|\tilde{u}_{\mathbf{k}}^{(n)}\right\rangle = e^{-i\beta(\mathbf{k})}\left|u_{\mathbf{k}}^{(n)}\right\rangle \tag{34}$$

where, $\beta(\mathbf{k})$ is a real function, the Berry connection

$$\tilde{\mathbf{A}}^{(n)}(\mathbf{k}) = \mathbf{A}^{(n)}(\mathbf{k}) + \nabla_{\mathbf{k}}\beta(\mathbf{k}) \tag{35}$$

if it depends on the *gauge*; and the Berry curvature $\Omega^{(n)}(\mathbf{k})$ being the rotational of the Berry connection is invariant. Likewise, for the 2D case, the first Chern number for the n-band is invariant under this *gauge* and can be calculated as

$$C^{(n)} = \frac{1}{2\pi}\int_{\mathrm{BZ}} \Omega_{xy}^{(n)} d^2k. \tag{36}$$

Thus, since the Chern number is an integer then the Berry phase for a trajectory along the Brillouin zone is an integer multiple of 2π, which yields an invariant of the wave function. Additionally, some properties of the Berry curvature $\Omega^{(n)}(\mathbf{k})$ for an n-band, which is a well-defined function in the Brillouin zone, are

- If the crystal has symmetry inversion (SI), then $\mathbf{\Omega}^{(n)}(\mathbf{k}) = \mathbf{\Omega}_n(-\mathbf{k})$.

- If the crystal has time-reversal symmetry (TRS), then $\mathbf{\Omega}^{(n)}(\mathbf{k}) = -\mathbf{\Omega}_n(-\mathbf{k})$.
- If the crystal has both IS and TRS, then $\Omega^{(n)}(\mathbf{k}) = 0$.

From this, it is inferred that Berry curvature is of interest in systems that exhibit spontaneous time-reversal symmetry breaking, as in the case of a ferromagnetic system.

Section 5.0

RESULTS AND DISCUSSION

5.1. STRUCTURAL PROPERTIES

In Fig. 2(a) is presented the crystalline structure of the OsX_3 monolayer family. It is a honeycomb lattice found to belong to the $P\bar{3}1m(162)$ space group. The Os atoms present a hexagonal organization and are coordinated with six halide atoms at a constant distance. Where a layer of Os atoms is in between two sheets of halide atoms, and the unit cell consists of 2 Os atoms and 6 halides(Cl, Br, I).

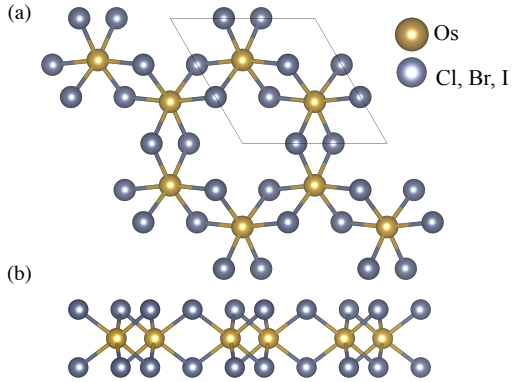

Figure 2. The crystalline structure of the OsX_3 monolayer. Yellow spheres represent the Os atoms and the blue spheres the halide atoms (Cl, Br, I) (a) Top view and (b) lateral view of the monolayer, the lines represent the unit cell.

Initially, to obtain the lattice parameters and atomic positions the structures were optimized in the in-plane directions (x and y), taking into account a vacuum distance of 20 Å to avoid interlayer coupling. The results obtained for the lattice constants and Os-Os distance are presented in Fig. 3.b, where an increasing trend is observed with respect to the atomic number $Z_{Cl,Br,I}$ of the halide atom (see Fig. 3.a). This tendency is also presented for the monolayer width as the corresponding values found

are $OsCl_3$:2.616 Å, $OsBr_3$:2.788 Å and OsI_3:3.024 Å. The obtained results for the lattice parameters agree with other DFT studies on the OsI_3 monolayer with a relative difference of -1.72%[72] and -0.23%[73] and for the $OsCl_3$ case 0.49%[74].

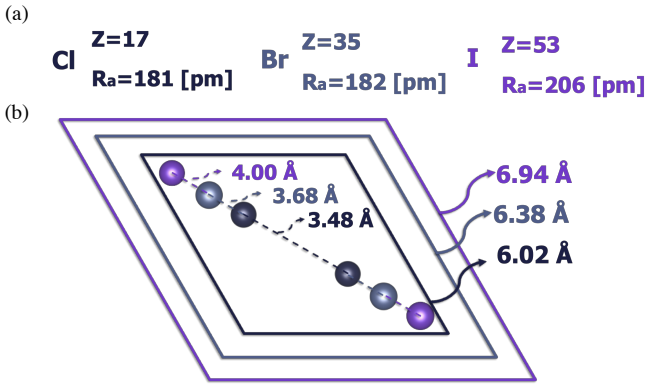

Figure 3. (a)Halide atomic number and ionic radius (b) Visual representation of the lattice parameter and Os-Os distance for the monolayer family.

Additionally, it can be seen that the results found via DFT mostly agree with the geometric Pauling rules for possible coordinations of a cation by anions[75]. Whereof, assuming that atoms are spheres in contact, the ratio between ionic radii implies

$$\frac{r_c}{r_a} > 0.732 \longrightarrow cubic,$$

$$0.414 < \frac{r_c}{r_a} < 0.732 \longrightarrow octahedral,$$

$$\frac{r_c}{r_a} < 0.414 \longrightarrow tetrahedral.$$

In this manner, taking into account that the ionic radius of the atoms are: Os($77pm$),

[72] L. Tian et al. 2019.

[73] Fang et al. 2022.

[74] Sheng and Nikolić 2017.

[75] e. a. Bercioux 2018; Pauling 1929.

Cl(181 pm), Br(182 pm) and I(206 pm)[76], then the ratios for the compounds are

$$\frac{r_{Os}}{r_{Cl}} = \frac{77}{181} = 0.425, \qquad \frac{r_{Os}}{r_{Br}} = \frac{77}{182} = 0.423, \qquad \frac{r_{Os}}{r_{I}} = \frac{77}{206} = 0.373,$$

such that the compounds follow the empirical coordination rules except for the OsI_3 case. Moreover, from the DFT ionic optimization results, it was possible to observe an angle distortion from the octahedral coordination of the halides with the Os atom, as presented in Fig. 4. For the case of $OsCl_3$ and $OsBr_3$ monolayers, there is a slight change and similar behaviour, nevertheless, for OsI_3 a more noticeable distortion from the octahedra is evidenced.

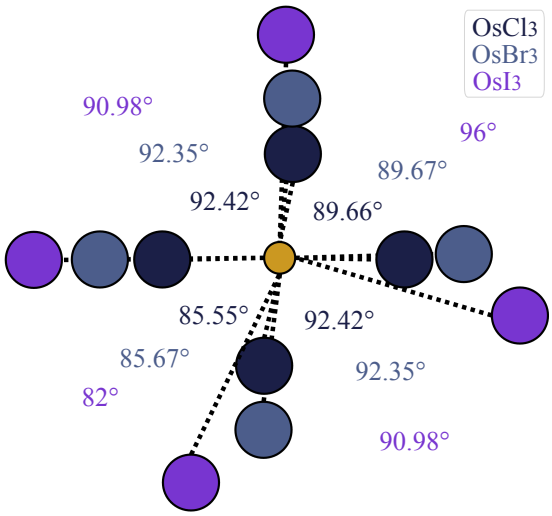

Figure 4. Distortion from the octahedral coordination of the OsX_3 monolayers

Finally, the energetic favorability of the monolayers was investigated through the cohesive energy E_c per unit cell, given by

$$E_c = (E_T - 2E_{Os} - 6E_X)/8, \tag{37}$$

[76] Shannon 1976.

which is the difference between E_T, the total energy of the OsX_3 monolayer, and E_{Os} and E_X the free Os and halide atom energies per atoms in the unit cell, respectively. For this calculation, the energies of the spin-polarized free atoms were found by employing an $8 \times 8 \times 8$ Å^3 computational cell. The results for the monolayers cohesive energies are presented in Table. 1. Here, the negative energies indicate a preference for the condensed phase formation and are all lower than the theoretically calculated for the CrI_3:-2.30 eV case, which has already been synthesized[77]. An increasing trend for E_c according to the halide atomic number $Z_{Cl,Br,I}$ can be observed. This can be explained by the electronic charge transfer trend found in Sec. 5.3, where a loss in the ionicity was found following the same tendency. In other words, the cohesive energy increases as the compounds are less ionic, therefore, being easier to dissociate the electronic bonds. Lastly, the structural information is presented in Table. 1.

Material	**a(Å)**	$\mathbf{d_{Os-Os}}$**(Å)**	$\mathbf{d_{Os-X}}$**(Å)**	**Width (Å)**	α **Os-X-Os °**	$\mathbf{E_c}$ **eV/atom**
$OsCl_3$	6.02	3.48	2.37	2.616	94.45	-3.513
$OsBr_3$	6.38	3.68	2.51	2.788	94.32	-2.879
OsI_3	6.94	4.00	2.67	3.024	97.50	-2.486

Table 1. Structural properties of the OsX_3 monolayers.

5.2. MAGNETIC PROPERTIES

To determine the magnetic ground state of the OsX_3 monolayers the ionic relaxation for the configurations presented in Fig. 5 were simulated. It was found that for the three compounds the lowest energy case was the ferromagnetic (FM) ordering. The stability difference between the configurations, found at the GGA+U PBSEsol level, is given by the magnetic exchange energy, $\Delta E = E_{FM} - E_{AFM}$, with the following

[77] F. Zhang, W. Mi, and Xiaocha Wang 2020; B. Huang, Clark, Navarro-Moratalla, et al. 2017.

obtained values: $OsCl_3$:24 meV, $OsBr_3$:11.9 meV and OsI_3:173.5 meV.

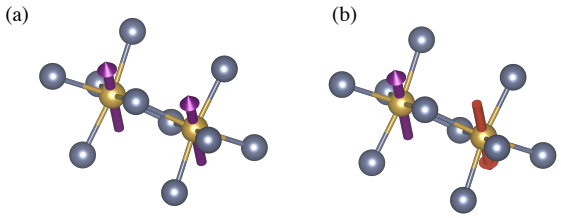

Figure 5. Initial magnetic moment configurations simulated for the OsX_3 (a)ferromagnetic and (b) antiferromagnetic ordering

In Fig. 6 the spin and orbital magnetic moments per unit cell are presented as a function of the Hubbard U parameter employing the PBEsol exchange and correlation functional; for which the final values selection is justified in the following section 5.3. For the case of the spin magnetic moments, in Fig. 6 the dashed lines represent the value found for the Hybrid calculations taken as reference, and it is evident that there is a good agreement for the PBEsol values by employing the U correction. It is worth noting that in all the cases when there is a complete absence of correlation adjustment, the values are far off and undergo a transition as U increases. Henceforth, the U correction is vital for obtaining the correct magnetic properties. Finally, the results obtained for the orbital magnetic moments are considerable, being larger than the originating from spin. These results are due to the elevated value of the SOC for the atoms in the monolayers.

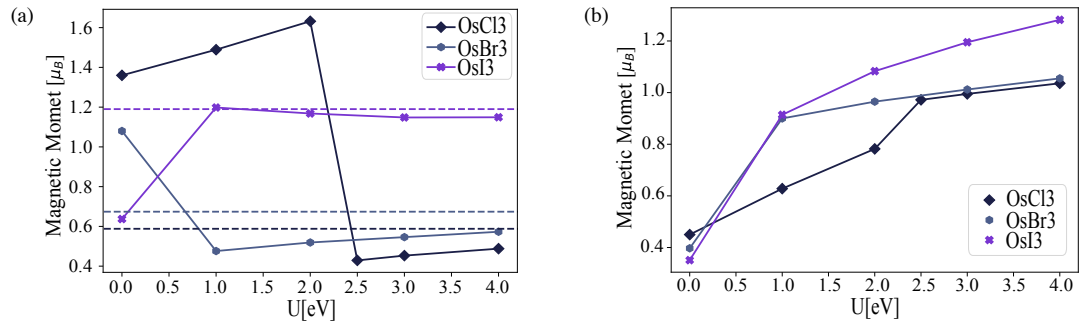

Figure 6. Values obtained for the magnetic moments for the PBEsol calculations as a function of the U parameter. (a) Spin magnetic moments, where the dashed lines represent the magnetic moments from HSE06 hybrid calculations (b) Orbital magnetic moments

The valence electrons of the Os atom belong to the orbitals $5p^6 6s^2 5d^6$, such that for the formula unit OsX_3 the expected occupation would be $5d^5$. Taking into account the geometrical organization of the atoms and the interaction of the d electrons with the halide orbitals, given the octahedral coordination this results in a Crystal field splitting which raises the energy degeneracy of the d electron states. The 5d orbitals are separated into a higher energy doublet e_g and a lower energy triplet t_{2g} as shown in Fig. 7.

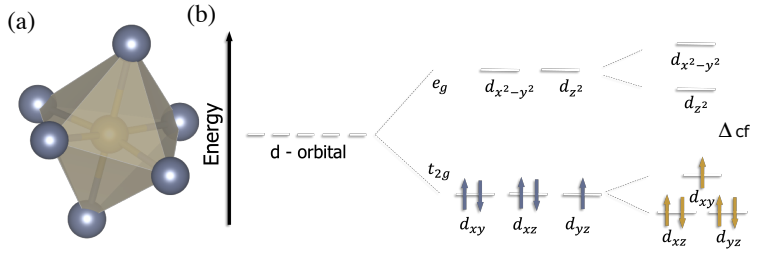

Figure 7. Crystal field splitting for the octahedral coordination. From the d orbitals, the eg and t2g originate with a low spin configuration groundstate.

Now, in isolated atoms, Hund's rule implies that the electrons occupy levels such that they posses the largest possible total spin to minimize the interaction between them, as given for the Pauli exclusion principle. For the case of t_{2g} levels the first 3 electrons occupy 3 parallel spin states, but for the 2 remaining electrons, there is a correlation

problem. As the options are to occupy the e_g levels with a parallel spin to the t_{2g} states, obeying Hund's rule (high spin configuration). Nevertheless, this implies an energy cost Δ_{cf} as they must occupy the high energy e_g levels. The alternative is to fill the t_{2g} levels with an opposite spin, and in this manner, gaining the Δ_{cf} energy, but losing Hund's energy (low spin configuration). The low spin configuration is typical for 4d and 5d compounds, due to the large extent of d orbitals and the greater hybridization with the p orbitals (greater Δ_{cf} value)[78]. Hence the expected electron occupation given the found magnetic moments in Fig. 6 is the one given in Fig. 7. Additionally, this non-symmetrical distribution of down-spin electrons in the t_{2g} levels contributes to the large orbital magnetic moments found in Fig. 6.

The Crystal field splitting originates both from the d-p orbital hybridization (covalency) and the tendency of the system to minimize the energy by reducing the electron-electron Coulomb repulsion. This last contribution can be evidenced as the most energetically favourable electronic states are those in which the overlapping of charge density between Os electrons and the halide's orbitals is reduced, by the positioning of the lobes in between the ligands (t_{2g}). In contrast, the states with lobes pointing directly to the p orbitals of the halide (e_g) increase in energy, as presented in Fig. 8.

[78] Khomskii 2014.

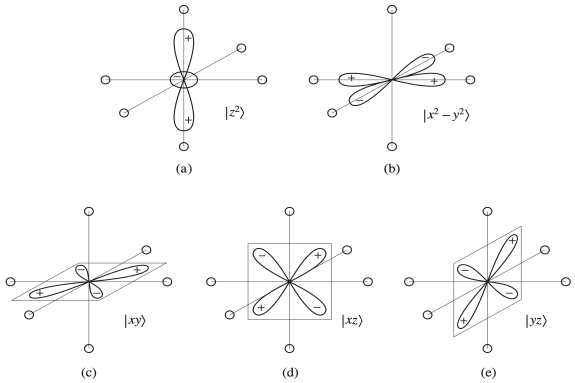

Figure 8. Illustration of the electron densities of orbitals (a,b) e_g and (c,d,e) t_{2g}. Reference:[79]

On the other hand, in the covalency contribution case, for transition metals to the crystal field splitting increases with the atomic number $Z_{Cl,Br,I}$[80]. Therefore for the Os (Z=76), it is expected to be important. Nevertheless, for the case of the anions, the covalency tendency related to the ligand strength follows the spectrochemical series[81]

$$\begin{aligned} \mathrm{I}^- < \mathrm{Br}^- < \mathrm{S}^{2-} < \mathrm{Cl}^- < \mathrm{NO}_3^- < \mathrm{F}^- < \mathrm{OH}^- < \mathrm{O}^{2-} \\ < \mathrm{H_2O} < \mathrm{NH_3} < \mathrm{NO}_2^- < \mathrm{CN}^- < \mathrm{CO}, \end{aligned} \tag{38}$$

where it can be observed that the crystal field splitting contribution should be low for our halides case as they are weak ligands (left side of the series).

Another important feature of ferromagnetic systems is the temperature dependence of magnetization, which indicates the possibility of utilizing materials in realistic environments. The magnetization vanishes at the Curie temperature

$$T_C = \frac{2Z\mathcal{J}S(S+1)}{3k_B}, \tag{39}$$

[80] Khomskii 2014.

[81] Tsuchida 1938.

here Z is the number of nearest magnetically active neighbours, S the spin quantum number, k_B Boltzmann constant and $\mathcal{J}$ the Heisenberg exchange constant from the Heisenberg Hamiltonian

$$\mathcal{H} = -2\sum_{i>j} \mathcal{J}_{ij} \boldsymbol{S}_i \cdot \boldsymbol{S}_j \tag{40}$$

which generalizes the many-electron spins of atoms on lattice sites i, j as $\boldsymbol{S}_i$ and $\boldsymbol{S}_j$.

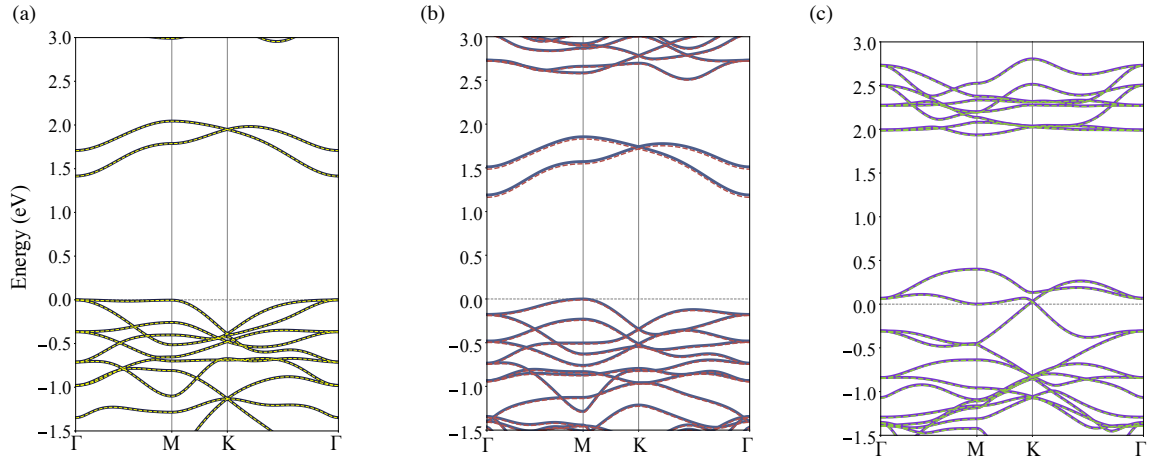

Figure 9. Electronic band structures calculated with the PBEsol+U exchange and correlation functional without SOC for the (a) $OsCl_3$ (b) $OsBr_3$ and (c) OsI_3 case, the dashed lines are the band structures obtained from the Wannier function tight-binding model.

For determining the Curie temperature T_C, the approach taken was to compute the magnetic exchange constants. The electronic states from DFT collinear magnetism calculations (VASP)[82] were mapped to the Wannier function representation (WANNIER90), obtaining the Hamiltonian for the computation of the magnetic interactions between atoms from the rigid spin-rotation perturbation (TB2J) utilizing the Green's function method[83]. The electronic band structures from DFT along with the computed from the

[82] Non-collinear calculations were not employed due to computational restrictions.

[83] X. He et al. 2021.

Wannier Hamiltonian are presented in Fig. 9, where the correct reproduction of the electronic dispersion is evidenced. The values for the magnetic exchange constants are presented in Fig 10, where a positive value in all cases confirmed the ferromagnetic interaction. Additionally, an increasing trend as a function of the atomic number $Z_{Cl,Br,I}$ of the halide is presented. The corresponding Curie temperatures, Eq. (39), obtained were $OsCl_3$:45 K, $OsBr_3$:98 K and OsI_3:390 K. This indicates that the OsI_3 monolayer may be a very good candidate for 2D magnets applications as the Curie temperature is above room temperature. Nevertheless, for a more reliable prediction, the SOC effect should be taken into account, due to its contribution to magnetic anisotropy which may play a role in the stabilization of the magnetic ordering against thermal fluctuations.

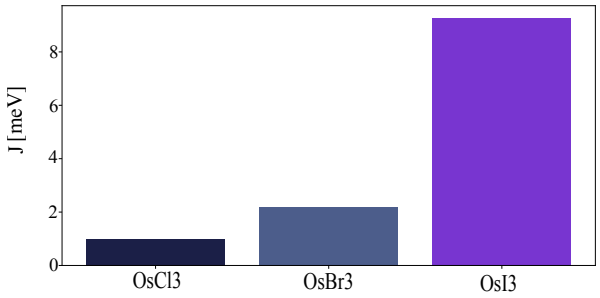

Figure 10. Values for the first magnetic exchange constant for the monolayers.

Finally, the large range magnetic ordering originates from the exchange interactions between the magnetically active atoms in the lattice. This interaction comes from the Coulomb repulsion of nearby electrons along with the Pauli principle of exclusion (as Hund's rules for intra-atomic interactions). Nevertheless, in a real material, there is no unique interaction but multiple competing mechanisms. In transition metals, such as Os, the magnetism comes from localized spins; therefore, the analysis of the exchange interactions presented will be for the case of insulators (supported by the results of section 5.3). For the monolayers is possible to take into account the contri-

bution of two main mechanisms: the direct and super-exchange interactions[84]. In the first case, taking into account the electron orbital occupancy for two Os atoms, each of them posses 5 valence electrons which belong to the t_{2g} as shown in Fig. 7. Therefore, if an electron hops from one atom to another half-filled orbital it will complete the t_{2g} orbitals due to the Pauli principle and will lead to an AFM coupling. This interaction mechanism is related to the wavefunction overlapping, as electrons prefer to delocalize to reduce the system total energy as by the Heisenberg uncertainty principle $\Delta x \Delta p \geq \hbar$, where p and x are the momentum and position respectively. Nevertheless, the results evidencing a ferromagnetic ordering show that this contribution is not the principal one, as the d_{Os-Os} distance in the monolayers is considerable (> 3.48Å). Furthermore, as the distance d_{Os-Os} increases (see Fig. 3) the electronic wavefunction overlapping decreases, and the monolayers tend to a more ferromagnetic behaviour as shown in Fig. 10. For the second case, the super-exchange mechanism involves the virtual transfer of Os electrons mediated by the non-magnetic halide atoms. The magnetic coupling is found by following the Goodenough–Kanamori rules[85]. For the OsX_3 monolayers case, given the symmetry of the lattice and the close to 90^o Os-X-Os angles, as presented in Tab.1, the exchange is ferromagnetic and is considered to be the main contributor. The results presented agree with previous reports on the ferromagnetic ordering presence in $OsCl_3$ and OsI_3[86]. In the latter, the magnetic properties agree qualitatively with the reported in Ref.[87], nevertheless, the crystalline space group differs and is not directly comparable. Lastly, a table summarizing the magnetic properties is presented in Table. 2.

---

[84] Coey 2010; B. G. Li et al. 2020.

[85] Coey 2010.

[86] T. Liu et al. 2019.

[87] B. G. Li et al. 2020.

Material	ΔE meV	Exchange Coupling meV	T_C K
$OsCl_3$	23.99	1.0	44.93
$OsBr_3$	11.92	2.2	97.64
OsI_3	173.55	9.3	390.82

Table 2. Magnetic properties of the OsX_3 monolayers.

5.3. ELECTRONIC PROPERTIES

To shed light on the electronic properties of the ferromagnetic OsX_3 monolayers the self-consistent field calculations from the DFT framework implemented in the VASP package were carried out (see Sec. 7 for computational details). Once obtained the electronic densities, the band structures were computed for the path $\Gamma \rightarrow M \rightarrow K \rightarrow \Gamma$ in the hexagonal Brillouin zone, as shown in Fig. 11. It is worth mentioning that calculations without including SOC employed the collinear magnetism approach and the non-collinear when considering it.

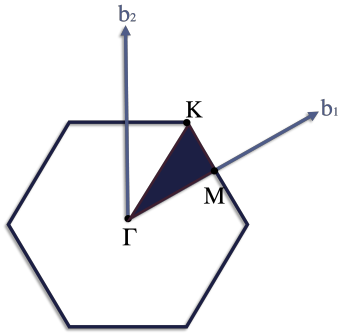

Figure 11. Hexagonal Brillouin zone, the irreducible portion (blue coloured) and the high-symmetry points: Γ, K, M.

The calculated electronic band structures for the three monolayers employing the HSE06 exchange and correlation hybrid functional are presented in Fig. 12. First, the results obtained without SOC for the $OsCl_3$ and $OsBr_3$ cases show a semiconductor/insulator behaviour with a band gap of 1.011 eV and 0.934 eV, respectively.

Moreover, the band features between these two materials are reasonably similar and only defer noticeably on the last occupied band along the $\Gamma \rightarrow M$ path. In the case of OsI_3, there is a metallic behaviour given by the linear dispersion around the Fermi level at the K high symmetry point of the Brillouin zone, by the appearance of a Dirac cone. Additionally, the spin-projected electronic band structures are presented in Fig. 13. Is evident that in all cases there is a 100% spin-polarization around the Fermi level. Due to the ferromagnetic nature of the monolayers, which results in a majority and minority spin channel. In this manner, for the $OsCl_3$ and $OsBr_3$ both spin channels are insulating, but in the OsI_3 case the majority spin channel is metallic while the minority one presents a band gap.

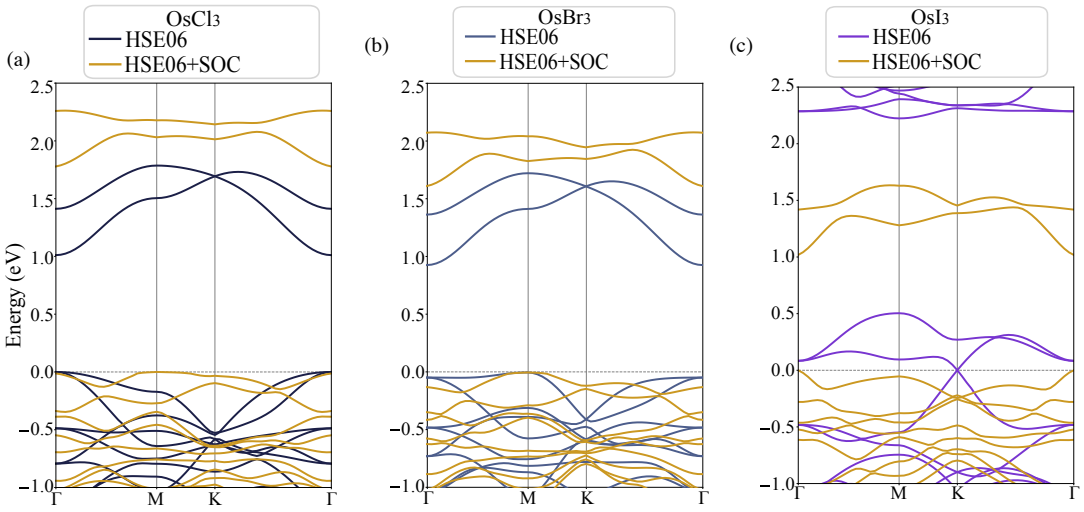

Figure 12. Electronic band structure calculated with the Hybrid exchange and correlation functional HSE06, with SOC (yellow) and without (coloured) for the (a) $OsCl_3$ (b) $OsBr_3$ (c) OsI_3 monolayers.

On the other hand, the electronic band structures taking into account the SOC interaction are presented in Fig. 12 (yellow coloured). As a consequence of the SOC inclusion in all three compounds, there is an insulating behaviour. For the case of $OsCl_3$, the band gap increases to 1.779 eV and for $OsBr_3$ to 1.621 eV. Notably, for the OsI_3 there is a degeneracy lifting at E_F given by a gap opening of 1.018 eV. This

gap opening is intriguing as this characteristic has been suggested as a marker of the QAH topological phase from the theoretical approach[88]. Moreover, the large band gap is beneficial from the practical point of view, as it could be maintained at room temperature. Finally, as a general trend, it can be observed that there is an inverse relation of the electronic band gap with the atomic number $Z_{Cl,Br,I}$ of the halide.

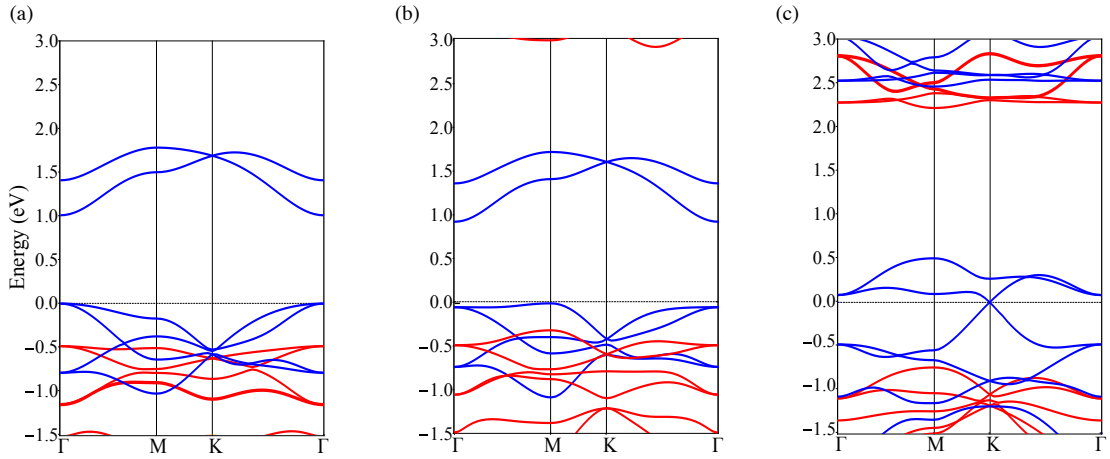

Figure 13. Spin projected electronic band structure without SOC calculated with the Hybrid exchange and correlation functional HSE06 for the (a)$OsCl_3$ (b)$OsBr_3$ and (c)OsI_3 case, blue (spin-majority) channel and red (spin-minority)

To gain deeper insight into the electronic nature of the OsX_3 monolayers, the Bader charge analysis[89] was employed through the software available from the Henkelman Group[90]. The Bader charge is defined as the difference between the number of valence electrons and the total charge computed by the Bader analysis; a non-zero value

[88] Kong et al. 2018; J. He et al. 2017; L. Tian et al. 2019; Jiaxiang Sun et al. 2020; You et al. 2019; Ya ping Wang et al. 2018; e. a. Sun Q. 2019.

[89] Bader 1991.

[90] G. A. Henkelman, Arnaldsson, and Jónsson 2006; Edward Sanville et al. 2007; Yu and Trinkle 2011; Tang, Sanville, and G. Henkelman 2009.

signals the ionicity of the bonding[91]. The Bader charges obtained for the Os atom in the monolayers are presented in Fig. 14. In the case of $OsCl_3$, the Os atom has lost 0.91 electrons, and each Cl atom has attracted 0.31 electrons, indicating an elevated ionic bonding. For the $OsBr_3$ case, the Os atom forfeits 0.43 electrons, and each Br atom gains 0.14 electrons, presenting considerable electronic transport. Finally, for the OsI_3 monolayer, the Os atom yields 0.11 electrons, and the I atom attracts 0.04 electrons. In this manner, from the Bader charge analysis is evident a decrease in the electronic charge transfer as the atomic number $Z_{Cl,Br,I}$ increases, which could be explained by the cell expansion and Os-X distance increment observed in Sec. 5.1.

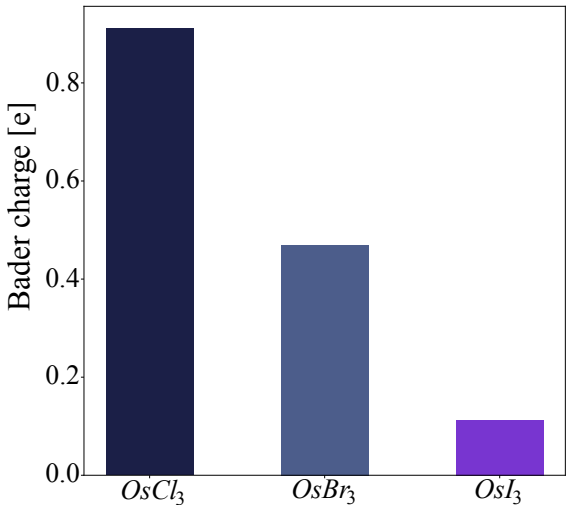

Figure 14. Bader net atomic charges for Os in the OsX_3 monolayers, the non-zero values imply an electronic transfer from Os atoms to the halides.

Another aspect to take into account is the electronegativity difference between the transition metal and the halides. This property gives a measure of the tendency of an atom to attract electrons when forming a bond[92]. For the atoms in question, the

[91] H. Zhang et al. 2018.

[92] Linus 1932.

Pauling electronegativity values are[93]

$$\chi_{Os} = 2.2, \quad \chi_{Cl} = 3.16, \quad t_{Br} = 2.96, \quad \chi_{I} = 2.66,$$

therefore, the differences are

$$\Delta_{Os-Cl} = 0.96, \quad \Delta_{Os-Br} = 0.76, \quad \Delta_{Os-I} = 0.46.$$

This tendency is in accord with the observed reduction in electronic charge transfer. Moreover, in Fig. 15 is presented the electronic band structure of the OsX_3 monolayers projected by atom. Here, the electronegativity difference effect can be evidenced as there is a direct relationship with the band gap size. This band gap trend is supported as well from the spectrochemical series analysis, presented in (38) of Sec. 5.2, as the ligand strength is related to the ligand-field splitting parameter Δ of d orbitals. It can also be observed that the halides (more electronegative) are seen to contribute to the bands below the Fermi energy, in contrast, the Os (less electronegative) are present in the conduction bands. This is supported by the crystal field discussion from Sec. 5.2, where the bonding orbitals (mainly p) are filled before the non-bonding (d orbitals). Additionally, it can be seen that there is a tendency for hybridization to increase around the Fermi level, due to electronic charge retention.

[93] Allred 1961.

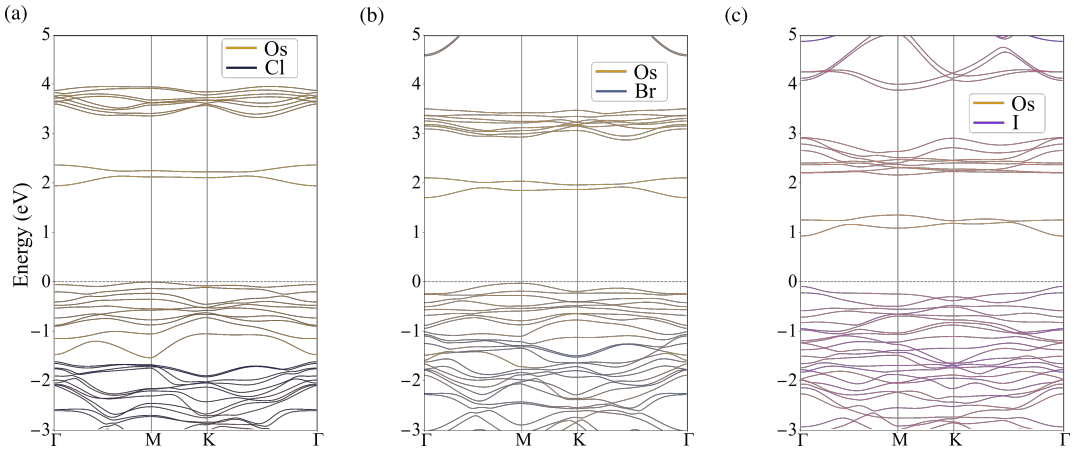

Figure 15. Electronic band structure with SOC calculated with the PBEsol+U exchange and correlation functional taking into account the projection by atom Os (yellow) halide(coloured) for the OsX_3 monolayers.

For the electronic structure description, the Perdew-Burke-Ernzerhof for solids (PBEsol) exchange and correlation functional was initially employed due to presenting lower computational cost. Nevertheless, due to the important electron correlation effect for the transition metal atoms, owing to the localization of their d electrons, the PBEsol functional fails to reproduce accurately the physics of the system. Therefore, the chosen methodology was to make use of the Hubbard[94] correction for the PBEsol case until a good agreement with the HSE06 results; as the later functional is regarded as more precise and closer to the expected experimental results[95]. We found that for the three monolayers, the U=4.0 eV was the appropriate value to correct the electron correlation, as presented in Fig. 16. Here, a good agreement between the band's behaviour around the Fermi level can be evidenced, as well as a difference of 10% ($OsCl_3$), 7% ($OsBr_3$) and 0.7 % (OsI_3) in the electronic band gap.

[94] Dudarev et al. 1998.

[95] Heyd and G. E. Scuseria 2004.

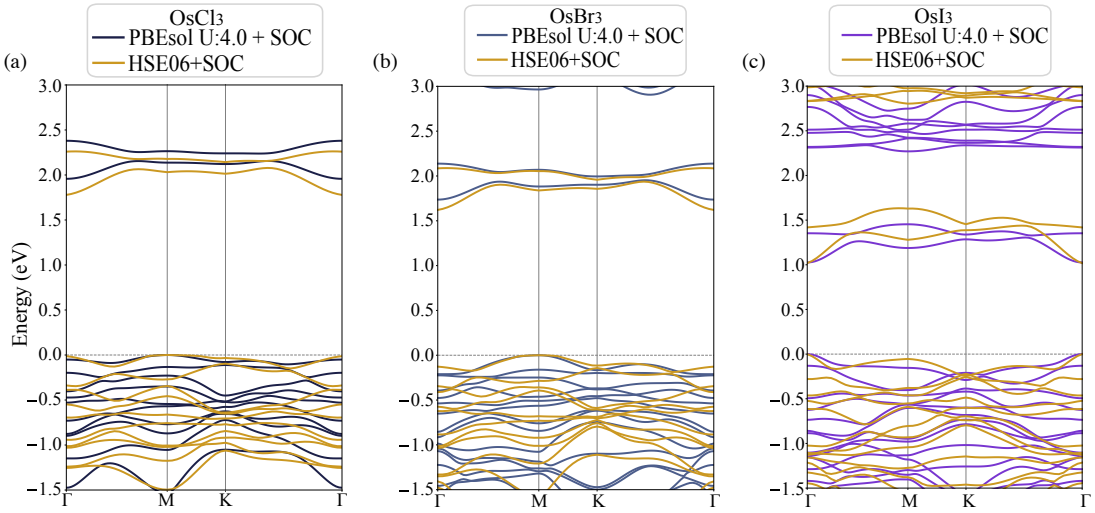

Figure 16. Electronic band structure calculated with the Hybrid HSE06 (yellow) and the PBEsol+U:4.0 (coloured) exchange and correlation functionals, taking into account the SOC for the (a) $OsCl_3$ (b) $OsBr_3$ (c) OsI_3 monolayers.

The description of the electronic structure of these compounds was found to be highly sensitive to the correlation treatment. This can be seen in Fig. 17, in the case of $OsCl_3$, initially without correcting the correlation a band crossing can be observed at the Fermi level between Γ and M; but as U increases it vanishes and there is a gap opening. Henceforth, being fundamentally different in nature from the SOC-induced gap opening. For the $OsCl_3$ case, a small gap was found in the first place, along with a crossing between Γ and M between conduction bands. Once U is taken into account, the crossing disappears and the band gap increases. Finally, the OsI_3 case is notable as the Dirac cone found at the K high symmetry point is preserved under the Hubbard correlation treatment. In view of the above, as there is a change from metallic to insulating behaviour not protected by the crystal potential periodicity, the nature of these compounds is of a Mott insulator. In this type of insulator, the electronic transport behaviour comes from the correlation between electrons[96]. This

[96] Khomskii 2014.

electronic state is characterized by electron localization, and correspondingly there is an appearance of localized spins-magnetic moments as was evidenced in Sec. 5.2.

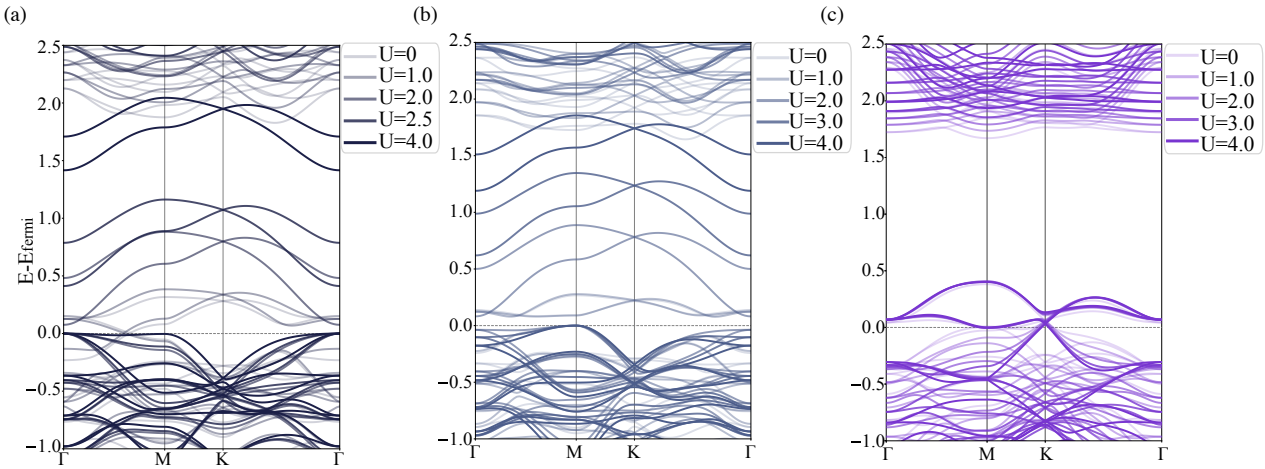

Figure 17. Electronic band structure without SOC calculated with the PBEsol exchange and correlation functional taking into account the Hubbard U correction for the (a) $OsCl_3$ (b) $OsBr_3$ (c) OsI_3 monolayers

Finally, to verify the gap opening of the OsI_3 monolayer as a consequence purely of the SOC inclusion (as the electron correlation was discarded), a non-collinear magnetism calculation without including SOC was performed[97], see Fig. 18. From this result, is evident that the magnetism formalism results in the same electronic band structure, and the crossing remains. The reasons for this difference even though the compounds present a very similar chemical environment (same periodic table group), could be explored from the change in electronic charge transfer shown by the Bader analysis. Moreover, another factor to take into consideration is the SOC effect, which is comparable in magnitude to the crystal field energy Δ_{cf}, and increases for heavier atoms[98]. Finally, another difference of the OsI_3 monolayer is given from the structural

[97] VASP is implemented in such way that calculations including SOC by default imply the utilization of non-collinear magnetism and the spinors formalism.

[98] Khomskii 2014.

point of view, as presented in 4 from Sec. 5.1. The octahedral distortion could also contribute to the difference in the band structure, as the crystal field is modified. This change in angle implies a change in the overlapping of the d orbitals of Os and the p halide orbitals, which could affect the splitting as the antibonding levels are less energetic, and the band gap is reduced.

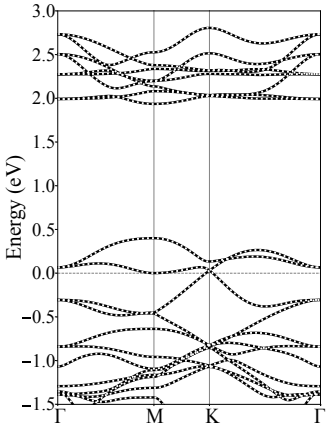

Figure 18. Electronic band structure calculated with the PBEsol exchange and correlation functional for the OsI_3 monolayer, with non-collinear magnetism but not taking into account the SOC.

5.4. SOFTWARE IMPLEMENTATION: CherN

Given the characteristics presented by the OsX_3 monolayers the expected topological phase was the QAH phase, characterized by the total Chern number (C) given by[99]

$$C = \frac{1}{2\pi} \sum_{n}^{\text{occ.}} \int_{\text{BZ}} \mathbf{\Omega}^{(n)}(\mathbf{k}) \cdot d\mathbf{S}. \tag{41}$$

Nevertheless, the Berry curvature $\Omega(\mathbf{k})$ is not directly available in practical density functional theory (DFT)[100] calculations. This constraint prevents straightforward

[99] Thouless 1983; David 2018, chap. 3.2.2.

[100] W. and S. L. J. 1965; H. P. and W. 1964.

computation of Eq. (41). Instead, the tracking of the evolution of hybrid Wannier charge centers (HWCCs) from one boundary in the BZ ($k = 0$) to its periodical image (e.g., $k = 2\pi/a_i$) was proposed to evaluate the Chern number[101]. Available numerical implementations for computing the Chern topological invariant are Z2PACK[102] and WANNIERTOOLS[103]. Z2PACK accepts physical models based on an analytical Hamiltonian, a tight-binding Hamiltonian, or as an input from *ab initio* pseudopotential, plane-wave basis family DFT codes, such as VASP, QUANTUM ESPRESSO, and ABINIT. WANNIERTOOLS, on the other hand, requires construction of a Wannier function tight-binding model based on the results obtained from an *ab initio* code via the WANNIER90 package[104]. To the best of our knowledge, only one numerical implementations for computing the C and $\mathbb{Z}_2$ topological invariants based on the all-electron full-potential DFT code has been reported so far[105]. Nonetheless, the program is not publicly available for use.

In this manner, the implementation of a open-source program that broadens the capability of the all-electron full-potential DFT package WIEN2K[106] to the characterization of topological phases by computing the C invariant was carried out. In addition to computing the topological invariant, this contribution allows us to generate a map of the Berry curvature $\Omega(\mathbf{k})$ in an arbitrary plane of the Brillouin zone, which can be employed for identifying regions with inhomogeneous $\Omega(\mathbf{k})$ values. The latter

---

[101] Soluyanov and Vanderbilt 2011.

[102] Gresch et al. 2017.

[103] Q. Wu et al. 2018.

[104] al. 2020.

[105] Feng, Wen, et al. 2012.

[106] Blaha et al. 2020; B. P. et al. 2018.

functionality complements the growing interest to direct experimental reconstruction of the Berry curvature in reciprocal space, which becomes a target for measuring an underlying topology of Bloch bands[107]. The program employs the programs WIEN2WANNIER[108] and BERRYPI[109] for the calculation of overlap matrix elements and the Berry phase, respectively (both codes are implemented in WIEN2K). This implementation does not require construction of Wannier functions thereby making characterization of topological materials more straightforward.

5.4.1. METHOD

We consider the electronic ground-state for a periodic crystal, which is described by a single-particle mean-field Hamiltonian $H(\mathbf{k})$, a smooth function of the $\mathbf{k}$ crystalline wave vector. The eigenstates of this Hamiltonian are found through the solution of the Kohn-Sham equations given by the DFT[110].

For the calculation of the Chern number as per Eq. (41) it is necessary to perform an integration of the Berry curvature $\Omega(\mathbf{k})$ over the whole 2D BZ. In this context, the BZ is not taken as the Wigner-Seitz cell of the reciprocal space, but a primitive cell consisting of the parallelepiped formed by the reciprocal lattice vectors as in Fig. 19. This integration can be performed by subdividing the 2D BZ ($\mathbf{S}$) into patches ($\mathbf{S}_i$) such that the total Chern number is given by the sum of Berry phases $\gamma^{(n)}_{\partial S_i}$ of occupied states accumulated on the boundary of each patch as originally proposed by[111]. The Berry

---

[107] Mikitik and Sharlai 1999; Y. Liu et al. 2011; M. G. P. and V. 2004; K. F. Mak et al. 2014; Hanzhe Liu et al. 2017.

[108] Kuneš et al. 2010.

[109] Ahmed et al. 2013.

[110] H. P. and W. 1964; W. and S. L. J. 1965.

[111] Fukui, Hatsugai, and Suzuki 2005.

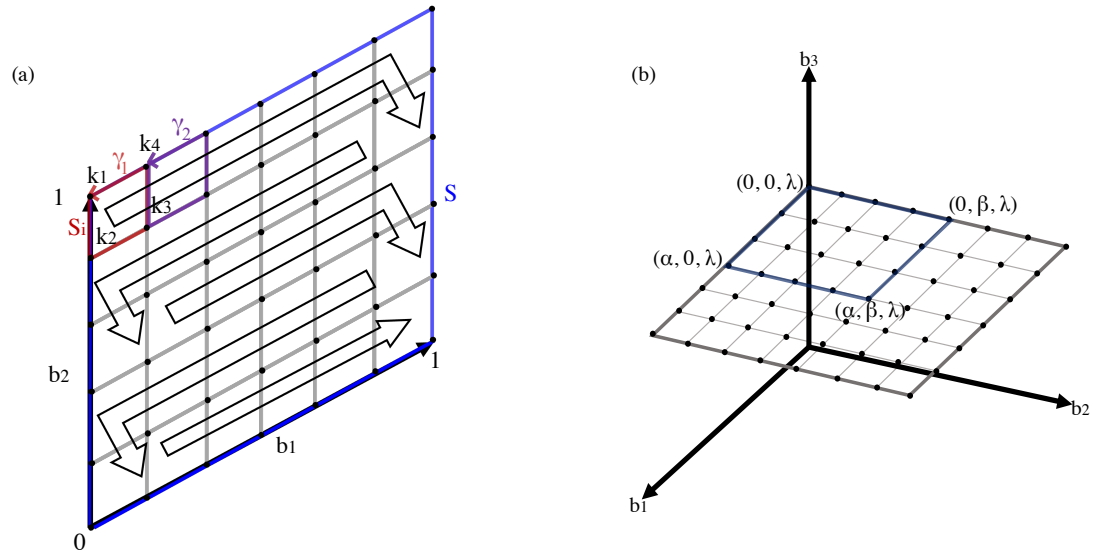

Figure 19. (a) Discretization of the BZ for the calculation of the Chern topological invariant. For each loop S_i the Berry phase is calculated counterclockwise $(k_1, .., k_4, k_1)$ and all the contributions are summed. The phase calculation direction consistency implies that the internal contributions from the loops cancel each other, and the Berry phase for the boundary ∂S is obtained. One of the Berry phase unwrapping schemes (horizontal) for adjacent k point loops is presented. The unwrapping starts from γ_2 with respect to γ_1 and follows the direction of the black arrow (a vertical scheme is also performed and a tolerance requirement is checked for both). (b) Boundary (light blue) discretization of the BZ (light gray) at the selected plane with height λ.

phase is a 2π gauge-invariant quantity which represents a rotation in the complex phase of the cell-periodic part of the Bloch state $|u_{\mathbf{k}}^{(n)}\rangle$ as it traverses adiabatically a closed path over the BZ. It is defined in terms of the Berry potential $\mathcal{A}(\mathbf{k})$ and is related to the Berry curvature via Stoke's theorem as

$$\gamma_{\partial S}^{(n)} = \oint_{\partial S} \mathcal{A}^{(n)}(\mathbf{k}) \cdot d\mathbf{k} = \int_S \Omega^{(n)}(\mathbf{k}) \cdot d\mathbf{S}, \tag{42}$$

where $\mathbf{S}$ is the vector of area normal to the surface, S and ∂S are the surface and its boundary, respectively. The calculation of the Chern number directly from 'raw' $\gamma_{\partial S}$ values is hindered by the gauge uncertainty. For instance, if we were to com-

pute the Berry phase on the whole boundary ∂S of the BZ, it would not be possible to differentiate between the phase of 0 and 2π, or equivalently between the Chern number of 0 and 1. Therefore, an alternative approach involves dividing S into subspaces S_i sufficiently small, so that the obtained change in phase between adjacent loops ∂S_i is smooth enough in comparison to the gauge uncertainty of 2π. Thus, for a patch $\mathbf{S}_i$(Fig. 19a) we can compute the Berry phase $\gamma_{\partial S_i}$ by means of the eigenvalues $\lambda_i = \text{eig}(M)$ of the Wilson loop

$$M = \prod_{i=1}^{J-1} S\left(\mathbf{k}_i, \mathbf{k}_{i+1}\right), \tag{43}$$

which is comprised of discrete k points[112]($\mathbf{k}_1 \equiv \mathbf{k}_J$ due to periodicity of the BZ). Here, $S_{mn}\left(\mathbf{k}_i, \mathbf{k}_j\right)$ are the overlap matrix elements between the cell-periodic term of two eigenstates

$$S_{mn}\left(\mathbf{k}_i, \mathbf{k}_j\right) = \left\langle u_{\mathbf{k}_i}^{(m)} \mid u_{\mathbf{k}_j}^{(n)} \right\rangle \quad m, n \in \left[b_{\text{in}}, b_{\text{fin}}\right], \tag{44}$$

and the eigenvalues of the Wilson loop are related to the total Berry phase by

$$\gamma_{\partial S_i} = \sum_{v}^{\text{occ.}} \arg(\lambda_v) \equiv \Phi_i. \tag{45}$$

This quantity is also referred to as a flux of Berry curvature (or the Berry flux) Φ_i through the patch. For a discrete grid, the magnitude of the Berry curvature projection normal to the plane S_i can be approximated as

$$|\Omega(\mathbf{k})| \approx \frac{\Phi_i}{S_i}. \tag{46}$$

[112] M 2020.

Finally, the Chern number is computed as[113]

$$C = \frac{1}{2\pi} \sum_{i}^{\text{BZ}} \gamma_{\partial S_i}. \tag{47}$$

Since the Chern number is defined as the total flux of Berry curvature in the BZ, Eq. (47) can be viewed as a sum of locally calculated Berry fluxes through each patch; where the i index runs over ∂S_i in such way that the whole surface S is covered. The BZ constitutes a vectorial manifold, for the 2D case a T^2 torus, owing to the periodic boundary conditions of the crystal. Hence, the Chern number can be comprehended as the winding number of the Berry phase around this torus[114].

5.4.2. IMPLEMENTATION

CHERN is a PYTHON script that divides a plane S in the BZ into subsets S_i and evaluates the Berry phase for each boundary ∂S_i following the method described in section 5.4.1 by recursively invoking the main BERRYPI program. The script must be executed in the case directory after performing the standard WIEN2K self-consistent field calculation. For this purpose, the program receives as input: the band's range $[b_{\text{in}}, b_{\text{fin}}]$, the plane normal direction and height, the boundary range $[b_1^{\text{initial}}, b_1^{\text{final}}, b_2^{\text{initial}}, b_2^{\text{final}}]$ (if b_3 is selected as the plane normal direction) and finally, the discretization parameters n_1 and n_2. For example, Fig. 19b presents a scenario for a plane in b_3 direction with height λ and a boundary $[0, \alpha, 0, \beta]$. It is worth noting that for the computation of the Chern number the boundary should cover the BZ, i.e, $[0, 1, 0, 1]$ (or any equivalent selection). Moreover, it is possible to switch the spin-polarized, parallel, and orbital potential (DFT+U) calculation flags. SOC is implied by default.

---

[113] M 2020; Fukui, Hatsugai, and Suzuki 2005; Palyi, Asboth, and Oroszlany 2016; Blanco de Paz et al. 2020.

[114] D. Bercioux et al. 2018.

Sample of `CherN.py` input:

```
bands= [1,70]
n_1 = 10
n_2 = 10
plane_dir = 3
plane_height = 0.0
boundary = [0,1.0,0,1.0]
parallel = False
spinpolar = True
orbital = False
```

The script generates a mesh-grid discretization of $(n_1 - 1) \times (n_2 - 1)$ for the chosen boundary at a plane perpendicular to the selected direction and located at the constant height (see Fig. 19b). Following this, the program generates the appropriate `case.klist` file for each loop ∂S_i in the discretized grid and invokes the BERRYPI code with the specified flags. As the Berry phase calculation inherently carries a 2π uncertainty, two phase unwrapping schemes are utilized (the python `numpy.unwrap` function) for all the calculated phases (see fig 19b) to ensuring a smooth evolution of the Berry flux between adjacent patches. The acceptable criterion for smoothness is $\Delta\gamma < \pi/2$. If the smoothness criterion is not fulfilled, a warning message will be displayed at the end of the run.

Finally, the program calculates the total Chern number C by employing Eq. (47) and stores the result, as well as the Berry curvature projection data (image matrix with values in units of rad bohr^2 separated by comma) obtained from Eq. (46) in the `berrycurv.dat` file. This methodology differs from that chosen in the previously mentioned codes (Z2PACK and WANNIERTOOLS) where the calculation of the polarization is employed, which implies the discretization of the Brillouin zone in a set of strings

along the direction of one of the reciprocal lattice vectors. The two methods are equivalent from the Chern number perspective. In our case, however, the selection of loops also allow us to generate a map of the Berry curvature $\Omega(\mathbf{k})$ (46) as the Berry phase is computed in each loop for the discretized grid. If the MATPLOTLIB library is installed, a Berry curvature map is saved in `.png` and `.pdf` format. The source code of CHERN is available in the BERRYPI GitHub repository[115]. The execution of CHERN requires WIEN2K[116] and BERRYPI[117] (along with its dependencies) installed, as well as the NUMPY library.

5.4.3. VALIDATION

5.4.4. CHERN NUMBER OF $FeBr_3$

2D magnetic materials are profiled as appropriate systems to host the AHC topological phase. The intrinsic magnetic ordering fulfills the time-reversal symmetry-breaking condition and, as a result, conductive edge states are expected to appear in materials with non-trivial Chern numbers. Therefore, we validate our CHERN module by employing it on the $FeBr_3$ monolayer, reported as a hypothetical Chern insulator with a topological invariant value $|C| = 1$[118].

First, for obtaining the $FeBr_3$ monolayer structure we performed the ionic relaxation employing the VASP DFT package[119]. The projector augmented wave pseudopoten-

[115] Oleg 2022.

[116] Blaha et al. 2020.

[117] Ahmed et al. 2013.

[118] Olsen et al. 2019; P. Li 2019; S.-H. Zhang and B.-G. Liu 2017.

[119] G. Kresse and J. Hafner 1993; Kresse and Furthmüller 1996.

tial (PAW) method[120] was utilized with cut-off energy of 500 eV for the plane-wave basis, the valence electrons selected were: Fe(8) and Br(7). The exchange and correlation functional used was the Perdew-Burke-Ernzerhof (PBE)[121] and the Γ-centered Monkhorst-Pack k-mesh grid[122] of $13 \times 13 \times 1$ was selected. Both the cell parameters and internal atomic positions were fully relaxed with a force criterion of less than 1×10^{-2} eV Å^{-1} on all atoms. Additionally, a vacuum of 20 Å was set to avoid interlayer coupling. The obtained structure belongs to the $P\bar{3}1m$ (162) space group and the optimized parameter found was $a = 6.297$ Å in good agreement with Ref.[123].

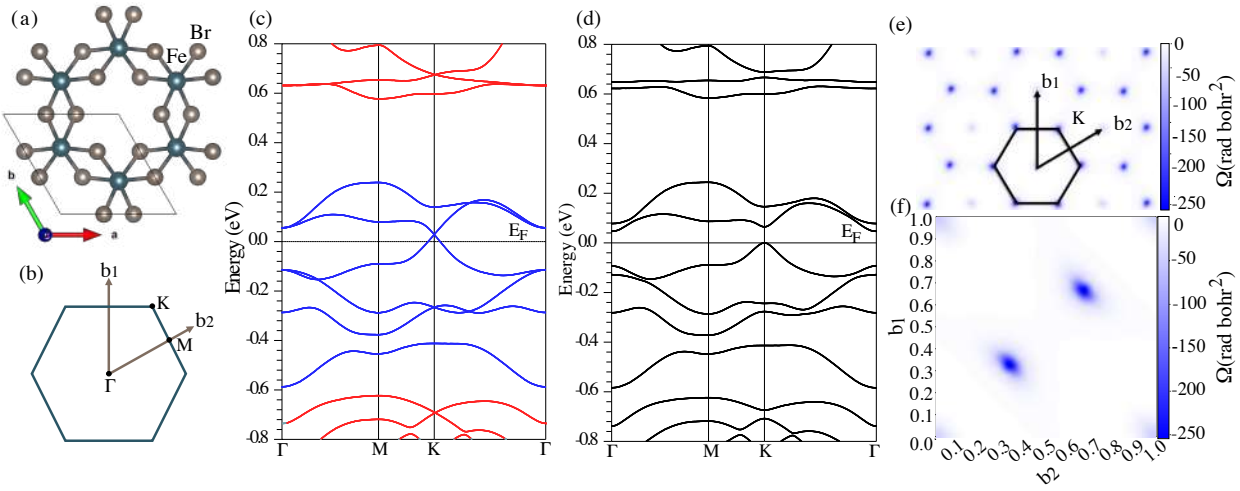

Figure 20. Monolayer $FeBr_3$: (a) crystal structure, (b) BZ and high-symmetry points, (c,d) electronic band structure (spin-up:red, spin-down:blue) without and with SOC, respectively, (e) Berry curvature map in reciprocal space, (f) Berry curvature distribution in the primitive BZ (fractional coordinates).

Taking the obtained structure, the self-consistent field electronic structure calculation

[120] Bloch 1994; G. Kresse and Joubert 1999.

[121] John P. Perdew, Burke, and Ernzerhof 1996.

[122] Monkhorst and Pack 1976.

[123] S.-H. Zhang and B.-G. Liu 2017.

was performed in WIEN2K, within the spin-polarized and second-variational SOC framework, a parameter $\min(R_{\text{MT}})K_{\text{max}} = 7$, and a k-point mesh grid of $15 \times 15 \times 1$ were taken. Here K_{max} is the largest reciprocal-lattice vector size (plane wave cut-off) and R_{MT}= 2.26, 2.15 bohr for Fe and Br, respectively, which refers to the smallest of all atomic sphere radii. The energy cut-off separating the core from valence states was such that 14 and 17 electrons were considered as valence for Fe and Br, respectively. The calculation was initialized with a magnetic moment value of $1\mu_B$ per formula unit, with Fe as the magnetically active atom, and the ground state found was ferromagnetic with a magnetic moment of $0.99\mu_B$ per formula unit, henceforth, breaking the time-reversal symmetry of the system. Figure 20a,b shows the $FeBr_3$ monolayer structure and the BZ, respectively. In Fig. 20c the electronic band structure without SOC is presented, where a crossing at the Fermi level (between bands 130 and 131) can be observed at the K high-symmetry point. A SOC-induced gap opening of 47 meV can be evidenced in Fig. 20d, which lifts the degeneracy at E_{F} and indicates the Chern insulator phase[124].

The projected Berry curvature map for $FeBr_3$ is presented in Fig. 20e along with the detailed map in the primitive BZ (fractional coordinates) shown in Fig. 20f. It can be observed that the source of Berry curvature comes from the high symmetry point K where the SOC gap emerged. The calculation was performed with the spin polar and parallel flags, the range of occupied bands [1,130] was selected, and the discretization parameters $n_1 = n_2 = 33$ were used. It should be noted that for obtaining reliable results this parameters must be increased until the tolerance criteria is achieved, in this case for values higher than $n_1 = n_2 = 21$. Moreover, the lattice vector perpendicular to the monolayer ($\mathbf{a}_3$) was selected as the `plane_dir` parameter, and the plane height was set to 0. The obtained Chern number given by Eq. (47) is $|C| = 1$, which

[124] Olsen et al. 2019; P. Li 2019; S.-H. Zhang and B.-G. Liu 2017.

agrees with prior theoretical studies[125].

5.4.5. BERRY CURVATURE OF MoS_2

For the validation of the Berry curvature maps, the MoS_2 monolayer was selected due to its characteristic behaviour, the opposite Berry curvature at the corners of the hexagonal Brillouin zone (K and K' high symmetry points as in Fig. 21b) Feng, Yao, et al. 2012; Xiao et al. 2012. For this reason this material has attracted great attention due to the potential uses in electronics and emerging fields such as valleytronics and spintronics Xiao et al. 2012; Lembke, Bertolazzi, and Kis 2015; Zhongying Wang and B. Mi 2017; H. Li et al. 2014. Nevertheless, as this is a non-magnetic monolayer the TRS breaking condition is not met, and it cannot be a Chern Insulator ($C = 0$).

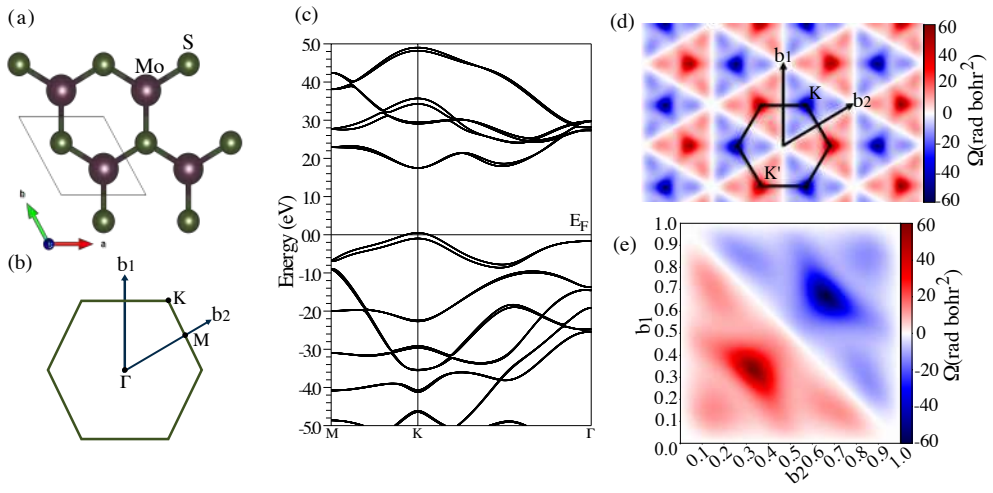

Figure 21. Monolayer MoS_2: (a) crystal structure, (b) BZ, (c) calculated electronic band structure with SOC, (d) Berry curvature map in reciprocal space, (e) Berry curvature distribution in the primitive BZ (fractional coordinates).

The self-consistent field calculations were carried out with the full-potential linearized augmented plane-wave DFT method implemented in WIEN2K. The experimental

[125] Olsen et al. 2019; P. Li 2019; S.-H. Zhang and B.-G. Liu 2017.

data from Ref.[126] were utilized for the crystal structure, fixing the lattice parameter of the monolayer to $a_1 = 3.16$ Å, which belongs to the $P\bar{6}m2$ (187) space group, as presented in Fig. 21a. To avoid interlayer coupling, a vacuum of $a_3 = 9.11$ Å was employed, which corresponds to the triple value of interlayer bulk distance. The PBE generalized gradient approximation[127] was selected for the exchange and correlation functional. For the electronic ground states the parameter $\min(R_{\text{MT}})K_{\text{max}} = 7$ was utilized (muffin tin radii $R_{\text{MT}} = 2.44, 2.10$ bohr for Mo and S, respectively) with a k-mesh grid of $16 \times 16 \times 3$. The energy cut-off separating the core from valence states was such that 14 and 6 electrons were considered as valence for Mo and S, respectively; the charge leakage was checked. The spin-orbit coupling was taken into account.

The calculated ground state was found to be nonmagnetic (resulting in $|C| = 0$), and the electronic band structure is presented in Fig. 21c. Here it can be seen that monolayer MoS_2 is a semiconductor with a direct band gap of 1.8 eV[128]. For calculation of the Berry curvature map, the k-parallel flag was employed, the selected range of occupied bands was $[1, 26]$, the selected `plane_dir` parameter corresponded to the lattice vector perpendicular to the monolayer (i.e., $\mathbf{a}_3$), and the plane height was set to 0. The discretization parameters $n_1 = n_2 = 51$ were selected, while the continuity of Berry curvature was achieved starting from $n_1 = n_2 = 32$. The inherent inversion symmetry breaking due to the monolayer configuration combined with the strong SOC result in appearance of opposite sign contributions to the Berry curvature with peaks at the K and K' high symmetry k-points. Moreover, $\Omega(\mathbf{k})$ vanishes at the Γ and M high symmetry points. These features of the Berry curvature map are in good

[126] Villars and Cenzual n.d.

[127] John P. Perdew, Burke, and Ernzerhof 1996.

[128] Xiao et al. 2012.

agreement with prior theoretical studies by Ref.[129].

5.5. TOPOLOGICAL PROPERTIES

To study the topological properties, particularly, determining the Chern topological invariant of the OsX_3 monolayers, two methodologies were employed: the utilization of the CHERN module discussed in Sec. 5.4 and the use of the Z2PACK[130] software. For the CHERN case, as it is available for the WIEN2K DFT package, the relaxed crystal structures calculated from VASP were employed and the self-consistent field calculations were carried out. The correct reproduction of the results was verified through the comparison of the obtained electronic band structures, see Appendix. 8.6, and the computational details for the WIEN2K package are provided in Sec. 7. In the Z2PACK case, there are two input options available for the Chern number calculation: a tight-binding Hamiltonian and interfacing from ab initio codes such as VASP. Both approaches were explored, the first by the construction of the MLWF through the WANNIER90 code. Nevertheless, the results obtained in this case were too sensitive, as different Chern numbers were obtained for the same compound by a variation of the convergence parameters provided by Z2PACK. Therefore, the results presented from this software are obtained by interfacing with the VASP code, utilizing the calculated electronic charge densities from Sec. 5.3.

---

[129] Feng, Yao, et al. 2012.

[130] Dominik et al. 2017.

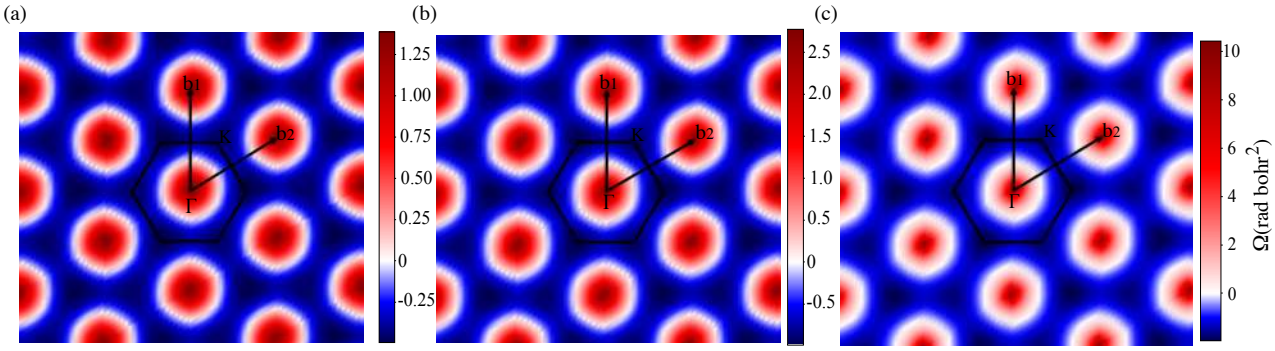

Figure 22. Berry curvature map in reciprocal space with U=4.0 eV for (a) $OsCl_3$ (b) $OsBr_3$ and (c) OsI_3.

The CHERN calculations were performed with the spin polar, parallel and orbital flags. The lattice vector perpendicular to the monolayer ($\mathbf{a}_3$) was selected as the `plane_dir` parameter, and the plane height was set to 0. The discretization parameters employed for the three monolayers were $n_1 = n_2 = 21$, which achieved the convergence tolerance. The band ranges taken were the set of occupied bands: $OsCl_3$ [1,98], $OsBr_3$ [1,158] and OsI_3 [1,158]. The computed Chern numbers for the three cases were $|C| = 0$ and the Berry curvature maps obtained are presented in Fig. 22. In all cases a non-null Berry curvature Ω can be observed in reciprocal space, where the positive contribution originates mainly from the Γ high symmetry point; decaying as you move away from Γ to negative values in the M and minimums in the K high symmetry points. Moreover, as the atomic number $Z_{Cl,Br,I}$ of the halide increases a trend can be observed such that there is an increment of Berry curvature values, in conjunction with a sharper behaviour around the Γ and K points in reciprocal space.

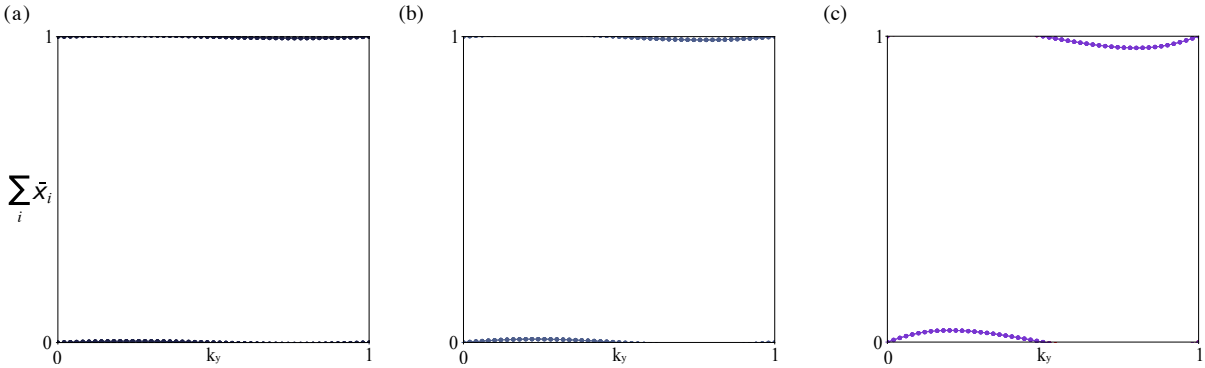

Figure 23. Tracking of the HWCC for the occupied states with U=4 eV for (a) $OsCl_3$ (b) $OsBr_3$ and (c) OsI_3.

In the Z2PACK case, the obtained results support the previous findings, as the calculated Chern number in all OsX_3 compounds is $|C| = 0$. This can be observed in Fig. 23, where the summation of the hybrid Wannier charge centers as a function of k_y is presented. In this manner, as this quantity is proportional to the Berry phase, $\gamma = \frac{2\pi}{a} \sum_n \bar{x}_n$, where a is the lattice parameter, and taking into account the interpretation of the Chern number (see Sec.5.4.2) as the winding of the number of the Berry phase along the Brillouin zone, the behaviour is consistent with a null-winding and a trivial Chern topological invariant.

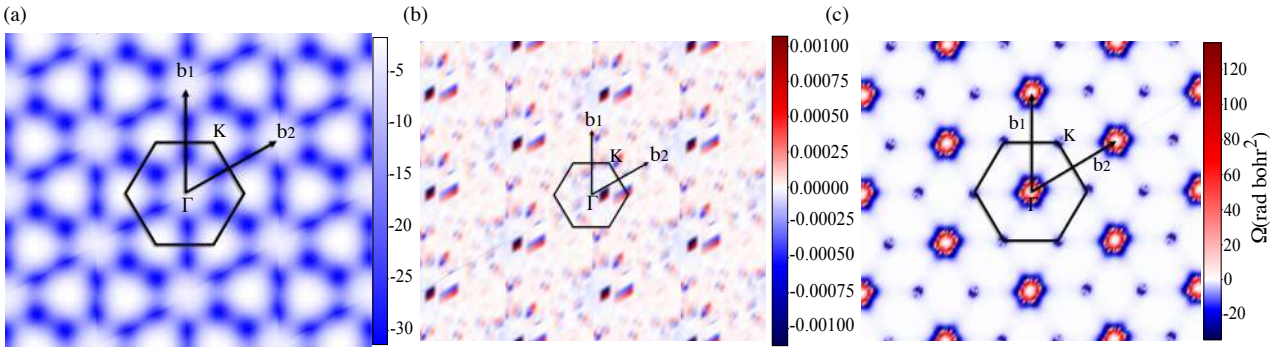

Figure 24. Berry curvature map in reciprocal space with U=0 eV for (a) $OsCl_3$ (b) $OsBr_3$ and (c) OsI_3.

Moreover, the calculations for the $U = 0$ case were carried out, motivated by previous

reports of the topological features of the $OsCl_3$ and OsI_3 monolayer[131], both predicting a non-null Chern number in them without taking into account the Hubbard U correlation correction and from the PBE exchange and correlation treatment[132]. The CHERN calculations were performed without the orbital flag as $U = 0$, and the same plane direction and value as those taken in the last section. The discretization parameters employed were $n_1 = n_2 = 21, 31, 33$; for the $OsCl_3$, $OsBr_3$ and OsI_3, respectively, and the band ranges taken were the occupied bands. The calculated Chern numbers were $|C| = 0$ for the $OsBr_3$ and OsI_3 cases and $|C| = 2$ for $OsCl_3$, consistent through the employment of both the PBE and PBEsol functionals. In Fig. 24 are presented the Berry curvature maps. Here, for the $OsBr_3$ case, Ω is found to be negligible over reciprocal space. For the OsI_3, there is significant Berry curvature presence in the BZ. The behaviour is such that there is both a positive and negative contribution around the Γ high symmetry point and a localized negative contribution at the K point, similarly to the $FeBr_3$ case of Sec. 5.4.3. Finally, in the $OsCl_3$ case, the Berry curvature presence has entirely the same sign, therefore, the integration over the Brillouin zone is not-null, as given by the calculated Chern number. In this case, it originates mainly from the region between the Γ and M high symmetry points; where the band crossing was observed in Fig. 17. Nevertheless, as discussed in Sec. 5.3, this degeneracy is lifted purely from the correlation correction, and as a result is not observed in Fig. 22.

In view of the foregoing, it can be evidenced that the theoretical study of topological features is a complex phenomenon that presents great susceptibility to the electronic structure description, particularly, the correlation treatment[133]. This is a natural con-

[131] Sheng and Nikolić 2017; Fang et al. 2022.

[132] The results presented here were using the PBEsol functional both in VASP and WIEN2K.

[133] Olsen et al. 2019.

sequence, as the change in the electronic interaction description results in a modification in the crystal wave functions and therefore an alteration in the band structure; from which topology the Berry curvature Ω is obtained. Based on the magnetic 5.2 and electronic 5.3 results from the OsX_3 monolayers the expected candidate for the Chern Insulator phase was the OsI_3 as it presented a strong ferromagnetic ordering, breaking the TRS, and a SOC-induced gap opening of the band crossing. Nevertheless, the computation of the Chern topological invariant indicates a trivial topology. Improvements in the methodology taken could be avoiding the transition from VASP to WIEN2K, by an implementation of the CHERN program in the former. Additionally, the possibility of calculating the Berry curvature for the HSE06 case could be optimal, nonetheless, due to computational restrictions is not yet an available option.

Section 6.0

CONCLUSIONS

From the presented developments and results from the DFT *ab initio* calculations of this work, is possible to state the following conclusions:

1. It was possible to find the relaxed crystal structures of the OsX_3 (X: Cl, Br, I) monolayer family, finding that they belong to the $P\bar{3}1m(162)$ space group. Employing the simulation package it was possible to determine the structural properties, such as the lattice constants, widths of the monolayer and the distances and angles between the atoms in the structures. An expansion trend of the monolayers and Os-Os distance was observed as a function of the halide atomic number. Finally, the monolayer condensed phase formation was energetically favourable as the cohesive energy E_c in all cases was negative, and a tendency related to the ionicity loss could be evidenced.

2. For all the OsX_3 (X: Cl, Br, I) monolayer family it was found a ferromagnetic ordering is the ground state of the system. It was possible to determine the spin and orbital magnetic moment, corresponding to the low spin configuration for the octahedral field splitting for the crystalline environment. The Hubbard correction was probed to be crucial for determining the magnetic properties of the PBEsol calculations. Additionally, large orbital magnetic moments were encountered, originating from the elevated SOC effect and the electron occupancy configuration. Moreover, the origin of the crystal field splitting was analyzed, such as the minimization or electron repulsion and the covalency contribution. The latter is expected to be not as significant because even though the high Z Os atom is present, the halide atoms (Cl, Br, I) are weak ligands given by the spectrochemical series. It was possible to carry out an estimation of the criti-

cal temperature T_C for the ferromagnetic ordering of the monolayers through the computation of the magnetic exchange constants. The OsI_3 monolayer was considered the most suitable candidate, due to the above room temperature calculated value. Lastly, the interaction mechanisms between magnetically active atoms in the lattice were reviewed. From this analysis, in conjunction with the structural features, the super-exchange interaction was considered the main contributor, benefiting FM behaviour.

3. The electronic band structure was determined from the HSE06 level, finding the monolayers as Mott insulators. Through SOC inclusion in the calculations, it was possible to observe a degeneracy lifting for the Dirac cone presented in the OsI_3 monolayer. Moreover, the electronic band structures projected by spin and atom contribution were examined. The former evidenced a 100% spin polarization around the Fermi level; and the latter, on the other hand, was discussed from the electronegativity difference and electronic charge transfer. In this manner, the basis taken to study the bonding behaviour was employing the Bader charge analysis. This technique allowed us to determine a decrease in the charge transfer between the Os atom and the corresponding halides as the atomic number increased $Z_{Cl,Br,I}$, losing ionicity. Additionally, the appropriate Hubbard U value for calculations employing the PBEsol functional was found to be U=4.0 eV, determined by a fitting to the HSE06 results. In addition, the great susceptibility of the electronic structure of the monolayers to the correlation effect was assessed, encountering a degeneracy lifting by the correlation correction for the $OsCl_3$ case. The OsI_3 monolayer band-crossing proved robust to these changes, and the gap opening was demonstrated to be purely from the SOC effect. Finally, the possible causes for this difference were discussed, such as the electronic transfer behaviour, the elevated SOC and the octahedral distortion.

4. We introduced the CHERN software module for computing the Chern topological invariant implemented in the all-electron full-potential package WIEN2K. The method of characterization was presented and relies on computing the Berry phase for a multitude of Wilson loops that discretize a 2D Brillouin zone. Additionally, the program implementation was described. Validation of the program was confirmed by testing on the well-known materials with topological features: monolayer $FeBr_3$ as a Chern insulator and monolayer MoS_2 with a distinct Berry curvature map. The results agree with the available experimental and computational data. The analysis of topological characteristics can be performed directly after performing a self-consistent field calculation without constructing maximally localized Wannier functions. This feature makes these computational tools attractive for the study and prediction of topological materials.

5. The topological features of the monolayers were explored from the implemented CHERN program and the available software for computing topological invariants. The Berry curvature maps and Chern numbers were computed for both Hubbard-corrected and not corrected cases. With this, the Berry curvature presence on reciprocal space was reviewed. The study of the topological features was found to be non-trivial as a careful description of the electronic correlation is needed. Therefore, even though the OsI_3 monolayer presented itself as a possible candidate to present the Chern insulator topological phase, once taking into account the U parameter the result was a null Chern number, as well as a similar Berry curvature distribution as the other monolayers. These results were corroborated by the zero Chern number found employing the Z2PACK program.

6. We expect that the study of these new systems might awaken the interest and future efforts to the experimental synthesizing and magnetic probing of the OsX_3 monolayers. Likewise, the properties presented by the materials could position

them as building blocks for devices in emerging fields, such as spintronics and hetero-structures.

Section 7.0

COMPUTATIONAL DETAILS

The density functional theory (DFT)[134] framework calculations were performed on the software implementations: VASP[135] and WIEN2K[136]. For the topological characterization: In the case of the VASP results the Z2PACK[137] software was utilized and for the WIEN2K case the program used was the CHERN module, part of the BERRYPI[138] software. Additionaly, for the exchange constants calculations the WANNIER90 software was employed for constructing the Wannier function tight binding model[139].

7.1. VASP

For reproducing the interaction between the ion + core electron system with the valence electrons, the projector augmented wave pseudopotential (PAW) method was utilized with cut-off energy of 600 eV for the plane-wave expansion[140]. The valence electrons selected were: $5p^6 6s^2 5d^6$ (Os) and s^2p^5 (Cl,Br,I). Concerning the exchange and correlation treatment, the selected functionals were the generalized gradient approximation (GGA) and Hybrid calculations with the Perdew-Burke-Ernzerhof for

---

[134] Hohenberg and Kohn 1964; Kohn and Sham 1965.

[135] G. and H. J. 1993; G. Kresse and J. Furthmüller 1996; G. Kresse and Furthmuller 1996.

[136] Peter et al. 2020.

[137] Dominik et al. 2017.

[138] Rubel 2022.

[139] Pizzi et al. 2020.

[140] G. and D. 1999; Kresse and Hafner 1994.

solids (PBEsol) and Heyd-Scuseria-Ernzerhof (HSE06) respectively. The Brillouin zones were sampled with a $9 \times 9 \times 1$ Γ-centered Monkhorst-Pack mesh grid. For the self-consistent field calculations the convergence tolerance selected was 1×10^{-8} eV and for the ionic optimization, the force criterion was 1×10^{-4} eVÅ^{-1}. Moreover, due to the significant correlation effects due to the highly localized d electrons of Os, the Hubbard correction[141] was taken into account with a U = 4 eV value for all compounds. Moreover, for the orbital occupancy around Fermi smoothing Gaussian smearing with 0.02 eV was selected. Finally, as the studied systems were monolayers to avoid inter-layer interaction a vacuum greater than 15 Å was set between them for all the structures. The cut-off energy and k-points mesh grid selection was taken based on the convergence tests performed for the $OsBr_3$ monolayer presented in Fig.25, the selection made took into account finding the best values for equilibrium between accuracy and computational cost. Finally, for the Bader charge calculations, the NG(X,Y,Z)F grid employed was $128 \times 128 \times 64$ which is two times finer than the employed in the self consistent field calculations.

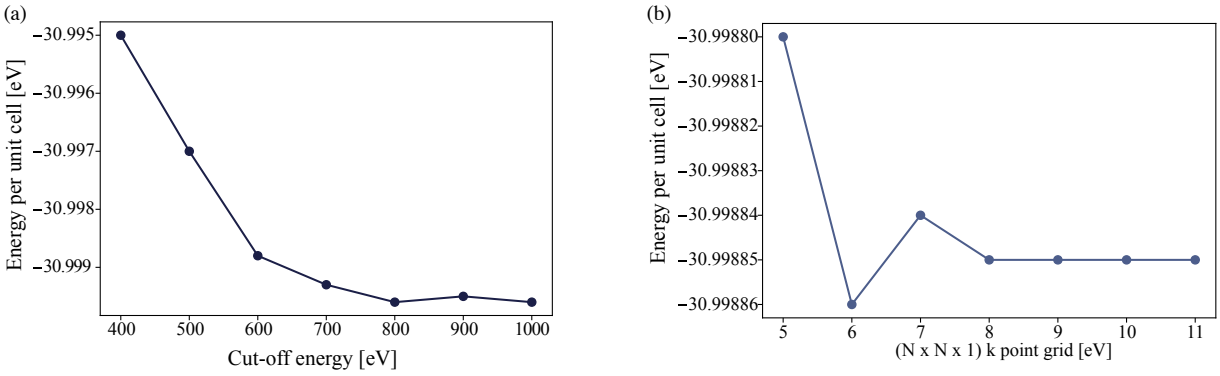

Figure 25. Convergence tests for (a) cut-off energy for the plane wave expansion (b) k-points meshgrid.

[141] Dudarev et al. 1998.

7.2. WIEN2K

For the exchange and correlation treatment, the Perdew-Burke-Ernzerhof for solids (PBEsol) GGA functional was selected. A reduction of 3% muffin-tin radii R_{MT}, the product $min(R_{MT})K_{max} = 8$, the separation energy of -6.0 Ry and a 15 $\times$ 15 $\times$ 1 k-point mesh-grid. For the self-consistent field calculation the energy convergence of $10^{-6}Ry$, and charge convergence of 10^{-3} e. For the Hubbard correction, a U = 0.367 Ry was selected. Finally, a Fermi temperature smearing was taken for the orbital occupancy with a broadening parameter of 0.0015 Ry. For the $OsCl_3$ case the R_{MT} values selected were 2.37,1.94 bohr for Os and Cl, respectively; and the number of valence electrons were 28 and 7 for Os and Cl, respectively. For the $OsBr_3$ the R_{MT} values employed were 2.40,2.17 bohr, for Os and Br, respectively; and the number of valence electrons were 28 and 17 for Os and Br, respectively. Finally, for the OsI_3 case the R_{MT} values used were 2.49,2.37 bohr, for Os and I, respectively; and the number of valence electrons were 28 and 17, for Os and I, respectively.

7.3. CHERN

For the Chern number and Berry flux calculations, the discretization parameter n selected was such that the continuity criteria for the phase unwrapping were verified, for all the cases $n > 21$. For the band selection, the occupied set of bands for each case was selected. The selected plane was the k_{xy} plane with a $k_z = 0$ value and a full Brillouin zone boundary selection. Finally, the calculations were performed with the spin-polarized option and additional orbital potential (for the U-corrected cases).

7.4. Z2PACK

For the Chern number calculation, the selected method was through the linkage with VASP. The surface selected was at $k_z = 0$ and the Wannier charge centers were calcu-

lated on lines along the k_y direction. The tolerance for the change in Wannier charge centers positions selected was $pos\_tol = 0.01$, the iterator along lines selected was $iterator = range(8, 50, 2)$, the tolerance for the distance between the largest gap and neighbouring WCC used was $gap\_tol = 0.3$, the minimum distance between neighbouring lines selected was $min\_neighbour\_dist = 0.001$ and the initial number of lines utilized was $num\_lines = 51$.

7.5. WANNIER90

For the DFT crystal electronic states mapping to the Wannier function representation the methodology employed was to find the maximally localized Wannier functions. For the disentanglement process, the limit of the frozen window was taken as 4 eV over the Fermi energy E_F, and with a tolerance of 10^{-6} for the fractional change of Ω_I. In the case of the wannierization the convergence tolerance of 10^{-9} for Ω was used. Finally, the projection was taken for the s, p, d electrons in the Os case and s, p for the halide atoms (Cl, Br, I).

Section 8.0

APPENDICES

8.1. APPENDIX A: PHYSICAL APPROXIMATIONS

To find solutions to Eq. (8) is necessary to make some approximations of physical character, that is, the assumption of behaviours of the system or form in the solutions; to simplify the equation to be solved without losing accuracy. The first of these approximations have the purpose of both specifying the behaviour of the ions and decoupling the electronic system from the ionic one; it is the *Born-Oppenheimer* or adiabatic approximation. Based on the fact that the mass of the ions M_I is much larger than the mass of the electrons m_i, the electronic system always 'perceives' the static ions and their effect as an effective potential. Thus, if the lattice ions move, the electrons evolve from energy ground-states based on the initial ionic positions to energy ground-states based on the final positions. In other words, they immediately adjust to the new configuration through minimum energy states. From the perspective of the ionic system, the electrons move at high speed, and the effect on the ions is to 'perceive' them as a homogeneous electric charge density that generates an effective potential. Additionally, once the ionic system decouples, based on the fact that the mass of the ions is considerable they can be treated as classical particles.[142] Then, to determine the equilibrium positions of the ionic system is only necessary to know the types of atoms in the lattice and the electron density and calculate the forces on the ions to perform the minimization process of the potential energy surface.

The result of this approximation in the equation Eq. (8), is that the kinetic energy

[142] An approximation that works well for the study of the equilibrium structure of materials as long as the atoms are not very light.

term of the ions tends to zero and the repulsive potential between them is a constant energy, i.e., the Madelung energy. Therefore, the ionic coordinates are transformed into parameters and the dependence of the wave function is only on the electronic positions: $\Psi(\mathbf{r_i})$. This makes physical sense since in a solid the nuclei do not travel long distances, but remain in fixed positions. Then the equation to be solved is

$$\left[\sum_i \frac{-\hbar^2}{2m}\nabla_i^2 - V_n(r) + \frac{1}{2}\sum_{i\neq j}\frac{e^2}{|\mathrm{r}_i - \mathbf{r}_j|}\right]\Psi = E\Psi, \tag{48}$$

with

$$E = E_{\mathrm{tot}} - \frac{e^2}{2}\sum_{I\neq J}\frac{Z_I Z_J}{|\mathbf{R}_I - \mathbf{R}_J|}, \tag{49}$$

and

$$V_{\mathrm{n}}(\mathrm{r}) = -\sum_I \frac{e^2 Z_I}{|\mathrm{r} - \mathrm{R}_I|}. \tag{50}$$

On the other hand, the single-particle approximation is performed, which consists of assuming a solution of the many-body wave function $\Psi(\mathbf{r_1}, \mathbf{r_2}, ...)$ as a function composed of the ϕ_i wave functions obtained by solving the Schrödinger equation for one electron only. This represents a great simplification since it goes from the problem of solving the 3N-dimensional Schrödinger equation to solving N three-dimensional equations.

$$\left[-\frac{\hbar^2}{2m}\nabla^2 + V_{\mathrm{n}}(\mathbf{r}) + V_{\mathrm{H}}(\mathbf{r})\right]\phi_i(\mathbf{r}) = \varepsilon_i\phi_i(\mathbf{r}), \tag{51}$$

here, this approximation implies assuming a system of independent electrons. But, for which it is possible to incorporate the effect of repulsion between electrons through the mean-field approximation, in which the effective potential V_H, known as the Hartree potential, is found, given by the expression

$$V_{\mathrm{H}}(\mathbf{r}) = e^2\int d\mathbf{r}'\frac{n\left(\mathbf{r}'\right)}{|\mathbf{r} - \mathbf{r}'|}. \tag{52}$$

So, from the solutions obtained for Eq. (51), it is possible to construct a wave function $\Psi(\mathbf{r_1}, \mathbf{r_2}, ...)$ that satisfies the conditions required to represent a quantum mechanical system; that is, it must be normalized ($\langle \Psi \mid \Psi \rangle = 1$) and it must be antisymmetric under two-electron exchange, as indicated by the Pauli exclusion principle. Thus, observables such as the energy of the system can be calculated as

$$E = \langle \Psi | \hat{H} | \Psi \rangle = \int d\mathbf{r}_1 \dots d\mathbf{r}_N \Psi^* \left(\mathbf{r}_1, \dots, \mathbf{r}_N \right) \hat{H} \Psi \left(\mathbf{r}_1, \dots, \mathbf{r}_N \right), \tag{53}$$

with

$$\hat{H} = \hat{T} + V_n + \hat{W} = -\sum_i \frac{\hbar^2}{2m} \nabla_i^2 + \sum_i V_{\mathrm{n}} \left(\mathrm{r}_i \right) + \frac{1}{2} \sum_{i \neq j} \frac{1}{|\mathrm{r}_i - \mathrm{r}_j|}, \tag{54}$$

and the electron density as

$$n(\mathbf{r}) = \sum_i |\phi_i(\mathbf{r})|^2 . \tag{55}$$

8.2. APPENDIX B: SPIN ORBIT COUPLING (SOC)

The spin-orbit coupling is a physical phenomenon of relativistic origin, which modifies the energetic states of the atom and, consequently, the electronic structure obtained for a material[143]. Moreover, this is the main contributor to crystalline magnetoanisotropy, which can be understood from the effect that this has in lifting the degeneracy of the energy states in the atom, the orbitals, which generally have a directional character. Spin-orbit coupling arises from the interaction between the orbital angular momentum of the electron and its intrinsic angular momentum: the spin.

In addition to the analysis presented here, it is possible to derive the same result from the Dirac equation in the non-relativistic limit of this interaction to estimate the energy contribution as follows:

Initially, considering a hydrogen-like atom, in which, from the electron frame of reference, the nucleus is orbiting around the electron at a velocity v; thus, a current is generated and gives rise to a magnetic field

$$\mathbf{B} = \frac{\mathbf{v} \times \mathbf{E}}{c^2}, \tag{56}$$

where

$$\mathbf{E} = -\nabla V(r) = -\frac{\mathbf{r}}{r}\frac{\mathrm{d}V(r)}{\mathrm{d}r}, \tag{57}$$

is the electric field corresponding to the electron due to the nucleus and $V(r) = -r\phi(\mathbf{r})$ the corresponding potential energy. It is necessary to mention the origin of Eq. (56) from relativistic electromagnetic theory[144]. It represents the magnetic field

[143] Vanderbilt 2018; Blundell 2001; Giustino 2014; Coey 2010.

[144] Griffiths 2013.

experienced by the electron, produced by the nucleus due to the relative motion between them; which interacts with the electron spin giving rise to a term in the Hamiltonian

$$H_{\mathrm{so}} = -\frac{1}{2}\mathbf{m}\cdot\mathbf{B} = \frac{e\hbar^2}{2m_{\mathrm{e}}c^2 r}\frac{\mathrm{d}V(r)}{\mathrm{d}r}\mathbf{S}\cdot\mathbf{L}, \tag{58}$$

where the orbital angular momentum is given by

$$\mathbf{L} = \frac{m_e \mathbf{r}\times\mathbf{v}}{\hbar}, \tag{59}$$

and the magnetic moment $\mathbf{m} = (ge\hbar/2m_e)\mathbf{S}$. Furthermore, the factor of $\frac{1}{2}$ has as its origin the relativistic correction due to the 'Thomas precession' which occurs when performing a velocity transformation to an inertial frame of reference. Note that this is necessary since the electron accelerates as it orbits the nucleus. Then, for a *Coulombian* field we have that

$$\frac{1}{r}\frac{\mathrm{d}V(r)}{\mathrm{d}r} = \frac{Ze}{4\pi\epsilon_0 r^3}, \tag{60}$$

and taking into account the result from quantum mechanics for the expected value of $\langle r^{-3}\rangle$

$$\left\langle r^{-3}\right\rangle = \frac{Z^3}{a_0^3 n^3 l\left(l+\frac{1}{2}\right)(l+1)}, \tag{61}$$

it is obtained that, the energy contribution due to spin-orbit coupling is

$$\langle\hat{H}_{so}\rangle = \frac{Z^4 e^2\hbar^2\langle\mathbf{S}\cdot\mathbf{L}\rangle}{4\pi\epsilon_0 a_0^3 n^3 l\left(l+\frac{1}{2}\right)(l+1)}, \tag{62}$$

for which a quartic dependence on the atomic number Z is evident, which indicates that this effect is significant for heavy atoms.

EFFECT ON KOHN-SHAM EQUATIONS

The development presented for the Kohn-Sham equations Eq. 13 is such that the spin has not been considered, which we know does not fully describe the physics of the system. Thus, we must treat the electrons as spinors. For materials that do not contain heavy atoms it is possible to neglect the SOC and make the approximation that the spins can only be oriented along one direction, in which the electronic system is divided into two independent ones: those with spin up and those with spin down. The calculations performed under this approximation are called collinear magnetism, and in this case, the Kohn-Sham equations can be generalized by adding the spin-related indices to the wave functions, potentials and densities, such that one obtains

$$\left(\frac{-\hbar^2\nabla^2}{2m} + V_{\text{ext}} + V_{\text{H}} + V_{\text{XC}\uparrow,\downarrow}\right)|\phi_{i\uparrow}\rangle = E_{i\uparrow,\downarrow}\,|\phi_{i\uparrow,\downarrow}\rangle\,, \tag{63}$$

where the Hartree potential V_H Eq. (52) is unchanged, the total density is, $n(\mathbf{r}) = n_\uparrow(\mathbf{r}) + n_\downarrow(\mathbf{r})$ with

$$n_\uparrow(\mathrm{r}) = \sum_{i\uparrow} |\phi_{i\uparrow}(\mathrm{r})|^2\,, \quad n_\downarrow(\mathrm{r}) = \sum_{i\downarrow} |\phi_{i\downarrow}(\mathrm{r})|^2\,, \tag{64}$$

Moreover, the chosen correlation and exchange term must also be adapted. For non-magnetic systems the spin-up and spin-down systems are identical, so they can be treated as spinless electron systems and this can be considered 'by hand' by introducing a factor of 2 into the equation (55).

On the other hand, when the SOC is considerable, it entangles the electronic states in such a way that the collinear approximation is not possible. As mentioned, this is a relativistic phenomenon, and it occurs as the electrons travel at very high velocities in the central region of the atom[145]. When this is considered, the Kohn-Sham equations take the form

[145] Blundell 2001.

$$\left[\frac{-\hbar^2\nabla^2}{2m} + V_{\text{ext}} + V_{\text{H}} + V_{\text{XC}} + \mathbf{W}_{\text{XC}} \cdot \sigma + h_{\text{SOC}}\right] \begin{pmatrix} \psi_{i\uparrow} \\ \psi_{i\downarrow} \end{pmatrix} = E_i \begin{pmatrix} \psi_{i\uparrow} \\ \psi_{i\downarrow} \end{pmatrix}, \tag{65}$$

Here, the corresponding spinorial treatment is to be performed, V_{cx} and $\mathbf{W_{cx}}$ are the spin-dependent scalar and spin-dependent correlation and exchange potentials, respectively, σ the vector of Pauli matrices

$$\sigma_x = \begin{pmatrix} 0 & 1 \\ 1 & 0 \end{pmatrix}, \quad \sigma_y = \begin{pmatrix} 0 & -i \\ i & 0 \end{pmatrix}, \quad \sigma_z = \begin{pmatrix} 1 & 0 \\ 0 & -1 \end{pmatrix}, \tag{66}$$

finally, the term h_{SOC} is the contribution to the Hamiltonian due to the spin-orbit interaction, which rewriting (58) is given by

$$h_{\text{SOC}} = \frac{\hbar}{4m^2c^2}\sigma \cdot \nabla V(\mathbf{r}) \times \mathbf{p}. \tag{67}$$

8.3. APPENDIX C: CRYSTAL ELECTRONIC WAVE-FUNCTIONS

Crystalline materials are idealized as periodic structures with long-distance ordering. Their atomic arrangement is described by the crystal lattice, which defines the allowed positions for the base elements (atoms or molecules). Therefore, to give a complete description of the crystal it is necessary to specify all the $\mathbf{R}$ vectors connecting equivalent atoms in the crystal and the basic unit containing all the non-equivalent distinct atoms, not linked by a $\mathbf{R}$ vector. The latter is known as the primitive unit cell, which consists of the minimum volume in space that translationally reproduces the crystal. The lattice vectors

$$\mathbf{R} = n_1\mathbf{a}_1 + n_2\mathbf{a}_2 + n_3\mathbf{a}_3, \tag{68}$$

are constructed as linear combinations of the primitive lattice vectors $\mathbf{a}_i$, which are the 3 shortest linearly independent vectors connecting equivalent atoms, so that they form the primitive unit cell. If the condition of translational periodicity is imposed on the lattice, then a Bravais lattice is obtained, a set of equivalent points in space (not only the nodes of the lattice) connected by $\mathbf{R}$ vectors. This definition is convenient because for the study of a material is only necessary to find the $\mathbf{r}$-dependent wavefunctions within the primitive unit cells. Since the equivalent points in space are connected by $\mathbf{R}$, this implies that the potential to which the electrons are subjected has the property

$$\mathcal{V}(\mathbf{r} + \mathbf{R}) = \mathcal{V}(\mathbf{r}). \tag{69}$$

Now, a useful tool to study the properties of periodic functions is the Fourier transform, so from the direct lattice it is possible to construct a lattice of allowed k values, under the condition of translational periodicity; this is defined analogously to the

direct lattice, with the primitive vectors of the reciprocal space

$$\mathbf{b}_1 = \frac{2\pi\,(\mathbf{a}_2 \times \mathbf{a}_3)}{\mathbf{a}_1 \cdot (\mathbf{a}_2 \times \mathbf{a}_3)}, \quad \mathbf{b}_2 = \frac{2\pi\,(\mathbf{a}_3 \times \mathbf{a}_1)}{\mathbf{a}_2 \cdot (\mathbf{a}_3 \times \mathbf{a}_1)}, \quad \mathbf{b}_3 = \frac{2\pi\,(\mathbf{a}_1 \times \mathbf{a}_2)}{\mathbf{a}_3 \cdot (\mathbf{a}_1 \times \mathbf{a}_2)}, \tag{70}$$

which satisfies the relation

$$\mathbf{a}_i \cdot \mathbf{b}_j = 2\pi\delta_{ij} \tag{71}$$

and with these it is possible to define the $\mathbf{G}$ vectors connecting equivalent points in the reciprocal space

$$\mathbf{G} = m_1\mathbf{b}_1 + m_2\mathbf{b}_2 + m_3\mathbf{b}_3, \tag{72}$$

by definition, it follows that

$$\mathbf{R} \cdot \mathbf{G} = 2\pi l, \tag{73}$$

implying that

$$\mathrm{e}^{\mathrm{i}\mathbf{G}\cdot\mathbf{R}} = 1. \tag{74}$$

With this in mind, it is possible to apply the condition of translational periodicity to wave functions, an idea consigned in Bloch's theorems:

Theorem 1: If one considers the Hamiltonian for a particle, of the form

$$\hat{H} = \frac{\hbar^2\nabla^2_{\mathbf{r}}}{2m_e} + \mathcal{V}(\mathbf{r}), \quad with \quad \mathcal{V}(\mathbf{r}+\mathbf{R}) = \mathcal{V}(\mathbf{r}), \tag{75}$$

then, a vector $\mathbf{k} = (k_1, k_2, k_3)$ can be chosen to differentiate the eigenfunctions and the wave functions are of the form:

$$\phi_{\mathbf{k}}(\mathbf{r}+\mathbf{R}) = \mathrm{e}^{i\mathbf{k}\cdot\mathbf{R}}\phi_{\mathbf{k}}(\mathbf{r}), \tag{76}$$

Here, the ϕ_k states are called Bloch states. It can be seen that k_i and $k_i + 2\pi$ corre-

spond to the same eigenvalue [146] e^{-ik_i} of ϕ, so that they refer to the same state. This implies that in 2D the index set (k_1, k_2) has the topology of a toroid and in 3D the set (k_1, k_2, k_3) of a 3-toroid, being closed spaces.

Theorem 2: The eigenfunctions of the Hamiltonian Eq. (75) must have the form

$$\phi_{\mathbf{k}}(\mathbf{r}) = \mathrm{e}^{i\mathbf{k}\cdot\mathbf{r}} u_{\mathbf{k}}(\mathbf{r}) \quad with \quad u_{\mathbf{k}}(\mathbf{r}+\mathbf{R}) = u_{\mathbf{k}}(\mathbf{r}), \tag{77}$$

that is, the wave functions $\phi_{\mathbf{k}}(\mathbf{r})$ can be expressed as the product of a phase factor $\mathrm{e}^{i\mathbf{k}\cdot\mathbf{r}}$ (plane wave) and the functions $u_{\mathbf{k}}(\mathbf{r})$ (modulating function), which incorporate the periodicity of the Bravais lattice.

Then, the time-independent Schrödinger equation for these states is such that

$$\hat{H}\phi_{\mathbf{k}}^{(n)} = E_{n\mathbf{k}}\phi_{\mathbf{k}}^{(n)}, \tag{78}$$

it is necessary to introduce the index n to describe the set of eigenfunctions ϕ_k and eigenvalues E_n; so that the energy values corresponding to the same value of n are continuous functions of $\mathbf{k}$ and are called energy bands.

The functions $\phi_{\mathbf{k}}^{(n)}(\mathbf{r})$ for different values of $\mathbf{k}$ obey different boundary conditions, due to the Eq. (76). For this reason, it is convenient to work with the periodic Bloch functions

$$u_{\mathbf{k}}^{(n)}(\mathbf{r}) = e^{-i\mathbf{k}\cdot\mathbf{r}}\phi_{\mathbf{k}}^{(n)}(\mathbf{r}), \tag{79}$$

which obey the periodic conditions in Eq. (77) and satisfy with

$$u_{\mathbf{k}+\mathbf{G}}^{(n)}(\mathbf{r}) = e^{-i\mathbf{G}\cdot\mathbf{r}} u_{\mathbf{k}}^{(n)}(\mathbf{r}), \tag{80}$$

In this manner, they belong to the same Hilbert space of periodic functions defined on

[146] Of the translation operator $T_{\mathrm{a}_j}|\psi_{n\kappa}\rangle = e^{-i\kappa_j}|\psi_{n\kappa}\rangle$, equivalent to Eq. (76).

the primitive unit cell, which can be taken into account when solving the Kohn-Sham equations. For this we replace the Bloch states Eq. (77) in the Eq. (13), so that

$$-\mathrm{e}^{-i\mathbf{k}\cdot\mathbf{r}}\frac{\hbar^2}{2m}\nabla^2\left[\mathrm{e}^{i\mathbf{k}\cdot\mathbf{r}}u_{\mathbf{k}}^{(n)}(\mathbf{r})\right]+V_{\mathrm{tot}}(\mathbf{r})u_{\mathbf{k}}^{(n)}(\mathbf{r})=E_{\mathbf{k}}^{(n)}u_{\mathbf{k}}^{(n)}(\mathbf{r}), \tag{81}$$

where the potential terms have been grouped into

$$V_{\mathrm{tot}}(\mathbf{r})=V_{\mathrm{n}}(\mathbf{r})+V_{\mathrm{H}}(\mathbf{r})+V_{xc}(\mathbf{r}), \tag{82}$$

so that, it is possible to obtain the Kohn-Sham equations as

$$\left[-\frac{h^2}{2m}(\nabla+i\mathbf{k})^2+V_{\mathrm{tot}}(\mathbf{r})\right]u_{\mathbf{k}}^{(n)}(\mathbf{r})=E_{\mathbf{k}}^{(n)}u_{\mathbf{k}}^{(n)}(\mathbf{r}), \tag{83}$$

in which the exponential factor $e^{-i\mathbf{G}}$ does not appear and the only function to be determined is the periodic function $u_{\mathbf{k}}^{(n)}$, which can be normalized to the unit cell of the crystal

$$\int_{\mathrm{UC}}\left|u_{\mathbf{k}}^{(n)}(\mathbf{r})\right|^2 d\mathbf{r}=1, \tag{84}$$

so that each function can only accommodate one electron per unit cell. This result implies that to study electrons in crystals it is only necessary to solve the Schrödinger equation(Kohn-Sham in DFT) within a unit cell primitive and apply periodic boundary conditions. Once determined $u_{\mathbf{k}}^{(n)}(\mathbf{r})$, by the periodic conditions Eq. (77), the solution in any other cell of the crystal is identically the same. Finally, the electron density can be obtained by integration over the n and k indices,

$$n(\mathbf{r})=\sum_i\int_{\mathrm{BZ}}\frac{d\mathbf{k}}{\Omega_{\mathrm{BZ}}}f_{\mathbf{k}}^{(n)}\left|u_{\mathbf{k}}^{(n)}(\mathbf{r})\right|^2 \tag{85}$$

Here, the integral is taken only for the first Brillouin zone (Wigner-Seitz cell in the reciprocal space) and $f_{\mathbf{k}}^{(n)}$ are the occupancy numbers, whose value is 1 for occupied

states and 0 for others.

8.4. APPENDIX D: QUANTUM ANOMALOUS HALL EFFECT (QAHE)

To understand the quantum anomalous Hall effect[147] a brief review of the family of 'Hall effects' is in order. First, the ordinary Hall effect (OHE) indicates the presence of a potential difference across the direction transverse to the current being transmitted through a conductor in the presence of a perpendicular magnetic field. This arises due to the deflection of electrons by the Lorentz force. In this case, the Hall voltage is proportional to the applied magnetic field and the Hall resistance, defined as the transverse voltage over the current, has a linear dependence.

Secondly, the anomalous Hall effect (AHE) is presented in ferromagnetic materials, in which the dependence of the Hall resistance presents a large slope at low magnetic field values, originated by the magnetization of the material; so that the (AHE) can be measured for a case of zero external magnetic cases.

Thirdly, the quantum Hall effect (QHE) is that presented in a two-dimensional electron gas in which Landau levels arise under the application of a large electromagnetic field. In this case, the dependence of the Hall resistance is linear up to certain points for which they take constant values. In these constant regions, the Hall conductivity takes the value ce^2/h, with c integer or fractional, i.e., it is quantized. Likewise, there is a zero resistance in edge dissipation, which is topological in nature, which will be seen below through the connection between the Hall conductivity and the first Chern number.

Finally, the quantum anomalous Hall effect as its name suggests exhibits the characteristics of the (QHE) with the conditions of the (AHE); that is, a topological phase with conducting edge states without the need for an external magnetic field.

Now, to show the connection between the topological characteristics of the band

[147] Vanderbilt 2018; Bernevig 2013; Zang, Cros, and Hoffmann 2018; K. He, Yayu Wang, and Xue 2013.

structure of a material and the Hall conductivity it is possible to start from the expression for the expected value of the velocity of electrons subjected to an electric field $\mathbf{E}$, in terms of the Bloch states $|u_{\mathbf{k}}^{(n)}$ (see Ref.[148])

$$\left\langle \mathbf{v}_{\mathbf{k}}^{(n)} \right\rangle = \frac{1}{\hbar}\nabla_{\mathbf{k}}\epsilon_{\mathbf{k}}^{(n)} + \frac{e}{\hbar}\mathbf{E} \times \mathbf{\Omega}^{(n)}(\mathbf{k}), \tag{86}$$

where $\mathbf{\Omega}^{(n)}(\mathbf{k})$ is the Berry curvature of the band. The first term in the expression to the right of equality is the group velocity and the second is known as the 'anomalous velocity' and is transverse to the electric field, leading to a Hall current for the case where the Berry curvature is non-zero. Then, if we analyze a 2D system (x,y plane) with a field $\mathbf{E} = E_x\hat{x}$, the electronic wavefunctions have no k_z component, and the expression (86) in this case takes the form

$$\left\langle \mathbf{v}_{\mathbf{k}}^{(n)} \right\rangle = \frac{1}{\hbar}\nabla_{\mathbf{k}}\epsilon_{\mathbf{k}}^{(n)} - \frac{e}{\hbar}E_x\Omega_{xy}^{(n)}(\mathbf{k})\hat{y}, \tag{87}$$

which would be the contribution of the n band in the $\mathbf{k}$ value of the wave vector; so, to find the total current per unit volume it is necessary to multiply by the charge $-e$ and integrate for all values of the wave vector. Therefore, the contribution of the first term is zero due to the symmetry criteria of the electronic bands and the second term results in

$$j_y = \frac{e^2 E_x}{\hbar}\int_{\mathrm{BZ}} \Omega_{xy}^{(n)}(\mathbf{k})\frac{\mathrm{d}k_x\,\mathrm{d}k_y}{(2\pi)^2}, \tag{88}$$

then, if Ohm's law is considered, the conductivity is given by

$$\sigma_{xy} = j_y/E_x = \frac{e^2}{(2\pi)^2\hbar}\int_{\mathrm{BZ}} \Omega_{xy}^{(n)}(\mathbf{k})\mathrm{d}k_x\,\mathrm{d}k_y \tag{89}$$

[148] Kaxiras and Joannopoulos 2019.

and taking into account the definition of the first Chern number Eq. (36), we find that

$$\sigma_{xy} = \frac{e^2}{2\pi\hbar} C_1^{(n)} = \frac{e^2}{h} C_1^{(n)}. \tag{90}$$

Hence, the Hall conductivity is quantized and is characterized by the first Chern number associated with the electronic structure topology.

8.5. APPENDIX E: WANNIER FUNCTIONS

Wannier functions are a complete basis of orthonormal functions for the space of crystalline electronic functions. Unlike Bloch functions which are oscillating and delocalized in direct space, Wannier functions can be adjusted [149] to have a large degree of localization in real space. For this reason, they are a convenient tool both for providing a way to visualize and interpret the physics of systems and for calculating various physical properties.

The Wannier functions are defined as the Fourier transform of the Bloch wavefunctions $\psi_{\mathbf{k}}^{(n)}(\mathbf{r})$, and there is a one-to-one correspondence between these two. [150]. These are defined as

$$\phi_{\mathbf{R}}^{(n)}(\mathbf{r}) = \sum_{\mathbf{k}} \mathrm{e}^{-\mathrm{i}\mathbf{k}\cdot\mathbf{R}} \psi_{\mathbf{k}}^{(n)}(\mathbf{r}), \tag{91}$$

so that $\phi_{\mathbf{R}}^{(n)}(\mathbf{r})$ is the Wannier function located in the unit cell defined by the lattice vector $\mathbf{R}$. Likewise, we have the inverse linear transformation

$$\psi_{\mathbf{k}}^{(n)}(\mathbf{r}) = \sum_{\mathbf{R}'} \mathrm{e}^{\mathrm{i}\mathbf{k}\cdot\mathbf{R}'} \phi_{\mathbf{R}'}^{(n)}(\mathbf{r}) \tag{92}$$

where any of this set of functions can be used to describe the electronic states. Also, as mentioned, the Wannier functions to fulfill the orthonormality condition, which can be verified, starting from the expression

$$\left\langle \phi_{\mathbf{R}'}^{(m)} \mid \phi_{\mathbf{R}}^{(n)} \right\rangle = \sum_{\mathbf{k}\mathbf{k}'} \mathrm{e}^{-\mathrm{i}\mathbf{k}\cdot\mathbf{R}} \mathrm{e}^{-\mathrm{i}\mathbf{k}'\cdot\mathbf{R}'} \left\langle \psi_{\mathbf{k}'}^{(m)} \mid \psi_{\mathbf{k}}^{(n)} \right\rangle \tag{93}$$

---

[149] It is possible to construct the maximally localized Wannier functions, by taking advantage of the *gauge* invariance of Bloch functions (Marzari et al. 2012)

[150] The results and formulation for degenerate states are similar, and can be found in Ref. (Vanderbilt 2018; Marzari et al. 2012)

and taking into account that the Bloch functions are eigenfunctions of the Hermitian operator ($\hat{H}$) and are normalized, then

$$\left\langle \phi_{\mathbf{R}'}^{(m)} \mid \phi_{\mathbf{R}}^{(n)} \right\rangle = \sum_{\mathbf{k}\mathbf{k}'} e^{-\mathrm{i}\mathbf{k}\cdot\mathbf{R}} \mathrm{e}^{\mathbf{i}\mathbf{k}'\cdot\mathbf{R}'} \delta_{\mathbf{k}\mathbf{k}'} \delta_{mn} = \delta\left(\mathbf{R}-\mathbf{R}'\right) \delta_{mn} \tag{94}$$

Now, some of the properties of Wannier functions are as follows:

- They are localized functions in real space, i.e., $\phi_{\mathbf{R}}^{(n)}(\mathbf{r}) \to 0$ when $|\mathbf{r}-\mathbf{R}|$ is large.
- They are translational images of themselves: $\phi_{\mathbf{R}}^{(n)}(\mathbf{r}) = \phi_{\mathbf{R}}^{(n)}(\mathbf{r}-\mathbf{R})$.
- They generate the same subspace of the Hilbert space that the Bloch functions generate, so it is possible to construct a completeness relation and its respective projection operator:$\mathcal{P}_n = \sum_{\mathbf{R}} |\phi_{\mathbf{R}}^{(n)}\rangle\langle\phi_{\mathbf{R}}^{(n)}|$

Additionally, it is possible to calculate the electron density from the Wannier functions as follows.

$$n(\mathbf{r}) = \langle \mathbf{r} \left| \mathcal{P}_n \right| \mathbf{r} \rangle = \frac{V_{\text{cell}}}{(2\pi)^3} \int_{\mathrm{BZ}} \left| \psi_{\mathbf{k}}^{(n)}(\mathbf{r}) \right|^2 d^3k = \sum_{\mathbf{R}} \left| \phi_{\mathbf{R}}^{(n)}(\mathbf{r}) \right|^2. \tag{95}$$

On the other hand, the Wannier functions are connected to the topological properties of the electronic bands through the elements of the position matrix, so these are.

$$\langle \phi_{\mathbf{0}}^{(n)}(\mathbf{r}) | \mathbf{r} | \phi_{\mathbf{R}}^{(n)}(\mathbf{r}) \rangle = \mathbf{A}_{\mathbf{R}}^{(n)}, \tag{96}$$

where $\mathbf{A}_{\mathbf{R}}^{(n)}$ are the Fourier coefficients of the Berry connection transform $\mathbf{A}_{\mathbf{k}}^{(n)}$, i.e. [151]

$$\mathbf{A}^{(n)}(\mathbf{k}) = \sum_{\mathbf{R}} e^{i\mathbf{k}\cdot\mathbf{R}} \mathbf{A}_{\mathbf{R}}^{(n)}. \tag{97}$$

[151] It can also be seen from the Berry connection introduced in Eq. (32), which is the expected value of the position operator in the unit cell, in the momentum representation.

Likewise, an important quantity is the load centre of the Wannier functions

$$\bar{\mathbf{r}}_n = \langle \phi_{\mathbf{0}}^{(n)}(\mathbf{r}) | \mathbf{r} | \phi_{\mathbf{0}}^{(n)}(\mathbf{r}) \rangle \tag{98}$$

which by Eq. (96) is equal to $\mathbf{A}(\mathbf{0})^{(n)}$, such that taking into account Eq. (97) we obtain that it is the average of Berry's connection $\mathbf{A}(\mathbf{k})^{(n)}$.

$$\bar{\mathbf{r}}_n = \frac{V_{\text{cell}}}{(2\pi)^3} \int_{\text{BZ}} \mathbf{A}^{(n)}(\mathbf{k}) d^3k = \frac{V_{\text{cell}}}{(2\pi)^3} \int_{\text{BZ}} \left\langle u_{\mathbf{k}}^{(n)} \mid i\nabla_{\mathbf{k}} u_{\mathbf{k}}^{(n)} \right\rangle d^3k, \tag{99}$$

and therefore the charge center of the Wannier functions is proportional to the Berry phase. Finally, a fundamental property is that the matrix elements of the Hamiltonian between Wannier functions are diagonal, and are the Fourier coefficients for the energy expansion of the band n

$$\langle \phi_{\mathbf{0}}^{(n)}(\mathbf{r}) | \hat{H} | \phi_{\mathbf{R}}^{(n)}(\mathbf{r}) \rangle = E_{n\mathbf{R}}, \tag{100}$$

result implying that the Wannier functions provide an accurate representation of the dispersion $E_{\mathbf{k}}^{(n)}$.

8.6. APPENDIX F: WIEN2k ELECTRONIC BAND STRUCTURES

The electronic band structure graphs calculated employing the WIEN2K DFT package are presented along with the graphs obtained from VASP. The calculations details can be found at Sec. 7. Results with and without SOC are presented, as well as the calculations performed with and without taking into account the Hubbard U correction.

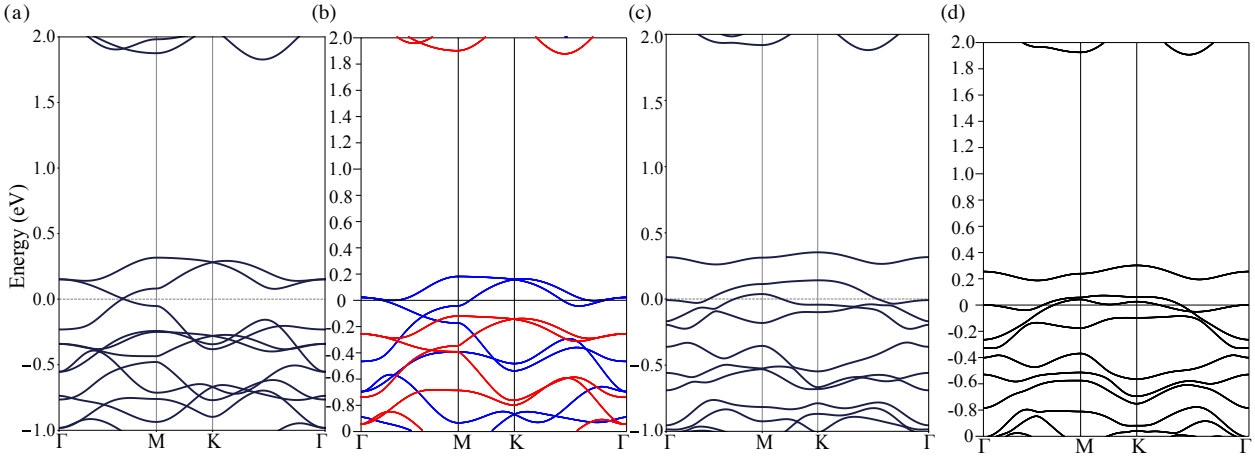

Figure 26. Electronic band structure for $OsCl_3$ with U=0 eV employing the PBEsol exchange and correlation functional, calculated with (a,c) VASP (b,d) WIEN2K, without and with SOC, respectively.

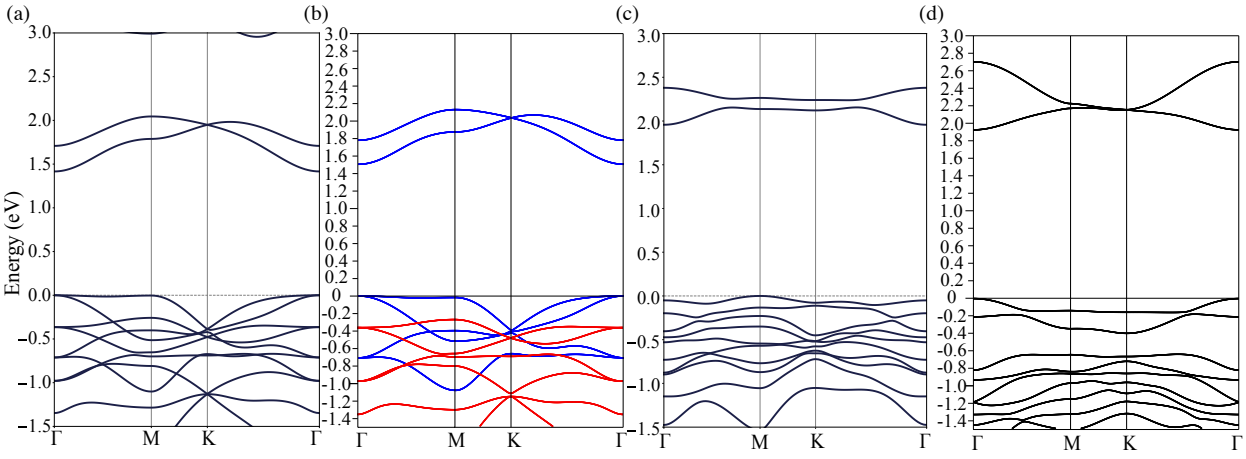

Figure 27. Electronic band structure for $OsCl_3$ with U=4 eV employing the PBEsol exchange and correlation functional, calculated with (a,c) VASP (b,d) WIEN2K, without and with SOC, respectively.

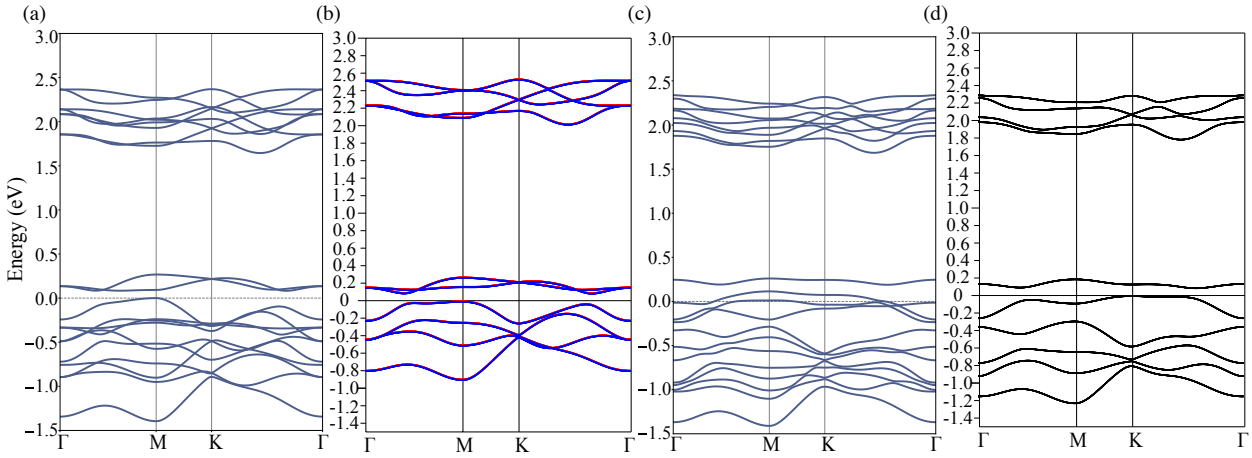

Figure 28. Electronic band structure for $OsBr_3$ with U=0 eV employing the PBEsol exchange and correlation functional, calculated with (a,c) VASP (b,d) WIEN2K, without and with SOC, respectively.

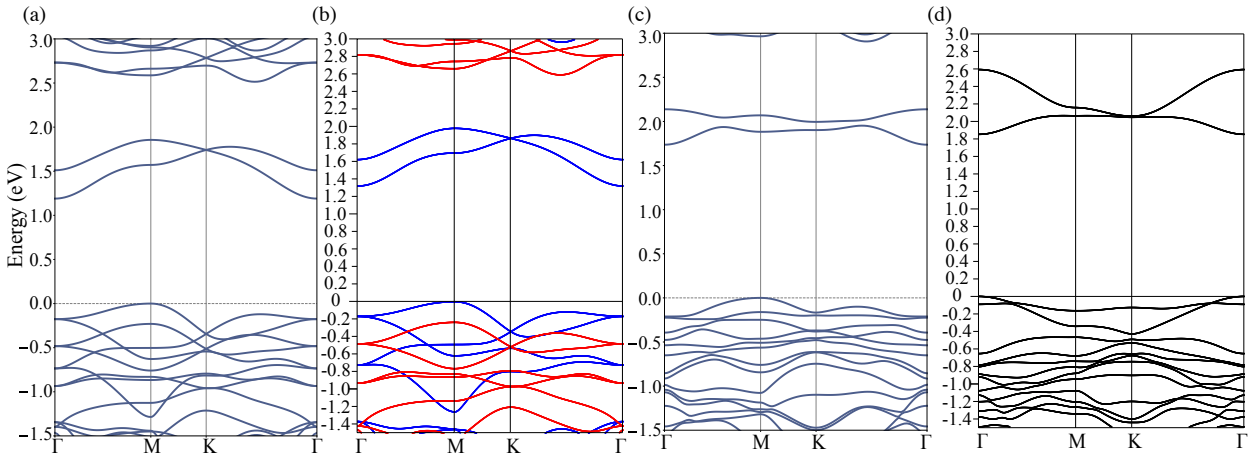

Figure 29. Electronic band structure for $OsBr_3$ with U=4 eV employing the PBEsol exchange and correlation functional, calculated with (a,c) VASP (b,d) WIEN2K, without and with SOC, respectively.

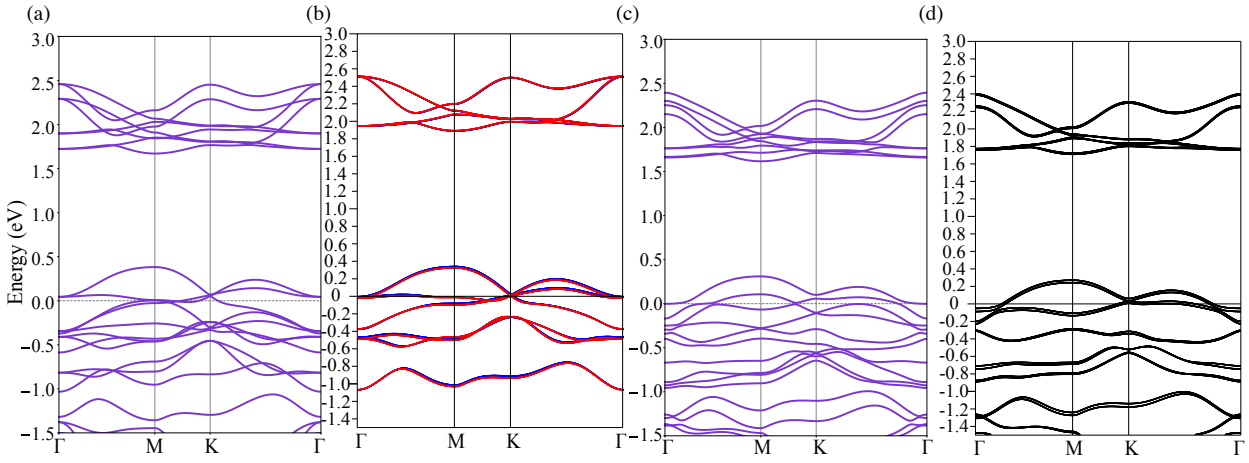

Figure 30. Electronic band structure for OsI_3 with U=0 eV employing the PBEsol exchange and correlation functional, calculated with (a,c) VASP (b,d) WIEN2K, without and with SOC, respectively.

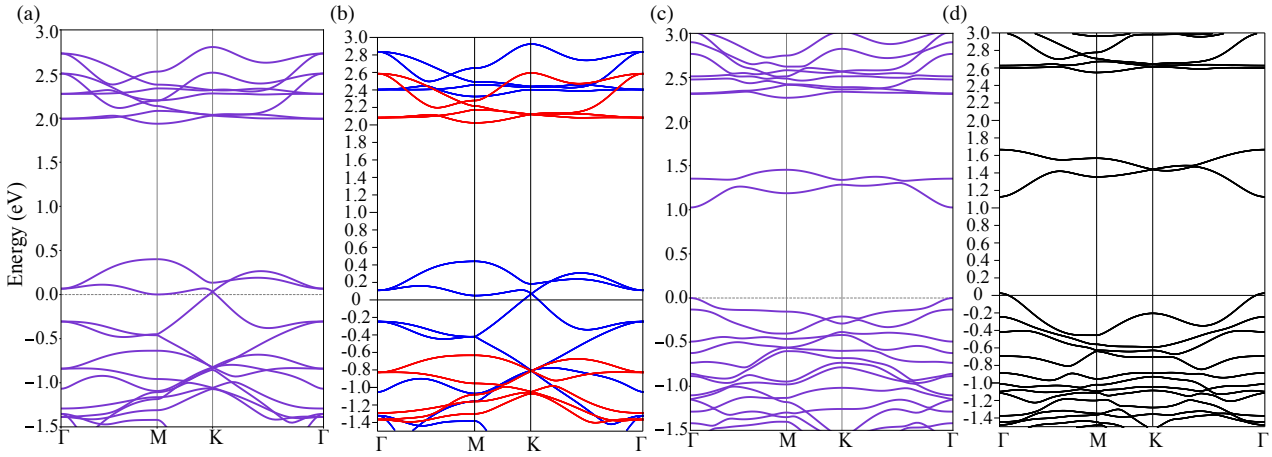

Figure 31. Electronic band structure for OsI_3 with U=4 eV employing the PBEsol exchange and correlation functional, calculated with (a,c) VASP (b,d) WIEN2K, without and with SOC, respectively.

Bibliography

Ahmed, S.J. et al. (2013). “BerryPI: A software for studying polarization of crystalline solids with WIEN2k density functional all-electron package”. In: *Comput. Phys. Commun.* 184.3, pp. 647–651.

al., Giovanni Pizzi et (2020). “Wannier90 as a community code: new features and applications”. In: *J. Phys. : Condens. Matter* 32.16, p. 165902.

Allred, A.L. (1961). “Electronegativity values from thermochemical data”. In: *J. Inorg. Nucl. Chem.* 17.3, pp. 215–221.

Ando, Yoichi (2013). “Topological insulator materials”. In: *J. Phys. Soc. Jpn.* 82.10, pp. 1–32.

Bader, Richard F. W. (1991). “A quantum theory of molecular structure and its applications”. In: *Chem. Rev.* 91.5, pp. 893–928.

Becke, A D (1988). “Density-functional exchange-energy approximation with correct asymptotic behavior”. en. In: *Phys. Rev. A Gen. Phys.* 38.6, pp. 3098–3100.

Becke, Axel D (1993). “Density-functional thermochemistry. III. The role of exact exchange”. In: *J. Chem. Phys.* 98.7, pp. 5648–5652.

Bercioux, Dario et al., eds. (2018). *Topological matter:Lectures from the topological matter school 2017*. en. 1st ed. Basel, Switzerland: Springer International Publishing. Chap. 3.

Bercioux, et al (2018). *Topological matter: Lectures from the topological matter school 2017*. en. 1st ed. Basel, Switzerland: Springer International Publishing.

Bernevig, B Andrei (2013). *Topological insulators and topological superconductors*. en. Princeton, NJ: Princeton University Press.

Bianco, Elisabeth et al. (2013). "Stability and Exfoliation of Germanane: A Germanium Graphane Analogue". In: *ACS Nano* 7.5, pp. 4414–4421.

Blaha, Peter et al. (2020). "WIEN2k: An APW+lo program for calculating the properties of solids". In: *J. Chem. Phys.* 152.7, p. 074101.

Blanco de Paz, María et al. (2020). "Tutorial: Computing Topological Invariants in 2D Photonic Crystals". In: *Adv. Quantum Technol.* 3.2, p. 1900117.

Bloch, P. E. (1994). "Projector augmented-wave method". In: *Phys. Rev. B* 50 (24), pp. 17953–17979.

Blundell, Stephen (2001). *Magnetism in Condensed Matter*. en. London, England: Oxford University Press.

Bonilla, Manuel et al. (2018). "Strong roomerature ferromagnetism in VSe2 monolayers on van der Waals substrates". In: *Nat. Nanotechnol.* 13.4, pp. 289–293.

Burch, Kenneth S., David Mandrus, and Je Geun Park (2018). "Magnetism in two-dimensional van der Waals materials". In: *Nature* 563.7729, pp. 47–52.

Butler, Sheneve Z. et al. (2013). "Progress, challenges, and opportunities in two-dimensional materials beyond graphene". In: *ACS Nano* 7.4, pp. 2898–2926.

Cai, Xinghan et al. (2019). “Atomically Thin CrCl3: An In-Plane Layered Antiferromagnetic Insulator”. In: *Nano Lett.* 19.6, pp. 3993–3998.

Chang, Cui-Zu et al. (2015). “High-precision realization of robust quantum anomalous Hall state in a hard ferromagnetic topological insulator”. In: *Nat. Mater.* 14.5, pp. 473–477.

Choudhuri, Indrani, Preeti Bhauriyal, and Biswarup Pathak (2019). “Recent Advances in Graphene-like 2D Materials for Spintronics Applications”. In: *Chem. Mater.* 31.20, pp. 8260–8285.

Coey, J (2010). *Magnetism and magnetic materials*. en. Cambridge, England: Cambridge University Press.

Cohen-Tannoudji, Claude, Bernard Diu, and Franck Laloe (2020). *Quantum Mechanics, Volume 1: Basic Concepts, Tools, and Applications*. 2nd ed. Weinheim, Germany: Wiley-VCH Verlag.

Cortie, David L. et al. (2020). “Two-Dimensional Magnets: Forgotten History and Recent Progress towards Spintronic Applications”. In: *Adv. Funct. Mater.* 30.18, pp. 1–15.

David, Vanderbilt (2018). “Chapter 5.3.1:Topological Index Set”. In: *Berry phases in electronic structure theory: Electric polarization, orbital magnetization and topological insulators*. Cambridge, England: Cambridge University Press.

Dean, C. R. et al. (2010). “Boron nitride substrates for high-quality graphene electronics”. In: *Nat. Nanotechnol.* 5.10, pp. 722–726.

Deng, Yujun et al. (2020). “Quantum anomalous Hall effect in intrinsic magnetic topological insulator MnBi2Te4”. en. In: *Science* 367.6480, pp. 895–900.

Dominik, Gresch et al. (2017). “Z2Pack: Numerical implementation of hybrid Wannier centers for identifying topological materials”. In: *Phys. Rev. B* 95 (7), p. 075146.

Dudarev, S. L. et al. (1998). “Electron-energy-loss spectra and the structural stability of nickel oxide: An LSDA+U study”. In: *Phys. Rev. B* 57 (3), pp. 1505–1509.

Fang, Xiaotian et al. (2022). “High Curie temperature and large perpendicular magnetic anisotropy in two-dimensional half metallic OsI3 monolayer with quantum anomalous Hall effect”. In: *Mater. Today Phys.* 28, p. 100847.

Fei, Zaiyao et al. (2018). “Two-dimensional itinerant ferromagnetism in atomically thin Fe3GeTe2”. In: *Nat. Mater.* 17.9, pp. 778–782.

Feng, Wanxiang, Jun Wen, et al. (2012). “First-principles calculation of Z2 topological invariants within the FP-LAPW formalism”. In: *Comput. Phys. Commun.* 183.9, pp. 1849–1859.

Feng, Wanxiang, Yugui Yao, et al. (2012). “Intrinsic spin Hall effect in monolayers of group-VI dichalcogenides: A first-principles study”. In: *Phys. Rev. B* 86 (16), p. 165108.

Floris, A. et al. (2020). “Hubbard-corrected density functional perturbation theory with ultrasoft pseudopotentials”. In: *Physical Review B* 101.6, p. 064305.

Fukui, Takahiro, Yasuhiro Hatsugai, and Hiroshi Suzuki (2005). “Chern Numbers in Discretized Brillouin Zone: Efficient Method of Computing (Spin) Hall Conductances”. In: *J. Phys. Soc. Jpn.* 74.6, pp. 1674–1677.

G., Kresse and Joubert D. (1999). “From ultrasoft pseudopotentials to the projector augmented-wave method”. In: *Phys. Rev. B* 59 (3), pp. 1758–1775.

G., Kresse and Hafner J. (1993). “Ab initio molecular dynamics for liquid metals”. In: *Phys. Rev. B* 47 (1), pp. 558–561.

Gibertini, M. et al. (2019). “Magnetic 2D materials and heterostructures”. In: *Nat. Nanotechnol.* 14.5, pp. 408–419.

Giustino, Feliciano (2014). *Materials modelling using density functional theory: Properties and predictions*. London, England: Oxford University Press.

Goedecker, Stefan (2004). “Minima hopping: An efficient search method for the global minimum of the potential energy surface of complex molecular systems”. In: *TheJ. Chem. Phys.* 120.21, pp. 9911–9917.

Gong, Cheng, Lin Li, et al. (2017). “Discovery of intrinsic ferromagnetism in two-dimensional van der Waals crystals”. In: *Nature* 546.7657, pp. 265–269.

Gong, Cheng and Xiang Zhang (2019). “Two-dimensional magnetic crystals and emergent heterostructure devices”. In: *Science* 363.6428.

Gresch, Dominik et al. (2017). “Z2Pack: Numerical implementation of hybrid Wannier centers for identifying topological materials”. In: *Phys. Rev. B* 95 (7), p. 075146.

Griffiths, David J (2013). *Introduction to electrodynamics: International edition*. en. 4th ed. Upper Saddle River, NJ: Pearson.

Gupta, Ankur, Tamilselvan Sakthivel, and Sudipta Seal (2015). “Recent development in 2D materials beyond graphene”. In: *Progress in Materials Science* 73, pp. 44–126.

Haldane, F. D. M. (1988). “Model for a Quantum Hall Effect without Landau Levels: Condensed-Matter Realization of the "Parity Anomaly"”. In: *Physical Review Letters* 61.18, pp. 2015–2018.

Hasan, M. Z. and C. L. Kane (2010). “Colloquium: Topological insulators”. In: *Rev. Mod. Phys.* 82.4, pp. 3045–3067.

He, Junjie et al. (2017). “Near-room-temperature Chern insulator and Dirac spin-gapless semiconductor: nickel chloride monolayer”. In: *Nanoscale* 9.6, pp. 2246–2252.

He, Ke, Yayu Wang, and Qi-Kun Xue (2013). “Quantum anomalous Hall effect”. In: *National Science Review* 1.1, pp. 38–48.

He, Xu et al. (2021). “TB2J: A python package for computing magnetic interaction parameters”. In: *Comput. Phys. Commun.* 264, p. 107938.

Henkelman, Graeme A, Andri Arnaldsson, and Hannes Jónsson (2006). “A fast and robust algorithm for Bader decomposition of charge density”. In: *Comput. Mater. Sci.* 36, pp. 354–360.

Heyd, Jochen, Gustavo Scuseria, and Matthias Ernzerhof (2003). “Hybrid functionals based on a screened Coulomb potential”. In: *Journal of Chemical Physics* 118, pp. 8207–8215.

Heyd, Jochen and Gustavo E Scuseria (2004). “Efficient hybrid density functional calculations in solids: assessment of the Heyd-Scuseria-Ernzerhof screened Coulomb hybrid functional”. en. In: *J. Chem. Phys.* 121.3, pp. 1187–1192.

Heyd, Jochen, Gustavo E Scuseria, and Matthias Ernzerhof (2003). “Hybrid functionals based on a screened Coulomb potential”. In: *J. Chem. Phys.* 118.18, pp. 8207–8215.

“High throughput computational screening for 2D ferromagnetic materials: The critical role of anisotropy and local correlations (2D Materials 6 (045018)” (2020). In: *2D Materials* 7.4.

Himmetoglu, Burak et al. (2013). “Hubbard-corrected DFT energy functionals: The LDAU description of correlated systems”. In: *International Journal of Quantum Chemistry* 114.1, pp. 14–49.

Hohenberg, P. and W. Kohn (1964). “Inhomogeneous Electron Gas”. In: *Phys. Rev.* 136 (3B), B864–B871.

Hu, Jun et al. (2018). “Engineering magnetic anisotropy in two-dimensional magnetic materials”. In: *Advances in Physics: X* 3.1, pp. 443–477.

Huang, Bevin, Genevieve Clark, Dahlia R. Klein, et al. (2018). “Electrical control of 2D magnetism in bilayer CrI3”. In: *Nat. Nanotechnol.* 13.7, pp. 544–548.

Huang, Bevin, Genevieve Clark, Efrén Navarro-Moratalla, et al. (2017). “Layer-dependent ferromagnetism in a van der Waals crystal down to the monolayer limit”. In: *Nature* 546.7657, pp. 270–273.

Huang, Pu et al. (2020). “Recent advances in two-dimensional ferromagnetism: Materials synthesis, physical properties and device applications”. In: *Nanoscale* 12.4, pp. 2309–2327.

Iyikanat, F. et al. (2018). “Tuning electronic and magnetic properties of monolayer α-RuCl3 by in-plane strain”. In: *Journal of Materials Chemistry C* 6.8, pp. 2019–2025.

Jiang, Shengwei, Lizhong Li, et al. (2018). “Controlling magnetism in 2D CrI3 by electrostatic doping”. In: *Nat. Nanotechnol.* 13.7, pp. 549–553.

Jiang, Shengwei, Jie Shan, and Kin Fai Mak (2018). “Electric-field switching of two-dimensional van der Waals magnets”. In: *Nat. Mater.* 17.5, pp. 406–410.

Jiang, Shengwei, Hongchao Xie, et al. (2020). “Exchange magnetostriction in two-dimensional antiferromagnets”. In: *Nat. Mater.* 19.12, pp. 1295–1299.

Jiang, Xue et al. (2021). “Recent progress on 2D magnets: Fundamental mechanism, structural design and modification”. In: *Applied Physics Reviews* 8.3, p. 031305.

Jiang, Zhou et al. (2018). “Screening and Design of Novel 2D Ferromagnetic Materials with High Curie Temperature above Room Temperature”. In: *ACS Applied Materials and Interfaces* 10.45, pp. 39032–39039.

Kaxiras, Efthimios and John D Joannopoulos (2019). *Quantum Theory of Materials*. Cambridge, England: Cambridge University Press.

Khomskii, Daniel I (2014). *Transition Metal Compounds*. Cambridge, England: Cambridge University Press.

Klitzing, K. v., G. Dorda, and M. Pepper (1980). “New Method for High-Accuracy Determination of the Fine-Structure Constant Based on Quantized Hall Resistance”. In: *Physical Review Letters* 45.6, pp. 494–497.

Kohn, W. and L. J. Sham (1965). “Self-Consistent Equations Including Exchange and Correlation Effects”. In: *Phys. Rev.* 140 (4A), A1133–A1138.

Kong, Xiangru et al. (2018). “Quantum anomalous Hall effect in a stable 1T-YN2 monolayer with a large nontrivial bandgap and a high Chern number”. In: *Nanoscale* 10 (17), pp. 8153–8161.

Kresse, G and J Furthmüller (1996). “Efficiency of ab-initio total energy calculations for metals and semiconductors using a plane-wave basis set”. In: *Comput. Mater. Sci.* 6.1.

Kresse, G and J Hafner (1994). “Norm-conserving and ultrasoft pseudopotentials for first-row and transition elements”. In: 6.40, pp. 8245–8257.

Kresse, G. and J. Furthmuller (1996). “Efficient iterative schemes for ab initio total-energy calculations using a plane-wave basis set”. In: *Phys. Rev. B* 54 (16), pp. 11169–11186.

Kresse, G. and J. Furthmüller (1996). “Efficiency of ab-initio total energy calculations for metals and semiconductors using a plane-wave basis set”. In: *Comput. Mater. Sci.* 6.1, pp. 15–50.

Kresse, G. and J. Hafner (1993). “Ab initio molecular dynamics for liquid metals”. In: *Phys. Rev. B* 47 (1), pp. 558–561.

Kresse, G. and D. Joubert (1999). “From ultrasoft pseudopotentials to the projector augmented-wave method”. In: *Phys. Rev. B* 59 (3), pp. 1758–1775.

Krukau, Aliaksandr V et al. (2006). “Influence of the exchange screening parameter on the performance of screened hybrid functionals”. en. In: *J. Chem. Phys.* 125.22, p. 224106.

Kuneš, Jan et al. (2010). “Wien2wannier: From linearized augmented plane waves to maximally localized Wannier functions”. In: *Comput. Phys. Commun.* 181.11, pp. 1888–1895.

Lado, J L and J Fernández-Rossier (2017). “On the origin of magnetic anisotropy in two dimensional CrI3”. In: *2D Materials* 4.035002, p. 3.

Lee, Jae Ung (2016). “Ising-Type Magnetic Ordering in Atomically Thin FePS3”. In: *Nano Lett.* 16.12, pp. 7433–7438.

Lee, Jae Ung et al. (2016). “Ising-Type Magnetic Ordering in Atomically Thin FePS3”. In: *Nano Lett.* 16.12, pp. 7433–7438. arXiv: 1608.04169.

Lembke, Dominik, Simone Bertolazzi, and Andras Kis (2015). “Single-Layer MoS2 Electronics”. In: *Accounts of Chemical Research* 48.1, pp. 100–110.

Li, B. G. et al. (2020). “First-principles investigation of a new 2D magnetic crystal: Ferromagnetic ordering and intrinsic half-metallicity”. In: *Journal of Chemical Physics* 152.24.

Li, Hai et al. (2014). “Preparation and Applications of Mechanically Exfoliated Single-Layer and Multilayer MoS2 and WSe2 Nanosheets”. In: *Accounts of Chemical Research* 47.4, pp. 1067–1075.

Li, Ping (2019). “Prediction of intrinsic two dimensional ferromagnetism realized quantum anomalous Hall effect”. In: *Phys. Chem. Chem. Phys.* 21 (12), pp. 6712–6717.

Linus, Pauling (1932). “THE NATURE OF THE CHEMICAL BOND. IV. THE ENERGY OF SINGLE BONDS AND THE RELATIVE ELECTRONEGATIVITY OF ATOMS”. In: *JACS* 54.9, pp. 3570–3582.

Liu, Hang et al. (2018). “Screening magnetic two-dimensional atomic crystals with nontrivial electronic topology”. In: *J. Phys. Chem. Lett.* 9.23, pp. 6709–6715.

Liu, Hanzhe et al. (2017). “High-harmonic generation from an atomically thin semiconductor”. In: *Nat. Phys.* 13.3, pp. 262–265.

Liu, Jie et al. (2018). “Analysis of electrical-field-dependent Dzyaloshinskii-Moriya interaction and magnetocrystalline anisotropy in a two-dimensional ferromagnetic monolayer”. In: *Physical Review B* 97.5, pp. 8–10.

Liu, Pan et al. (2017). “Electronic structures and band alignments of monolayer metal trihalide semiconductors MX3”. In: *Journal of Materials Chemistry C* 5.35, pp. 9066–9071.

Liu, Tian et al. (2019). “Prediction of colossal magnetocrystalline anisotropy for transition metal triiodides”. In: *J. Phys.: Condens. Matter* 31.29.

Liu, Y. et al. (2011). “Visualizing Electronic Chirality and Berry Phases in Graphene Systems Using Photoemission with Circularly Polarized Light”. In: *Phys. Rev. Lett.* 107 (16), p. 166803.

Liu, Yuan et al. (2016). “Van der Waals heterostructures and devices”. In: *Nature Reviews Materials* 1.9.

Lu, Yan et al. (2020). “Artificial Multiferroics and Enhanced Magnetoelectric Effect in van der Waals Heterostructures”. In: *ACS Applied Materials and Interfaces* 12.5, pp. 6243–6249.

M, Martin Richard (2020). *Electronic structure: Basic theory and practical methods*. 2nd ed. Cambridge, England: Cambridge University Press.

Mak, K. F. et al. (2014). “The valley Hall effect in MoS₂ transistors”. In: *Science* 344.6191, pp. 1489–1492.

Mak, Kin Fai, Jie Shan, and Daniel C. Ralph (2019). “Probing and controlling magnetic states in 2D layered magnetic materials”. In: *Nature Reviews Physics* 1.11, pp. 646–661.

Martin, Richard M (2020). *Electronic structure: Basic theory and practical methods*. 2nd ed. Cambridge, England: Cambridge University Press.

Marzari, Nicola et al. (2012). “Maximally localized Wannier functions: Theory and applications”. In: *Reviews of Modern Physics* 84.4, pp. 1419–1475. arXiv: 1112.5411.

Mas-Ballesté, Rubén et al. (2011). “2D materials: To graphene and beyond”. In: *Nanoscale* 3.1, pp. 20–30.

McGuire, Michael A. (2017). “Crystal and magnetic structures in layered, transition metal dihalides and trihalides”. In: *Crystals* 7.5.

Mermin, N. D. and H. Wagner (1966). “Absence of ferromagnetism or antiferromagnetism in one- or two-dimensional isotropic Heisenberg models”. In: *Physical Review Letters* 17.22, pp. 1133–1136.

Miao, Naihua and Zhimei Sun (2021). “Computational design of two-dimensional magnetic materials”. In: *Wiley Interdisciplinary Reviews: Computational Molecular Science* January.

Mikitik, G. P. and Yu. V. Sharlai (1999). “Manifestation of Berry’s Phase in Metal Physics”. In: *Phys. Rev. Lett.* 82 (10), pp. 2147–2150.

Monkhorst, Hendrik J. and James D. Pack (1976). “Special points for Brillouin-zone integrations”. In: *Phys. Rev. B* 13 (12), pp. 5188–5192.

Moore, Joel E. (2010). “The birth of topological insulators”. In: *Nature* 464.7286, pp. 194–198.

Mounet, Nicolas et al. (2018). “Two-dimensional materials from high-throughput computational exfoliation of experimentally known compounds”. In: *Nat. Nanotechnol.* 13.3, pp. 246–252.

Nguyen, Thi Phuong Thao et al. (2021). “Electric-field tuning of the magnetic properties of bilayer VI3: A first-principles study”. In: *Physical Review B* 104.1.

Novoselov, K S et al. (2004). “Electric field effect in atomically thin carbon films”. en. In: *Science* 306.5696, pp. 666–669.

Novoselov, K. S. et al. (2016). “2D materials and van der Waals heterostructures”. In: *Science* 353.6298.

O'Hara, Dante J. et al. (2018). "Room Temperature Intrinsic Ferromagnetism in Epitaxial Manganese Selenide Films in the Monolayer Limit". In: *Nano Lett.* 18.5, pp. 3125–3131.

Oleg, Rubel (2022). *BerryPI: Software to study polarization and topological properties of crystalline solids*. en.

Olsen, Thomas et al. (2019). "Discovering two-dimensional topological insulators from high-throughput computations". In: *Phys. Rev. Materials* 3 (2), p. 024005.

Onsager, Lars (1944). "Crystal Statistics. I. A Two-Dimensional Model with an Order-Disorder Transition". In: *Physical Review* 65.3-4, pp. 117–149.

P., Blaha et al. (2018). "WIEN2k: An Augmented Plane Wave Plus Local Orbitals Program for Calculating Crystal Properties". In.

P., Hohenberg and Kohn W. (1964). "Inhomogeneous Electron Gas". In: *Phys. Rev.* 136 (3B), B864–B871.

P., Mikitik G. and Sharlai Yu. V. (2004). "Berry Phase and de Haas–van Alphen Effect in $\mathrm{LaRhIn_5}$". In: *Phys. Rev. Lett.* 93 (10), p. 106403.

Palyi, Andras, Janos K Asboth, and Laszlo Oroszlany (2016). *A short course on topological insulators: Band structure and edge states in one and two dimensions*. en. 1st ed. Cham, Switzerland: Springer International Publishing.

Park, Je Geun (2016). "Opportunities and challenges of 2D magnetic van der Waals materials: Magnetic graphene?" In: *J. Phys.: Condens. Matter* 28.30, p. 301001.

Pauling, Linus (1929). “The principles determining the structure of complex ionic crystals”. en. In: *J. Am. Chem. Soc.* 51.4, pp. 1010–1026.

Perdew, John P, Matthias Ernzerhof, and Kieron Burke (1996). “Rationale for mixing exact exchange with density functional approximations”. In: *J. Chem. Phys.* 105.22, pp. 9982–9985.

Perdew, John P. (2001). “Jacob’s ladder of density functional approximations for the exchange-correlation energy”. In: *AIP Conference Proceedings*. AIP.

Perdew, John P., Kieron Burke, and Matthias Ernzerhof (1996). “Generalized Gradient Approximation Made Simple”. In: *Phys. Rev. Lett.* 77 (18), pp. 3865–3868.

Peter, Blaha et al. (2020). “WIEN2k: An APW+lo program for calculating the properties of solids”. In: *TheJ. Chem. Phys.* 152.7, p. 074101.

Pizzi, Giovanni et al. (2020). “Wannier90 as a community code: new features and applications”. In: *J. Phys.: Condens. Matter* 32.16, p. 165902.

Qi, Xiao Liang and Shou Cheng Zhang (2011). “Topological insulators and superconductors”. In: *Reviews of Modern Physics* 83.4.

Ren, Yafei, Zhenhua Qiao, and Qian Niu (2016). “Topological phases in two-dimensional materials: A review”. In: *Reports on Progress in Physics* 79.6, p. 66501.

Rubel, Oleg (2022). *BerryPI*.

Samarth, Nitin (2017). “Magnetism in flatland”. In: *Nature* 546.7657, pp. 216–217.

Sanville, Edward et al. (2007). “Improved grid-based algorithm for Bader charge allocation”. In: *J. Comput. Chem.* 28.5, pp. 899–908.

Sethulakshmi, N. et al. (2019). “Magnetism in two-dimensional materials beyond graphene”. In: *Materials Today* 27.August, pp. 107–122.

Shabbir, Babar et al. (2018). “Long range intrinsic ferromagnetism in two dimensional materials and dissipationless future technologies”. In: *App. Phys. Rev.* 5.4.

Shannon, R. D. (1976). “Revised effective ionic radii and systematic studies of interatomic distances in halides and chalcogenides”. In: *Acta Crystallographica Section A* 32.5, pp. 751–767.

Sheng, Xian Lei and Branislav K. Nikolić (2017). “Monolayer of the 5d transition metal trichloride OsCl3: A playground for two-dimensional magnetism, room-temperature quantum anomalous Hall effect, and topological phase transitions”. In: *Physical Review B* 95.20, pp. 3–7.

Soluyanov, Alexey A. and David Vanderbilt (2011). “Computing topological invariants without inversion symmetry”. In: *Phys. Rev. B* 83 (23), p. 235401.

Sun Qilong, et al (2019). “Intrinsic ferromagnetism and topological properties in two-dimensional rhenium halides”. In: *Nanoscale* 11.13, pp. 6101–6107.

Sun, Jianwei, Adrienn Ruzsinszky, and John P. Perdew (2015). “Strongly Constrained and Appropriately Normed Semilocal Density Functional”. In: *Physical Review Letters* 115.3, p. 036402.

Sun, Jiaxiang et al. (2020). “The intrinsic magnetism, quantum anomalous Hall effect and Curie temperature in 2D transition metal trihalides”. In: *Phys. Chem. Chem. Phys.* 22.4, pp. 2429–2436.

Sun, Qilong and Nicholas Kioussis (2018). “Prediction of manganese trihalides as two-dimensional Dirac half-metals”. In: *Physical Review B* 97.9, pp. 1–5.

Tang, W, E Sanville, and G Henkelman (2009). “A grid-based Bader analysis algorithm without lattice bias”. In: *J. Phys.: Condens. Matter* 21.8, p. 084204.

Thouless, D. J. (1983). “Quantization of particle transport”. In: *Phys. Rev. B* 27 (10), pp. 6083–6087.

Tian, Liu et al. (2019). “Prediction of colossal magnetocrystalline anisotropy for transition metal triiodides”. In: *J. Phys.: Condens. Matter* 31.29.

Tian, Yingzhen et al. (2019). “Optically Driven Magnetic Phase Transition of Monolayer RuCl3”. In: *Nano Lett.* 19.11, pp. 7673–7680.

Tsuchida, Ryutaro (1938). “Absorption spectra of co-ordination compounds. I”. en. In: *Bull. Chem. Soc. Jpn.* 13.5, pp. 388–400.

Vanderbilt, David (2018). *Berry phases in electronic structure theory: Electric polarization, orbital magnetization and topological insulators*. Cambridge, England: Cambridge University Press.

Villars, Pierre and Karin Cenzual, eds. (n.d.). *MoS2 Crystal Structure: Datasheet from “PAULING FILE Multinaries Edition – 2012” in SpringerMaterials*. Part of SpringerMaterials.

W., Kohn and Sham L. J. (1965). “Self-Consistent Equations Including Exchange and Correlation Effects”. In: *Phys. Rev.* 140 (4A).

Wang, Hongbo et al. (2016). “Doping enhanced ferromagnetism and induced half-metallicity in CrI3 monolayer”. In: *Epl* 114.4.

Wang, Xingzhi et al. (2016). “Raman spectroscopy of atomically thin two-dimensional magnetic iron phosphorus trisulfide (FePS3) crystals”. In: *2D Materials* 3.3, pp. 1–9.

Wang, Ya ping et al. (2018). “High-temperature Dirac half-metal PdCl3: a promising candidate for realizing quantum anomalous Hall effect”. In: *Journal of Materials Chemistry C* 6.38, pp. 10284–10291.

Wang, Zhiyong et al. (2015). “Proximity-Induced Ferromagnetism in Graphene Revealed by the Anomalous Hall Effect”. In: *Phys. Rev. Lett.* 114 (1), p. 016603.

Wang, Zhongying and Baoxia Mi (2017). “Environmental Applications of 2D Molybdenum Disulfide (MoS2) Nanosheets”. In: *Environmental Science and Technology* 51.15, pp. 8229–8244.

Webster, Lucas and Jia An Yan (2018). “Strain-tunable magnetic anisotropy in monolayer CrCl3, CrBr3, and CrI3”. In: *Physical Review B* 98.14, p. 144411.

Wu, QuanSheng et al. (2018). “WannierTools : An open-source software package for novel topological materials”. In: *Comput. Phys. Commun.* 224, pp. 405–416.

Wu, Shu-Chun, Guangcun Shan, and Binghai Yan (2014). “Prediction of Near-Room-Temperature Quantum Anomalous Hall Effect on Honeycomb Materials”. In: *Phys. Rev. Lett.* 113 (25), p. 256401.

Xiao, Di et al. (2012). “Coupled Spin and Valley Physics in Monolayers of MoS_2 and Other Group-VI Dichalcogenides”. In: *Phys. Rev. Lett.* 108 (19), p. 196802.

Xu, Mingsheng et al. (2013). “Graphene-Like Two-Dimensional Materials”. In: *Chem. Rev.* 113.5, pp. 3766–3798.

Yan, J. et al. (2019). “Anisotropic magnetic entropy change in the hard ferromagnetic semiconductor v I3”. In: *Physical Review B* 100.9, pp. 1–8.

You, Jing Yang et al. (2019). “Two-dimensional room-temperature ferromagnetic semiconductors with quantum anomalous hall effect”. In: *Physical Review Applied* 12.2, pp. 1–7.

Yu, Min and Dallas R Trinkle (2011). “Accurate and efficient algorithm for Bader charge integration”. en. In: *J. Chem. Phys.* 134.6, p. 064111.

Zang, Jiadong, Vincent Cros, and Axel Hoffmann, eds. (2018). *Topology in magnetism*. en. 1st ed. Basel, Switzerland: Springer International Publishing.

Zhang, Fang, Wenbo Mi, and Xiaocha Wang (2020). “Spin-Dependent Electronic Structure and Magnetic Anisotropy of 2D Ferromagnetic Janus Cr2I3X3 (X = Br, Cl) Monolayers”. In: *Advanced Electronic Materials* 6.1, p. 1900778.

Zhang, Hu et al. (2018). “Ionicity of bonding in elemental solids”. In: *Journal of Physics Communications* 2.11, p. 115009.

Zhang, Shi-Hao and Bang-Gui Liu (2017). *Intrinsic 2D ferromagnetism, quantum anomalous Hall conductivity, and fully-spin-polarized edge states of FeBr3 monolayer*.

Zhang, Wei Bing et al. (2015). “Robust intrinsic ferromagnetism and half semiconductivity in stable two-dimensional single-layer chromium trihalides”. In: *Journal of Materials Chemistry C* 3.48, pp. 12457–12468.

Zhang, Wei Xi et al. (2019). “Two-dimensional transition-metal halide CoBr3 with spin-polarized Dirac cone”. In: *Phys. Chem. Chem. Phys.* 21.32, pp. 17740–17745.

Zhang, Wen et al. (2019). “Van der Waals magnets: Wonder building blocks for two-dimensional spintronics?” In: *InfoMat* 1.4, pp. 479–495.

Zhang, Xiao-Long, Lan-Feng Liu, and Wu-Ming Liu (2013). “Quantum anomalous Hall effect and tunable topological states in 3d transition metals doped silicene”. en. In: *Sci. Rep.* 3.1, p. 2908.

Zhao, Jijun et al. (2016). “Rise of silicene: A competitive 2D material”. In: *Progress in Materials Science* 83, pp. 24–151.

Zheng, Fawei et al. (2018). “Tunable spin states in the two-dimensional magnet CrI3”. In: *Nanoscale* 10.29, pp. 14298–14303.

Zhong, Ding, Kyle L. Seyler, Xiayu Linpeng, Ran Cheng, et al. (2017). “Van der Waals engineering of ferromagnetic semiconductor heterostructures for spin and valleytronics”. In: *Science Advances* 3.5, pp. 1–7.

Zhong, Ding, Kyle L. Seyler, Xiayu Linpeng, Nathan P. Wilson, et al. (2020). “Layer-resolved magnetic proximity effect in van der Waals heterostructures”. In: *Nat. Nanotechnol.* 15.3, pp. 187–191.

Zhu, Yu et al. (2018). “Systematic search for two-dimensional ferromagnetic materials”. In: *Physical Review Materials* 2.8, pp. 1–5.